IOS

DEACON LABORATORY

COMPRESSIONAL-WAVE VELOCITIES IN OCEAN SEDIMENTS EASTSOUTHEAST OF MADEIRA, ATLANTIC OCEAN

BY

R.B. WHITMARSH, P.R. MILES, R.E. KIRK

& M.R. SAUNDERS

REPORT NO. 257

1988

Natural Environment Research Council

INSTITUTE OF OCEANOGRAPHIC SCIENCES DEACON LABORATORY

INSTITUTE OF OCEANOGRAPHIC SCIENCES

DEACON LABORATORY

Wormley, Godalming,
Surrey, GU8 5UB, U.K.

Telephone: 0428 79 4141
Telex: 858833 OCEANS G
Telefax: 0428 79 3066

Natural Environment Research Council

INSTITUTE OF OCEANOGRAPHIC SCIENCES

DEACON LABORATORY

REPORT No. 257

Compressional-wave velocities in ocean sediments eastsoutheast of Madeira, Atlantic Ocean

R.B. Whitmarsh, P.R. Miles, R.E. Kirk

& M.R. Saunders

1988

Report commissioned by the Admiralty Research Establishment, Portland

DOCUMENT DATA SHEET

AUTHOR	WHITMARSH, R.B., MILES, P.R., KIRK, R.E. & SAUNDERS, M.R.	*PUBLICATION DATE* 1988
TITLE	Compressional-wave velocities in ocean sediments eastsoutheast of Madeira, Atlantic Ocean.	
REFERENCE	Institute of Oceanographic Sciences Deacon Laboratory, Report, No. 257, 82pp.	

ABSTRACT

This report contains the results of a series of seismic experiments conducted in September, 1986 to determine the seismic structure of oceanic sediments in an area about 200 km ESE of Madeira. The work was carried out over six days during RRS Discovery Cruise 161 (WHITMARSH 1986). The work area was chosen by the Admiralty Research Establishment (ARE), Portland so that we would obtain data to assist their interpretation of a series of acoustic propagation experiment conducted along a NE-SW profile between Madeira and the continental margin off Morocco. Pairs of digital ocean-bottom seismographs (DOBS) were deployed at a depth of about 4400 m at three colinear points along a NE-SW profile eastsoutheast of Madeira. The DOBS recorded shots from airgun sources to ranges in excess of 25 km. In addition three disposable sonobuoy profiles were also obtained. Preliminary simple velocity models were obtained from the travel-times of near-vertical-incidence reflections. More sophisticated synthetic seismogram modelling was applied to three wide-angle seismic refraction profiles. This modelling identified an important and unsuspected mid-sediment reflector which had caused multiple reflection of energy refracted within the lower sediments. The upper sediment had velocities of 1.6 to 2.0 km s and the lower sediment velocities lay between 2.14 and 2.51 km s . The mid-sediment reflector appears to be associated with a small or negligible P-wave velocity contrast and a more substantial S-wave velocity difference. For this reason it is not clearly seen on seismic reflection profiles in the area. The seismic structure of the upper sediments could not be constrained by synthetic seismogram modelling because no arrivals from the upper sediments could be distinguished on the record-sections. This is essentially a geometrical problem only soluble in oceanic depths by using bottom sources. The calculated velocity/depth models were transformed to velocity/vertical travel-time and compared with a seismic reflection profile. The mid-sediment reflector was associated with a laterally extensive change in character in the upper part of the profile and the near-constant velocity layer with the transparent, probably pelagic, sediments draped over the volcanic basement. These correlations finally enabled an estimated depth section to be made from the whole reflection profile.

ISSUING ORGANISATION	Institute of Oceanographic Sciences Deacon Laboratory Wormley, Godalming Surrey GU8 5UB. UK.	*TELEPHONE* 0428 79 4141 *TELEX* 858833 OCEANS G *TELEFAX* 0428 79 3066

KEYWORDS *OCEAN BOTTOM SEISMOGRAPHS (DOBS) SEDIMENT PROPERTIES SEISMIC STRUCTURE SEISMIC VELOCITIES SONOBUOYS NORTHEAST ATLANTIC NORTHWEST AFRICA WATERS DISCOVERY/RRS - CRUISE(1986)(161)*	*CONTRACT* *PROJECT* *PRICE* £22.00

CONTENTS

	Page
INTRODUCTION	7
VERTICAL-INCIDENCE SEISMIC REFLECTION PROFILES	10
Echo-sounder profiles (10 kHz)	10
3.5 kHz profiles	11
Airgun reflection profiles (about 60 Hz)	11
THE WIDE-ANGLE SEISMIC REFLECTION/SEISMIC REFRACTION TECHNIQUE	16
Observational techniques	18
Data presentation	18
ANALYSIS OF THE RECORD-SECTIONS	19
Modelling travel-time	20
Modelling amplitudes	20
Modelling procedure	20
RESULTS FROM AROUND POINT L	24
Seismic refraction profiles	24
Ranges	24
Observations	24
Lateral structural homogeneity	27
Modelling	31
RESULTS FROM AROUND POINT MM	37
Seismic refraction profiles	37
Observations	37
Lateral structural homogeneity	43
Modelling	43
RESULTS FROM AROUND POINT NN	49
Seismic refraction profiles	54
Observations	54
Lateral structural homogeneity	57
Modelling	57
SONOBUOY PROFILES	61

DISCUSSION 63
Velocity structure from near-vertical-incidence reflections 63
Velocity structure from synthetic seismograms 63
Accuracy of the velocity models 66
A velocity model from Point L to Point NN 69
SUMMARY 71
REFERENCES 73
TABLES 75

1. INTRODUCTION

This report contains the results of a series of seismic experiments conducted in September, 1986 to determine the seismic structure of oceanic sediments in an area about 200 km ESE of Madeira (Figure 1). The work was carried out over six days during RRS Discovery Cruise 161 (WHITMARSH 1986). The work area was chosen by the Admiralty Research Establishment (ARE), Portland so that we would obtain data to assist their interpretation of a series of acoustic propagation experiments conducted along a NE-SW profile between Madeira and the continental margin off Morocco (Figure 2). The experiments to be described were concentrated at three locations, Points L, MM and NN (Figure 2). A number of wide-angle seismic profiles extended SW or NE from the above points at which ocean-bottom seismographs were also deployed.

The ARE profile lies in depths of 4300 to 4400 metres. It is bounded to the southeast by the foot of the roughly linear slope on the seaward edge of the complex continental borderland of Morocco. To the northeast lies the Seine Abyssal Plain which is separated from the work area by a low sill at about 33°N. To the westsouthwest the sea-floor deepens steadily towards the Madeira Abyssal Plain and the Canary Basin (both over 5200 m deep) some 700 km away. Finally to the northwest lies the linear NE-SW slope at the foot of the Madeira archipelago. It appears therefore that, at least in the recent geological past, the major non-pelagic sediment sources have been the borderland of Morocco south of about 33°N, but including the Agadir Canyon, and the east flank of the rise on which Madeira stands.

The ARE profile also lies between sea-floor spreading magnetic anomalies M21 and M25 and is therefore over Late Jurassic oceanic crust 150 to 156 Ma old (KLITGORD and SCHOUTEN 1986; KENT and GRADSTEIN 1986). A number of boreholes were drilled in the region by the Deep Sea Drilling Project (DSDP) on Legs 14, 50 and 79 (HAYES, PIMM et al. 1972; LANCELOT, WINTERER, et al, 1980; HINZ, WINTERER et al. 1984). However, the majority of these were drilled on the continental borderland off Morocco where the geological history has been strongly influenced by processes associated with the continental margin alone. The only nearby deep ocean hole was drilled at Site 136 about 170 km NNE of Madeira (HAYES, PIMM et al 1972). Even here the 308 m thick sediment column

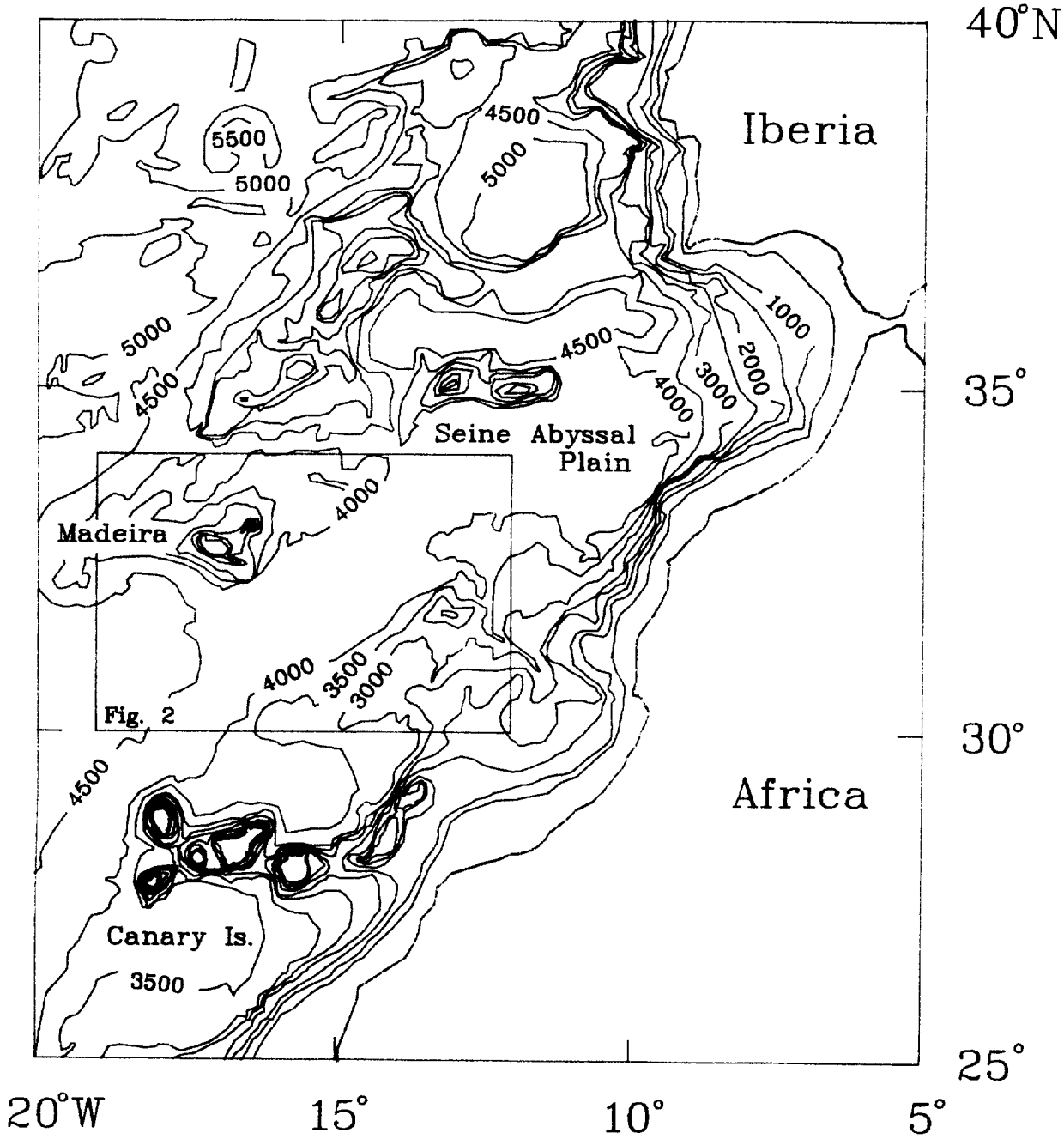

Figure 1: Bathymetric chart of part of the eastern North Atlantic Ocean (contours in metres). Box shows location of work area.

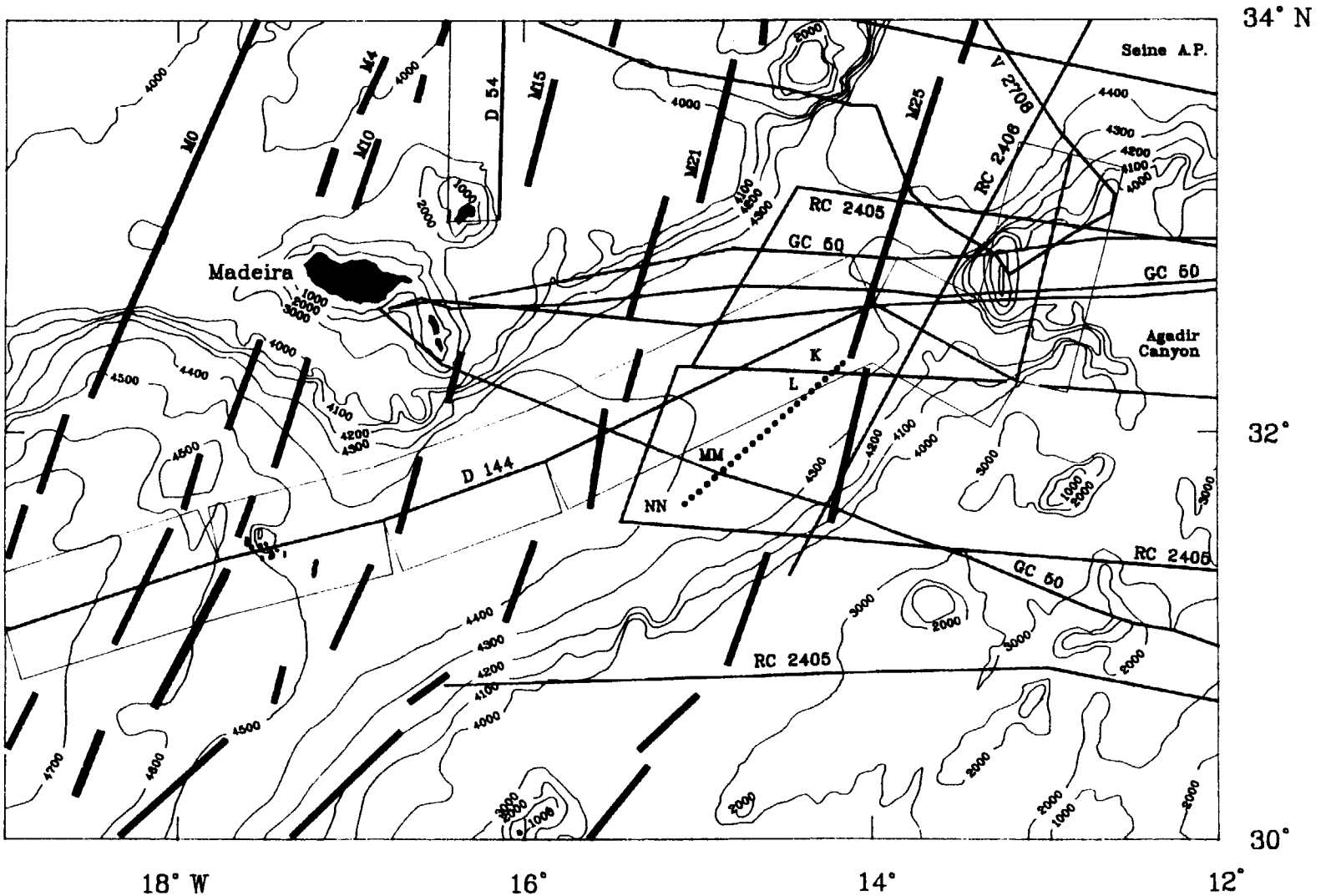

Figure 2: Bathymetric chart of the work area (contours in metres). Dotted line = profile studied in this report (L, MM and NN were three points of intense investigation); thick lines = magnetic isochrons (Klitgord and Schouten, 1987); medium lines = seismic reflection profile tracks (D = R.R.S. Discovery, GC = D.V. Glomar Challenger, RC = R.S. Robert D.Conrad, V = R.S. Vema). Rectangles bounded by fine lines denote coverage of GLORIA sonographs.

of mainly nannofossil chalk ooze was sampled by only nine cores. A prominent post-Early Pliocene mid-sediment reflector about 100 m downhole, clearly seen on reflection profiles across the north end of the Madeira high, was not sampled. The sediment interval velocity to the ca. 126 Ma old basement was 1.86 km s^{-1}.

The tectonic and palaeoceanographic history of the nearby continental margin and the eastern Atlantic Ocean at this latitude, respectively, have been summarised by EMERY and UCHUPI (1984). Discussion of these topics, while relevant to the sedimentary history of the area, is beyond the scope of this report. Broadly speaking however it may be expected that on oceanic crust of Jurassic age, adjacent to a continent which is subject to normal weathering processes, that the following sedimentary sequence will exist. Firstly draped pelagic sediments deposited near the Mid-Atlantic Ridge crest and above the carbonate-compensation depth (CCD), secondly a layer of clay-rich sediments deposited as the sea-floor sank beneath the CCD (with possibly some interleaving if the CCD varies with time) and thirdly an influx of terrigenous turbidites within the ooze or clay sequence as the abyssal plains extended seawards from the base the continental slope. In addition input of Miocene and later volcaniclastic material is expected to have occurred concurrently with the volcanism which built the island of Madeira.

2. VERTICAL-INCIDENCE SEISMIC REFLECTION PROFILES

Reflection profiles were obtained at 10 kHz, 3.5 kHz and at about 60 Hz.

2.1 Echo-sounder profiles (10 kHz)

The 10 kHz profiles were produced by the ship's precision echo-sounder and show insignificant penetration of the sea-bed. The sea-floor is everywhere smooth and almost flat. No basement outcrops were seen nor are any visible in the vicinity on a nearby GLORIA swath (IOS, unpublished data from Discovery Cruise 144) (Figure 2).

2.2 **3.5 kHz profiles**

The 3.5 kHz profiles were obtained almost continuously using a towed near-surface fish at speeds upto about 10 knots throughout the six day period spent in the work area. The ARE profile is characterised by sediments which, at 3.5 kHz, are not highly reflective and/or are unusually absorptive. Coherent reflections were rarely obtained from below 30 m and typically from not more than 25 m depth below the sea-bed. However inspection of all the records does reveal a systematic progression in record type from NE to SW along the profile (Figure 3). In the vicinity of Point L continuous sub-bottom reflectors are rare and when present they do not extend far along the track (Figure 4a). A 6 to 8 m high sea-floor step, probably a debris flow front, is seen here at 0638/256. Southwest of Point L there is a transitional region which leads into a zone of very well stratified reflections (Figure 4b) which includes Point MM. This zone continues almost as far as Point NN where quite abruptly several sub-bottom reflectors crop out (Figures 4c,d). Further southwest the sediments are quite well stratified but the sea-bed and the shallowest reflectors have a sinusoidal or hummocky appearance with an amplitude of about 5 metres (Figure 4e).

The NE to SW progression described above is consistent with a transition from sediment deposited by slumping to sediments deposited in the distal parts of turbidite flows. The source for such sediment might be the Agadir canyon (Figure 2). The hummocky sea-bed may have resulted from the action of bottom currents, perhaps beyond the reach of recent turbidite flows.

In any event the rather different characters of the 3.5 kHz records at Points L, MM and NN indicate that the sea-bed at these places will give rise to different acoustic responses at frequencies of a few kilohertz.

2.3 **Airgun reflection profiles (about 60 Hz)**

A continuous seismic reflection profile was obtained from Points K to NN (Figure 2). The source was a 300 ins^3 airgun fired every 13 secs. A waveshape kit, which suppresses air bubble oscillations, was used on the gun to enhance the depth resolution of the records. The signals from the two 25 metre-long active sections in the towed array were summed and displayed after appropriate band-pass filtering.

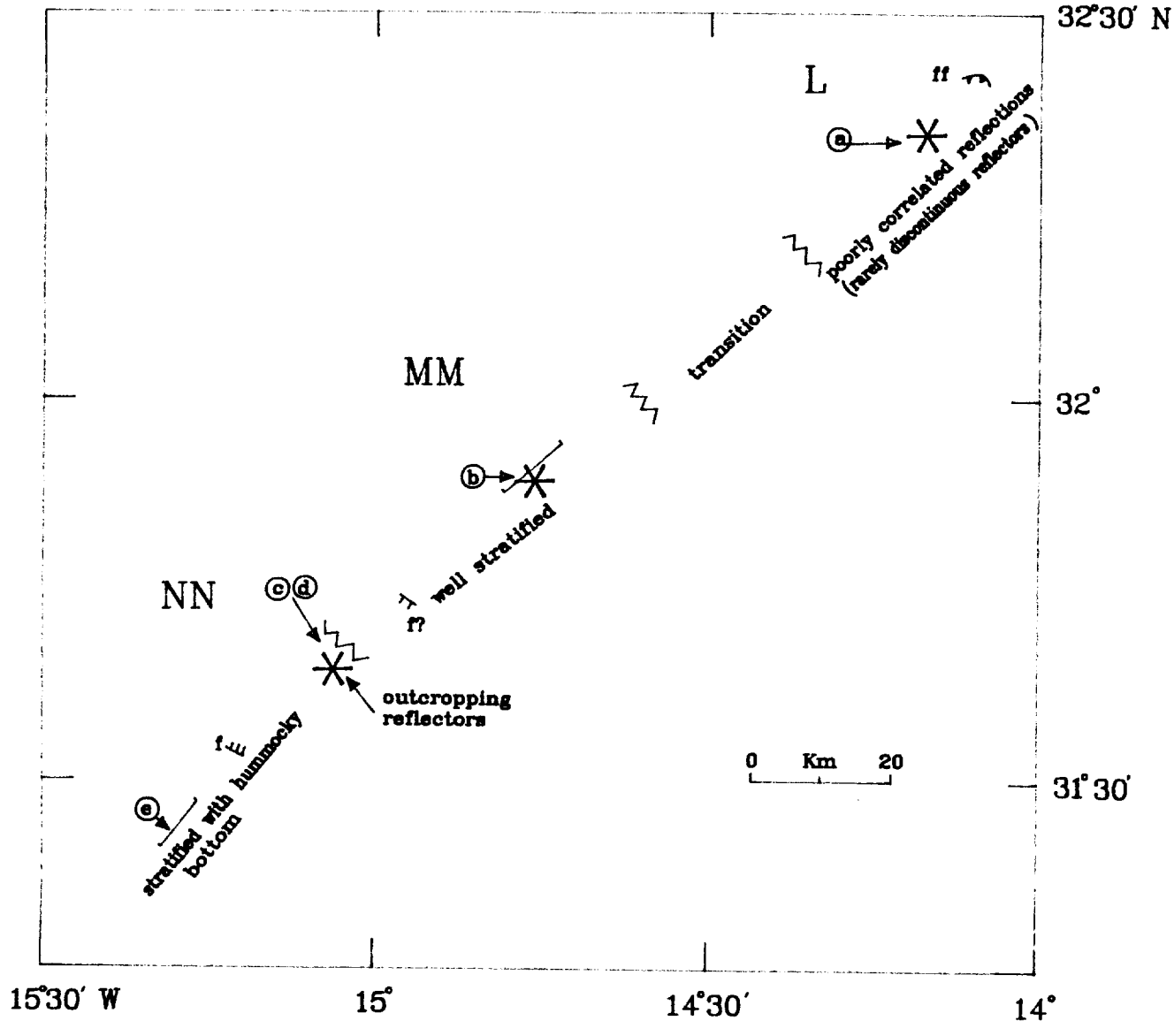

Figure 3: Summary of the character of the 3.5 kHz records along the profile. Stars = locations of Point L, MM, and NN; a, b, c, d and e = locations of records in Figure 4. f = fault; ff = flow front.

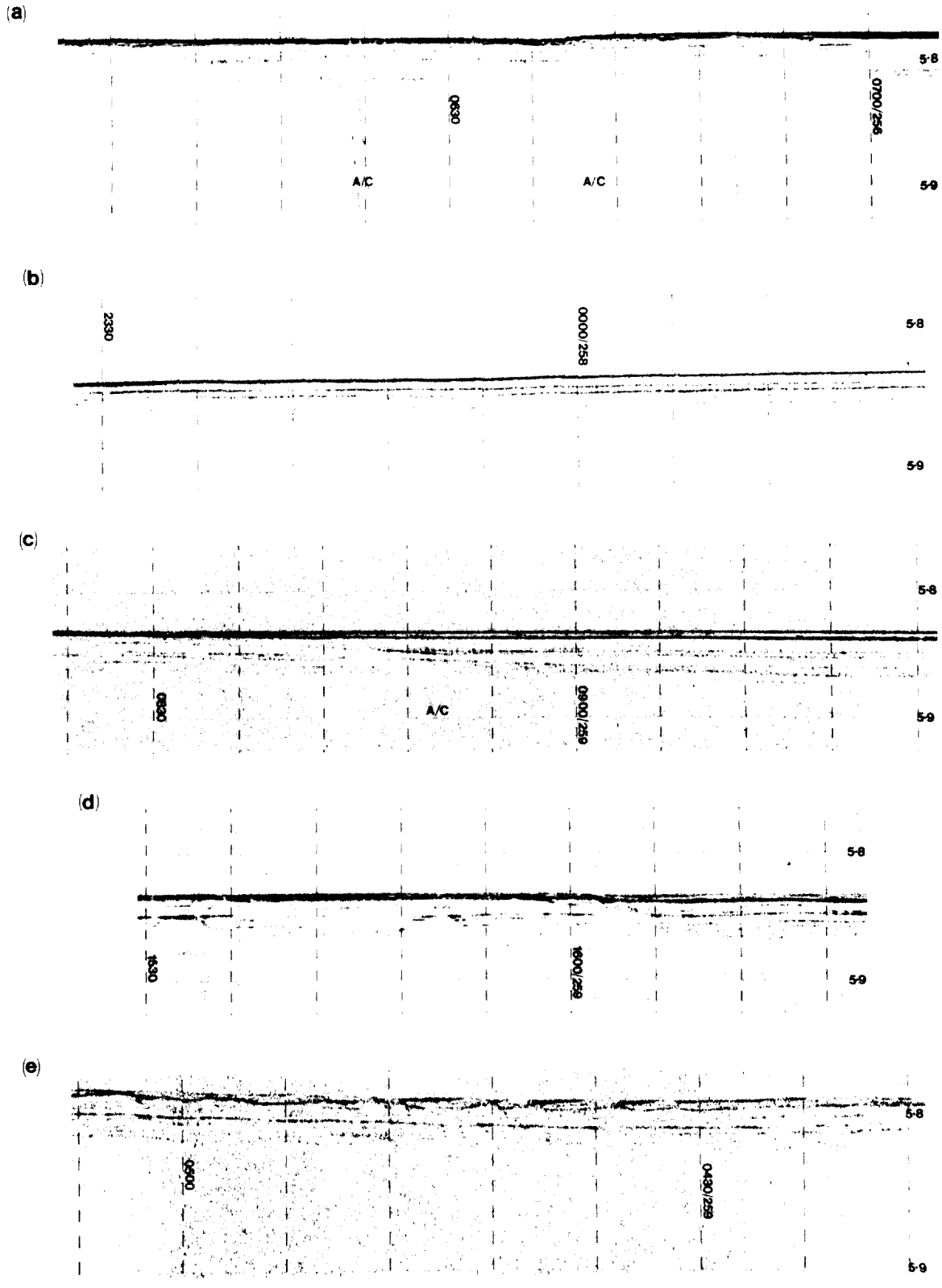

Figure 4: Characteristic 3.5 kHz profiles obtained at a variety of speeds and courses. For locations of a, b, c, d and e see Figure 3. Vertical scale, seconds (two-way time).

The profile is presented in Figure 5. Oceanic basement (Reflector e) is clearly visible everywhere and the sediment thickness varies from 0.75 to 1.85 s, roughly 700 to 1700 m. The greatest basement relief (1.1 s) occurs just SW of Point MM and this may correspond to one of the minor fracture zones indicated by KLITGORD and SCHOUTEN (1986).

Within the sediments four distinctive boundaries are seen (Figure 5). Reflectors c and d parallel each other and the sub-c sediments appear to be draped over the basement topography. These sediments are also relatively weakly stratified. Reflector c is offset in places by small normal faults. Above Reflector c there are three distinct sequences of well-stratified sediment each having a clear angular unconformity with the immediately underlying beds. The second and third sequences are gently folded whereas the first sequence is not. The first sequence has a component of thickening to the SW and the second sequence to the NE. One can only speculate as to the ages and origins of the changing geological and tectonic circumstances which produced the above relationships. It is possible to state with some confidence however, in the light of experience elsewhere, that the sediments below Reflector c are almost entirely pelagic and will consist of calcareous ooze or chalk, at least towards the basement. Sequences one to three are strongly influenced by turbidites of uncertain origin and composition.

Other mainly unpublished, reflection profiles exist which cross the region adjacent to the ARE profile (Figure 2). A profile of WINTERER et al (1980), obtained during DSDP Leg 50, crosses the profile in Figure 5 near Point MM. It shows a locally strong reflector at 0.37 sec (i.e. close to Reflector b) but lacks penetration and resolution to provide further information. Other profiles north of Point L appear to show Reflector b at about 0.75 sec depth. A series of potentially very informative multichannel reflection profiles were obtained during Robert D. Conrad cruises 2405 and 2406 (Figure 2) (ANON., 1983). Unfortunately the only one of these profiles so far published lies north of the sill on the southern edge of Seine Abyssal Plain (ANON., 1983) and is therefore in a different depositional province. However it has many similarities with our

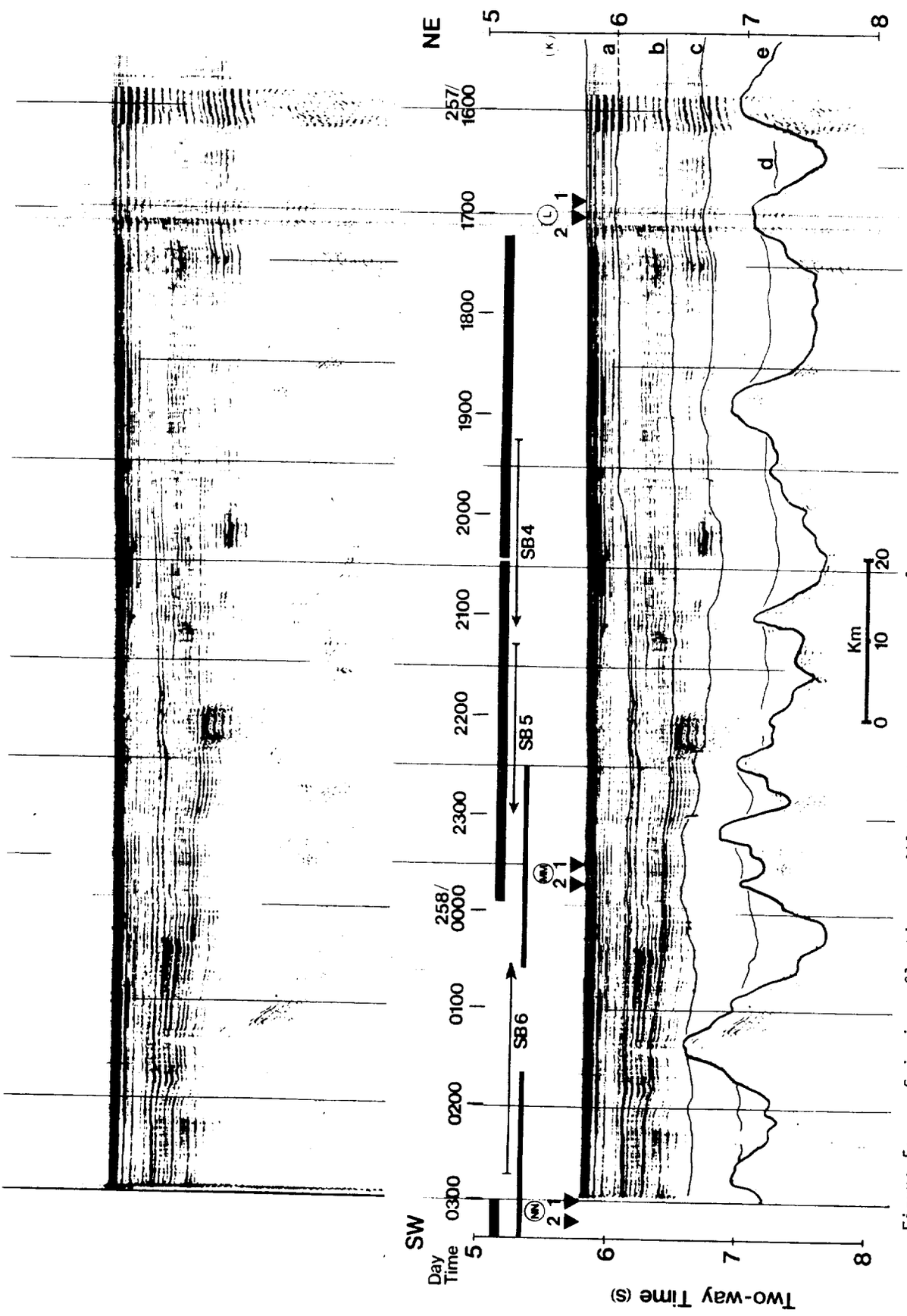

Figure 5: Seismic reflection profile obtained with a 300 ins³ airgun and waveshape kit. See Figure 2 for location. The lower part of the figure indicate the position of volcanic basement and several reflectors within the sediments. Thick bars = extent of wide-angle refraction profiles shot with 4 x 1000 ins³ airguns; thin bars = extent of near-vertical-incidence profiles shot with 300 ins³ airgun and waveship kit. SB = sonobuoy; triangle = DOBS location.

profile in that there is a weakly reflective lower section and a highly stratified upper section, the lower part of which is folded. MOUNTAIN and HAYES (1985), in a preliminary assessment of the Conrad data, also note faults in the sediments, some of which displace the sea-floor on 3.5 kHz records.

3. THE WIDE-ANGLE SEISMIC REFLECTION/SEISMIC REFRACTION TECHNIQUE

In the previous section the seismic profiles were obtained by transmitting energy from a variety of sources and by observing the returns at essentially vertical incidence from zones of sufficient impedance contrast within the sediments. While yielding a continuous measure along-track of the vertical travel-time to reflecting horizons the technique by itself does not allow the calculation of the seismic velocities to, and the depths of, these horizons. If, however, the horizontal separation of source and receiver is steadily increased then the varying range-dependent travel-times of the different seismic phases do enable velocity and depth to be obtained. This is the principle of the seismic refraction technique.

A curve in time-distance (T/X) space representing the travel-time of a particular seismic phase is called a hodochron. Hodochrons of different phases frequently cross each other. Usually the onset or arrival-time of only the first phase at a given range is well determined; subsequent phases suffer interference from preceding phases including the first phase. Thus the range of source-receiver separations, over which the seismic phase from a given layer of interest arrives first, is important for the study of the layer. One major factor at sea, which influences the range of first arrivals, is the closeness of the source and receiver to the sea-bed. In principle the best way to study the sediments just beneath the sea-bed is to put both the source and the receiver on the sea-bed (Figure 6c). An alternative method, appropriate to the area under discussion, is to use surface sources and bottom receivers (Figure 6b). As the figure shows the sediment arrivals always appear after the first arrivals from the oceanic basement but, because the sediment is relatively thick, most of the sediment and basement arrivals (except those from the uppermost sediment) are sufficiently separated in time for the interference to be potentially unimportant. Lastly it is clear (Figure 6a) that a combination of surface

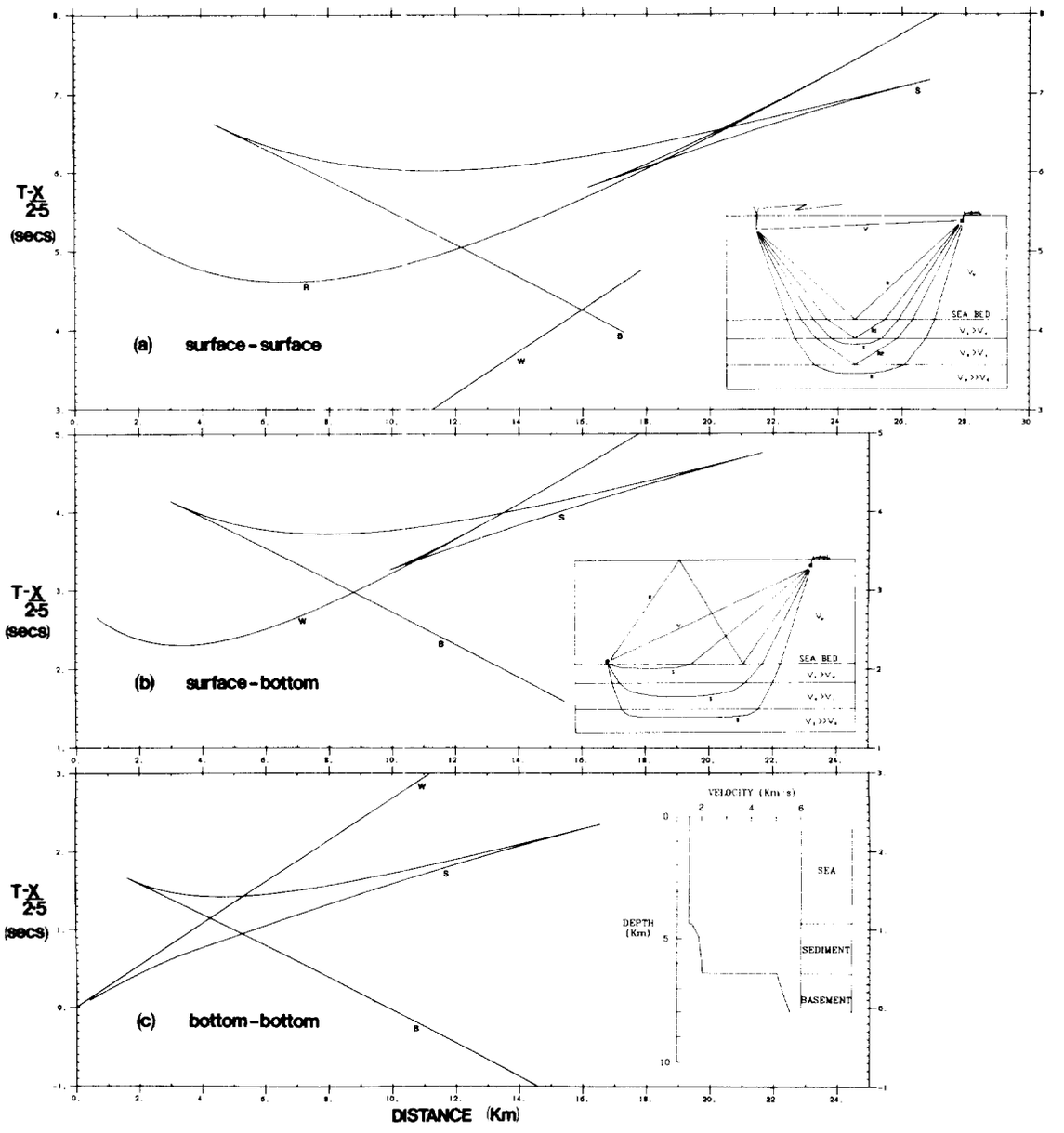

Figure 6: Illustration of the different travel-time curves which are obtained over normal oceanic crust with various combinations of surface and bottom sources and receivers.

sources and receivers is less suitable to study the sediments; sediment arrivals are observed ahead of the strong bottom reflection over a shorter distance and the weaker direct-sound water-wave may also interfere with the sediment arrivals at longer ranges. However, as will be shown, a near surface airgun and sonobuoy can provide useful constraints on the interval velocities between sediment reflectors.

3.1 **Observational techniques**

In practice the deployment of sea-bed receivers is achieved using ocean-bottom seismographs (OBS), a technique which has been used for many years (WHITMARSH and LILWALL 1981); in particular we used a set of digital OBS (or DOBS) built at I.O.S. (PEAL and KIRK 1983). Both near-surface airguns and a small number of experimental 1.7 kg bottom charges were fired to the DOBS. Unfortunately the charge sizes were generally too small to generate sufficient energy at about 4400 m depth. The principal results to be presented are therefore from the airguns. Two types of airgun source were fired every 2 minutes (a) 4 x 1000 cubic inch (16 litre) guns and (b) a 300 cubic inch (4.8 litre) gun with waveshape kit (WSK). The larger guns were fired out to 25 to 30 km range in order to penetrate the sediments and oceanic crust. The smaller gun was used at shorter ranges to study near-vertical-incidence reflections from within the sediments so as to obtain estimates of interval velocities.

Three disposable sonobuoys were also used, in between the DOBS locations and usually during normal reflection profiling, with the 300 cubic inch gun and WSK as source, to provide useful additional interval-velocity data. This technique, although it uses a near-surface receiver, has the advantage, when studying near vertical-incidence reflections, of a zero initial horizontal source-receiver separation. Navigational difficulties usually preclude this when DOBS are used as receivers.

3.2 **Data presentation**

Seismic refraction data is normally displayed as record sections. A record section is a representation in time-distance (T/X) space of all the seismic wiggly-line traces recorded by a particular sensor from one or more receivers during a refraction profile. The traces are positioned along the distance axis at the appropriate source-receiver horizontal separation or range.

The absolute amplitude scaling of the traces is chosen arbitrarily but their relative amplitudes are often proportional to range to correct crudely for spreading and other transmission losses. Ranges are calculated by standard techniques from the travel-time of the direct-sound waterwave (WHITMARSH et al 1986). Time corrections are made also for any drift of the DOBS clock with respect to the shipboard clock used to time the source emissions.

In order to exaggerate the relative velocity, or slope, differences of the primary arrivals on a record-section the vertical (time) axis is usually chosen to be the reduced travel-time (T-X/VR) where,

T = time since the source fired (s)
X = horizontal range (km)
VR = reduction velocity (km s^{-1})

Thus arrivals with a velocity VR will lie parallel to the distance exis. An example of a record section recorded by a DOBS is given in Figure 7.

4. ANALYSIS OF THE RECORD SECTIONS

Individual seismic traces contain phase, amplitude and frequency information and the ease with which these three parameters can be related to earth structure decreases in that order. The simplest models of the earth are those which assume lateral homogeneity (i.e. isotropic laterally-uniform horizontal layers) along a seismic profile. In many instances this is sufficient to allow an adequate explanation of seismic observations. Lateral homogeneity of the sediment velocity structure is assumed here, not only because the reflection profile (Figure 5) indicates it, but also because the experiments were designed on that assumption and do not provide data to constrain laterally heterogeneous models.

4.1 **Modelling travel time**

The starting point in interpreting any record section is to identify the major phases and to discover models which fit their arrival times. The latter is simple but the models are also non-unique. For example it is not possible, from travel-times alone, to distinguish between models with first and second order discontinuities in the velocity structure (Figure 8). In Figure 8 both the calculated hodochrons, from two dissimilar velocity structures, fit the "observed" points to within normal picking errors of about ± 0.02 secs. Travel-times were calculated using a version of the WKBJ program written by CHAPMAN (1978). The program has the advantage that the travel-time along any specified multiple path can be treated as well as along the primary ray-paths.

4.2 **Modelling amplitudes**

Far greater confidence in the uniqueness of velocity models is achieved if the amplitudes of all the major phases on the record section are modelled. The best, though computationally most lengthy, technique uses the reflectivity method of FUCHS and MUELLER (1971). The technique has the advantage that the total response, i.e. including all multiples and conversions, of a stack of uniform isovelocity layers is computed. A slight disadvantage is that a transmission zone, through which only travel-times are computed, necessarily separates the source and receiver from the underlying reflectivity zone for which the total response is to be computed. In practice the transmission zone may be about only one wavelength in thickness.

Modelling amplitudes with synthetic seismograms is a difficult and time-consuming business because no clear algorithm exists to find the 'best fit'. Intuition and empiricism have their place here. One reason for this is the sensitivity of the amplitudes of the synthetic seismograms to quite small changes in the velocity structure. Conversely this method provides a good deal of confidence in a structure once a 'best fit' has been achieved.

4.3 **Modelling procedure**

A variety of modelling procedures and types of data (Table 1) will be presented in the remainder of the report.

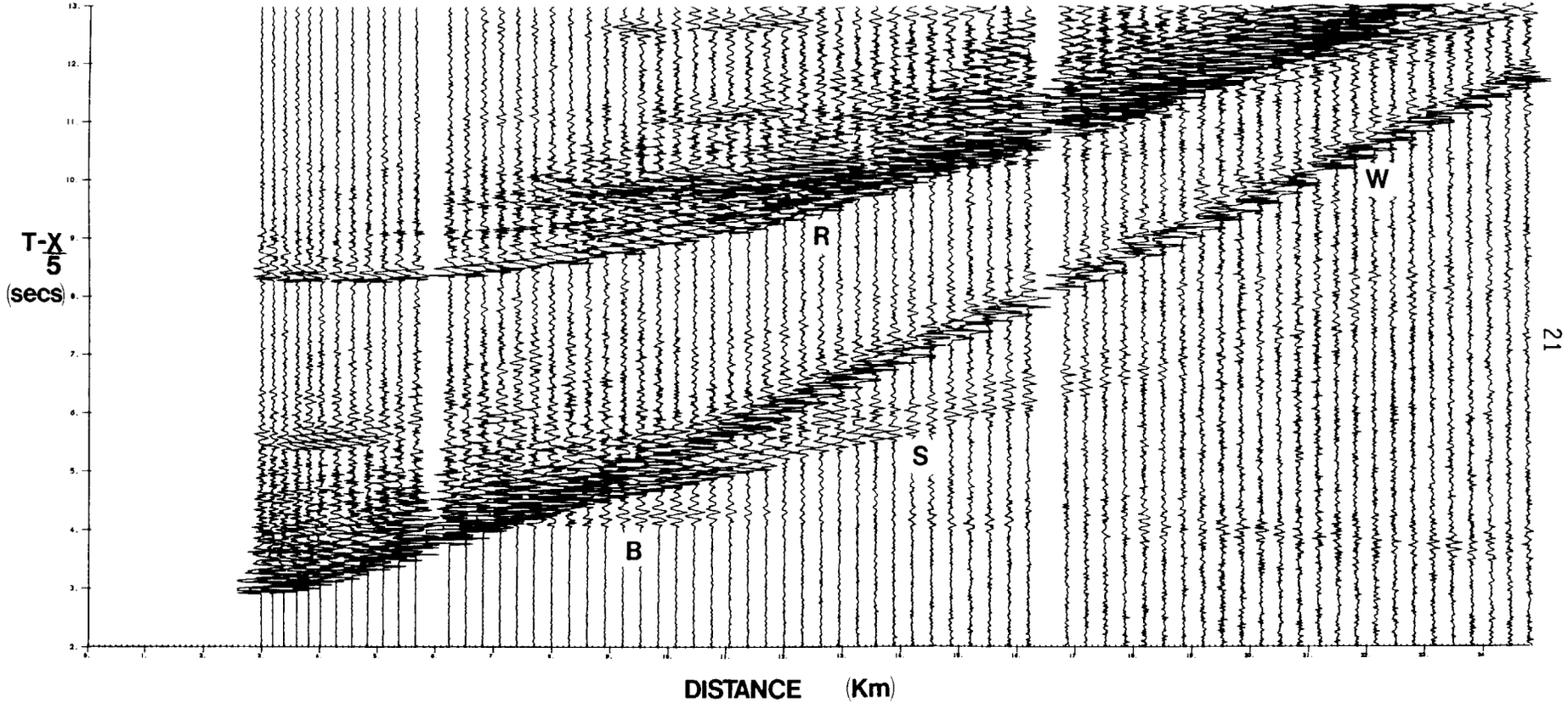

Figure 7: Typical unfiltered vertical geophone channel DOBS record section plotted with a reduction velocity of 5 km s^{-1}. The trace amplitudes have been multiplied by a factor proportional to their range. W and R are direct and bottom-surface reflected water-waves, respectively. S and B are sediment and basement arrivals, respectively.

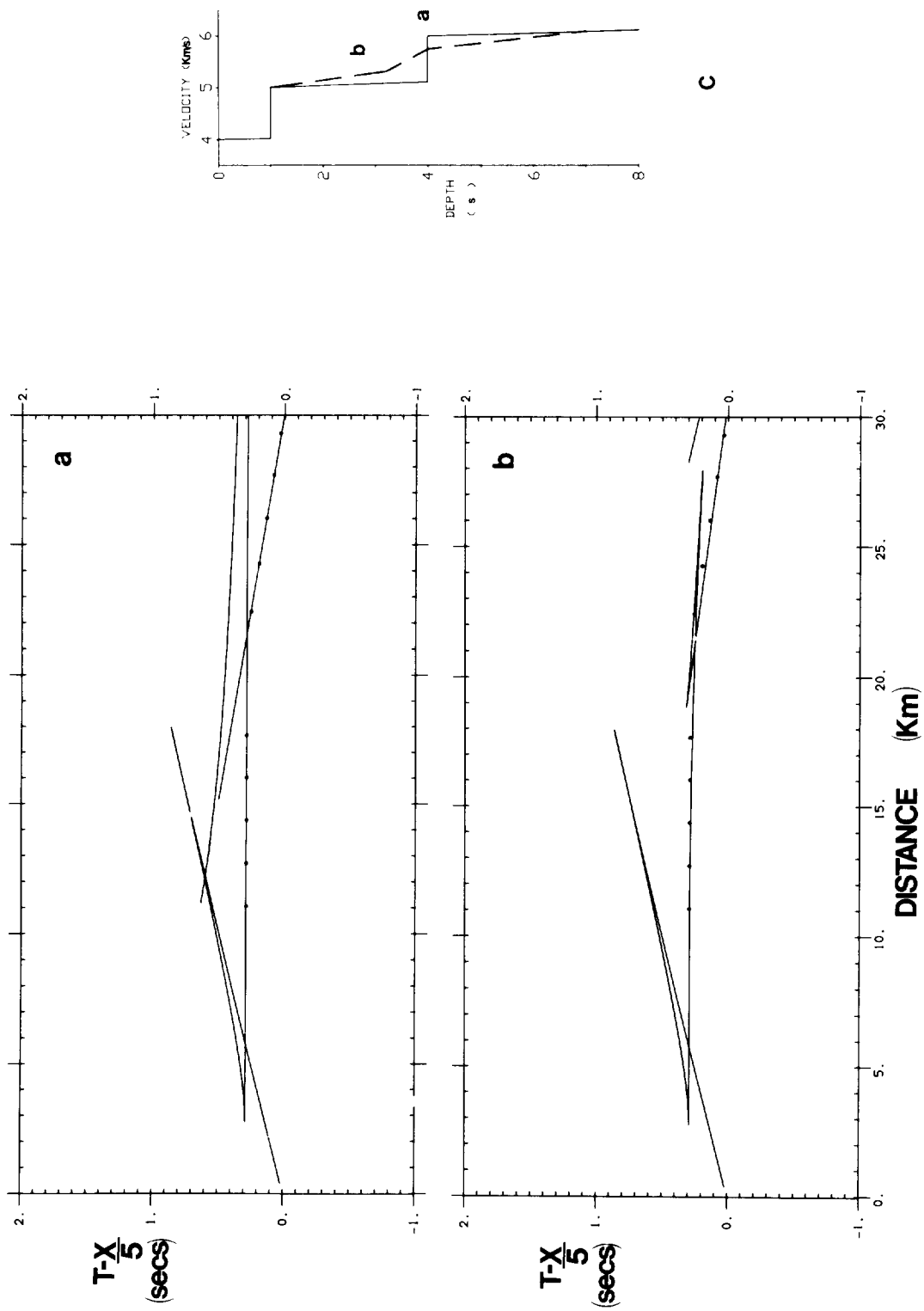

Figure 8: Two different hodochrons (a and b) which "fit" the same set of arrival picks (dots) but are generated from very different velocity/depth models (c).

The procedure for modelling the travel-times of the near-vertical incidence reflections was to use the WKBJ program to fit times picked from the record-sections. When such picks are plotted on a T^2/X^2 plot the points fall close to a straight line. This property makes fitting of the calculated hodochrons to the data much easier than the fitting of hyperbolae in T/X space. A simple algorithm was devised which, by altering the interval velocity and thickness of each layer being modelled, changed the slope and intercept of the hodochron to fit the picks within the accuracy of the observations after only a small number of iterations. Each model was developed from the top down, a deeper layer being added as each successive set of overlying reflections had been successfully modelled. This procedure generates a layered model in which each layer has a constant interval velocity. Such models are necessarily over-simplified but provide an excellent starting point for later, more sophisticated, models.

Amplitude modelling of the wide-angle refractions was preceded by similar WKBJ modelling of the arrival times but this time in T/X space. A 'good fit' was obtained by trial and error after each modification of the velocity/depth model. The next step was to transform the WKBJ model, consisting of linear gradients between points, to a stepped model consisting of a number of thin constant-velocity layers. In practise such layers need be no thinner than half a wavelength (CHAPMAN and ORCUTT, 1985). The velocity increments of the layers were also chosen to be able to adequately describe any linear gradient less than $4\ s^{-1}$. The transformation was done automatically in software. Reflectivity requires values of shear wave velocity Vs, and density p for each layer, as well as compressional wave velocity Vp. Normally Vs and p are derived from Vp by standard relationships.

In the reflectivity algorithm computation time depends on the trace length, among other things. Thus to reduce computation time the ocean layer is often reduced to a nominal thickness. To a first approximation the resulting synthetic seismograms can be shifted in range and time, according to the geometry of the water raypath, to simulate the real world. This approach was adopted here. A lifelike waveform was obtained by convolving the vertical seismometer Green's function output from the reflectivity program with a wavelet derived from a $4 \times 1000\ ins^3$ direct water-wave (WHITMARSH et al. 1986).

5. RESULTS FROM AROUND POINT L

The work in the vicinity of Point L resulted in the collection of an airgun seismic reflection profile and a seismic refraction profile which was recorded by DOBS 1 and 2. The tracks are shown in Figure 9. The spatial relationship of these two sets of data is also indicated in Figure 10.

5.1 Seismic refraction profiles

The seismic refraction line was shot to the southwest of Point L. 107 shots were fired at 2 minute intervals using an array of 4 x 1000 ins^3 airguns towed at 15 m depth at about 1800 psi. The shots were recorded by DOBS 1 and 2 on the three geophone channels, the hydrophone channel and the water-wave channel.

5.1.1. Ranges

Shot-to-receiver ranges were calculated by the semi-graphical method of WHITMARSH et al. (1986) using direct-sound water-wave arrival times and the soundspeed model in Table 2. This model is based on straight-line segments fitted by eye to point estimates of soundspeed calculated from temperature and salinity measurements down to 4300 m at Discovery II station 3645 (32°16'N, 14°46'W; FUGLISTER 1960) and from temperature observations during XBT cast 7103A to 882 m depth on Day 256, in the vicinity of Point L. A measure of the accuracy of the ranges is given by the consistency of the difference in distance to DOBS 1 and 2. For example the difference fluctuated within a range of only 40 metres for 24 consecutive shots starting 10 kms from DOBS 2 and all but two differences lay within a 20 metre range.

5.1.2. Observations

A complete vertical geophone record section from each DOBS is shown in Figures 11 and 12. These show secondary phases from the sediment layer out to 19 kms and first arrivals from the igneous crust to at least 25 kms. A variety of subcritical reflections and multiple arrivals can also be discerned. For present purposes subsequent analysis will be concentrated solely on the arrivals from the sedimentary layer.

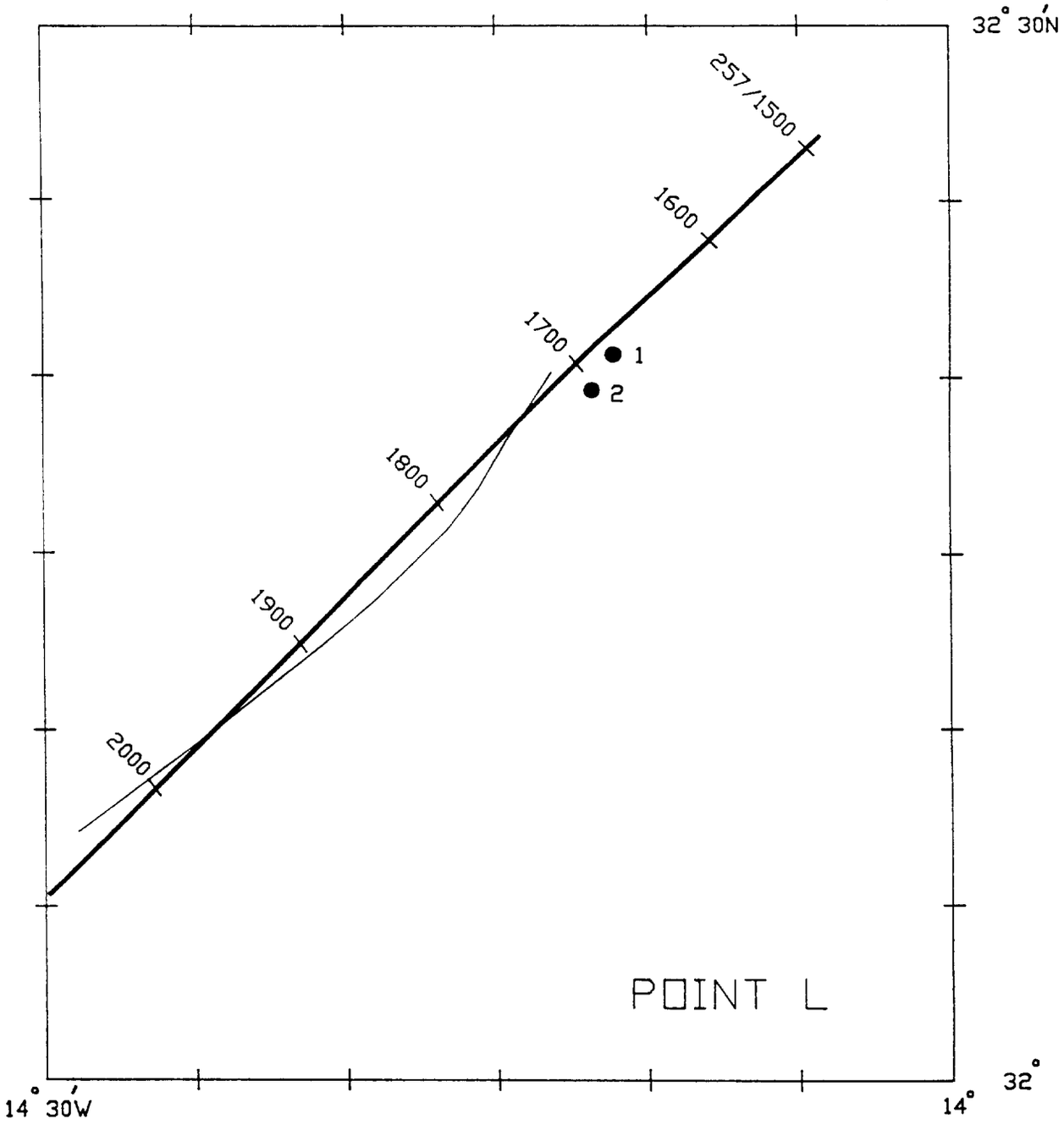

Figure 9: Track of seismic profiles near Point L. Thick line = seismic reflection profile (Figure 10); thin line = wide-angle refraction profile; dots = DOBS.

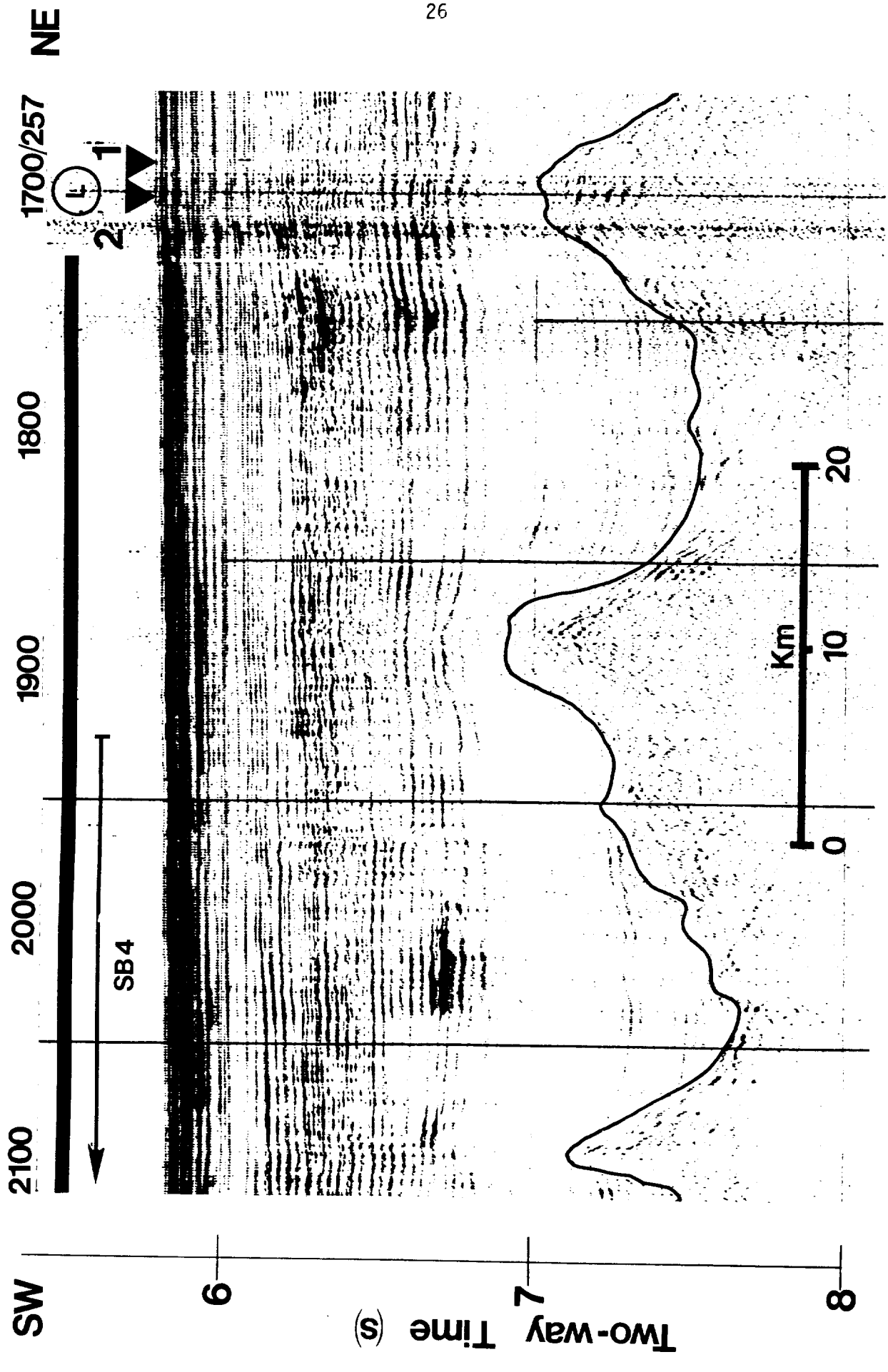

Figure 10: Seismic reflection profile southwest of Point L (see Figure 9 for location; Figure 5 for symbols).

The parts of the record-sections containing the sediment arrivals are displayed at a larger scale in Figure 13. With the parameters used in Figure 13 these arrivals line up roughly parallel to the distance axis, i.e. with a velocity of about 2.5 km s^{-1}. The sediment arrivals never arrive first and at ranges less than about 7.2 km arrive after the direct-sound water-wave. Thus little confidence can be placed on attempts to pick the sediment arrival times or to measure their amplitudes at ranges less than 7.2 km. At larger ranges the sediment arrivals decrease in amplitude with increasing range in a consistent way. Another feature of both record sections is the apparent delay to the onset of the sediment arrival which occurs at DOBS 1 at about 14.8 km and at DOBS 2 at about 15 km. Modelling of the above features will be attempted below.

5.1.3. Lateral structural homogeneity

A comparison of the waveforms recorded by the two DOBS at approximately the same shot-receiver range indicates lateral homogeneity in the seismic velocity structure. The amplitudes and shapes of the sediment arrivals are very similar as is the range at which the delay occurs. It is noticeable however, that the arrival time differences are scattered in the range ± 0.05 s. This indicates that the travel-time variability over distances of about 6 to 17 km through the sea and the sediments is ± 0.035 s.

Another test of lateral variability is to use the two DOBSs as an array to calculate the variation of apparent velocity of sediment arrivals with range. This was done objectively by performing a cross-correlation of pairs of traces from the same shot. The apparent velocity was then calculated directly from the lag required to maximise the cross-correlation function and the range difference of the DOBSs for that shot (Figure 14). Between 9 and 19 km range the best estimate of apparent velocity from travel-time modelling is very close to 2.3 km s^{-1}. The scatter of ± 0.028 s km^{-1} about this mean in Figure 14 is a measure of the variation in travel-time caused by lateral inhomogeneity as well as other factors such as the signal: noise ratio and the sampling rate. An error of 1 in the lag gives an error in ray parameter of about 0.01 s km^{-1}. Thus it seems the scatter is almost entirely due to real variations in arrival times of upto $\pm$ 0.06 seconds between the two DOBSs in rough agreement with the previous estimate. Presumably, due to the ray geometry, most of this variation occurs in the vicinity of the seabed entry point of the ray from the shot.

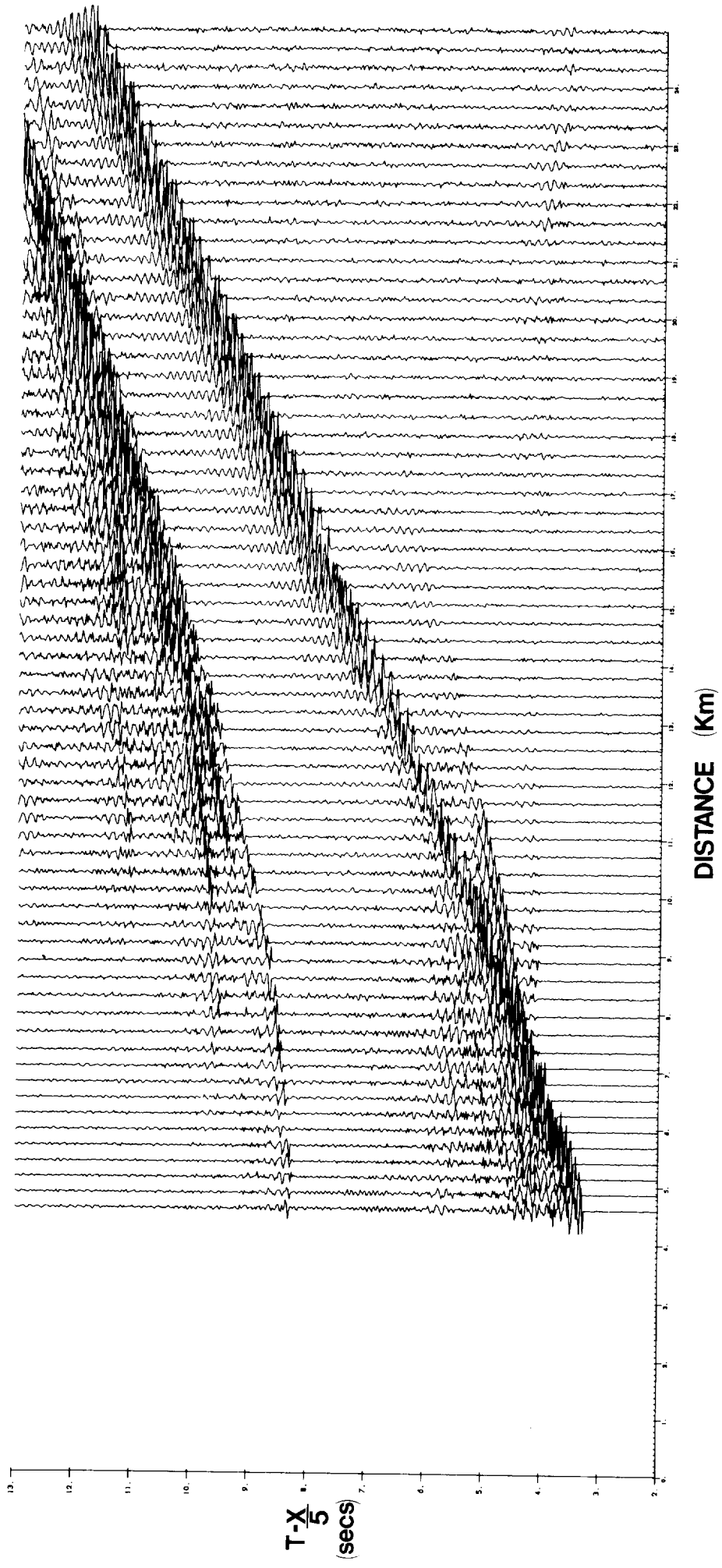

Figure 11: Unfiltered vertical geophone record-section recorded by DOBS1 at Point L. Reduction velocity is 5 km s^{-1}; sampling rate 50 s^{-1}.

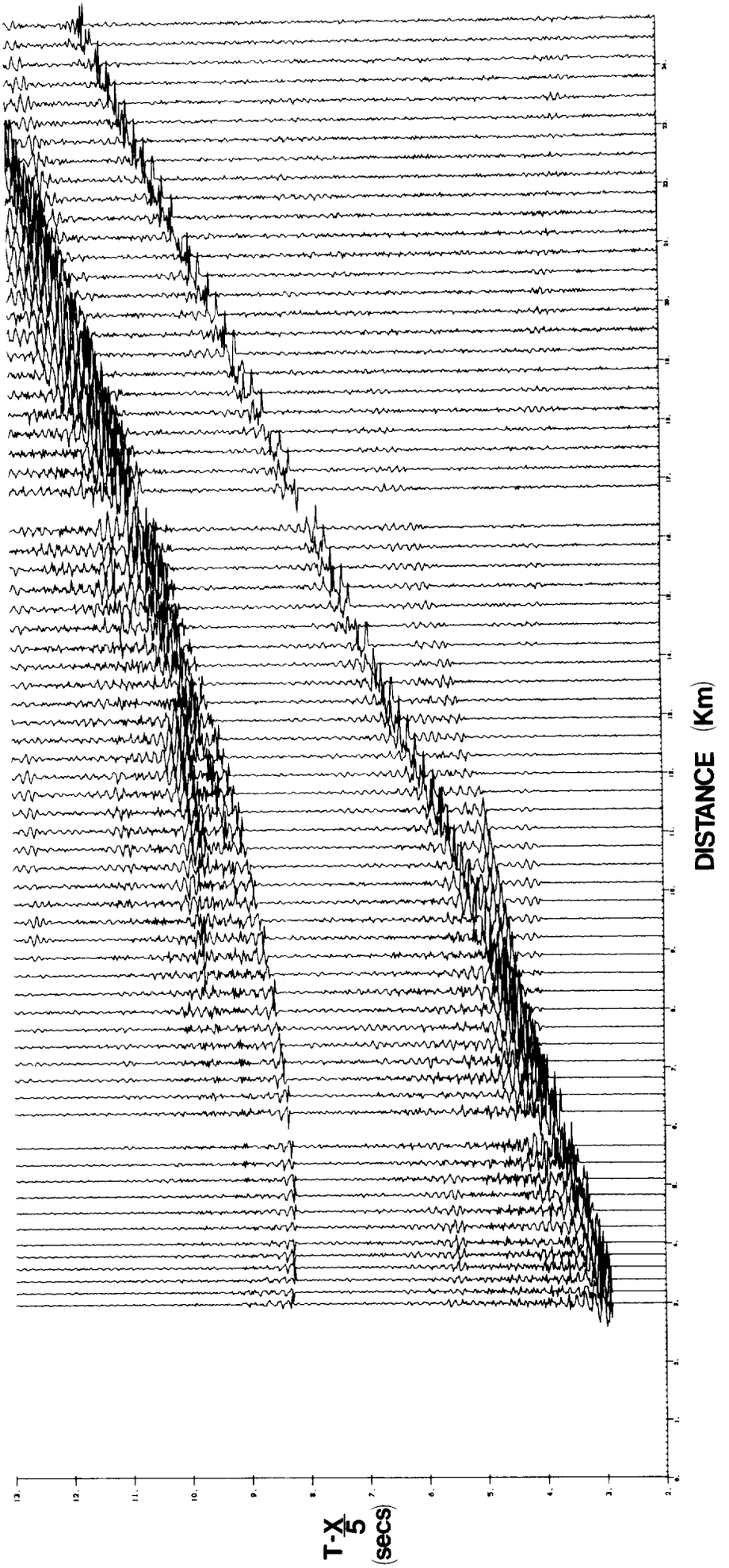

Figure 12: Unfiltered vertical geophone record-section recorded by DOBS2 at Point L. Reduction velocity is 5 km s^{-1}; sampling rate 50 s^{-1}.

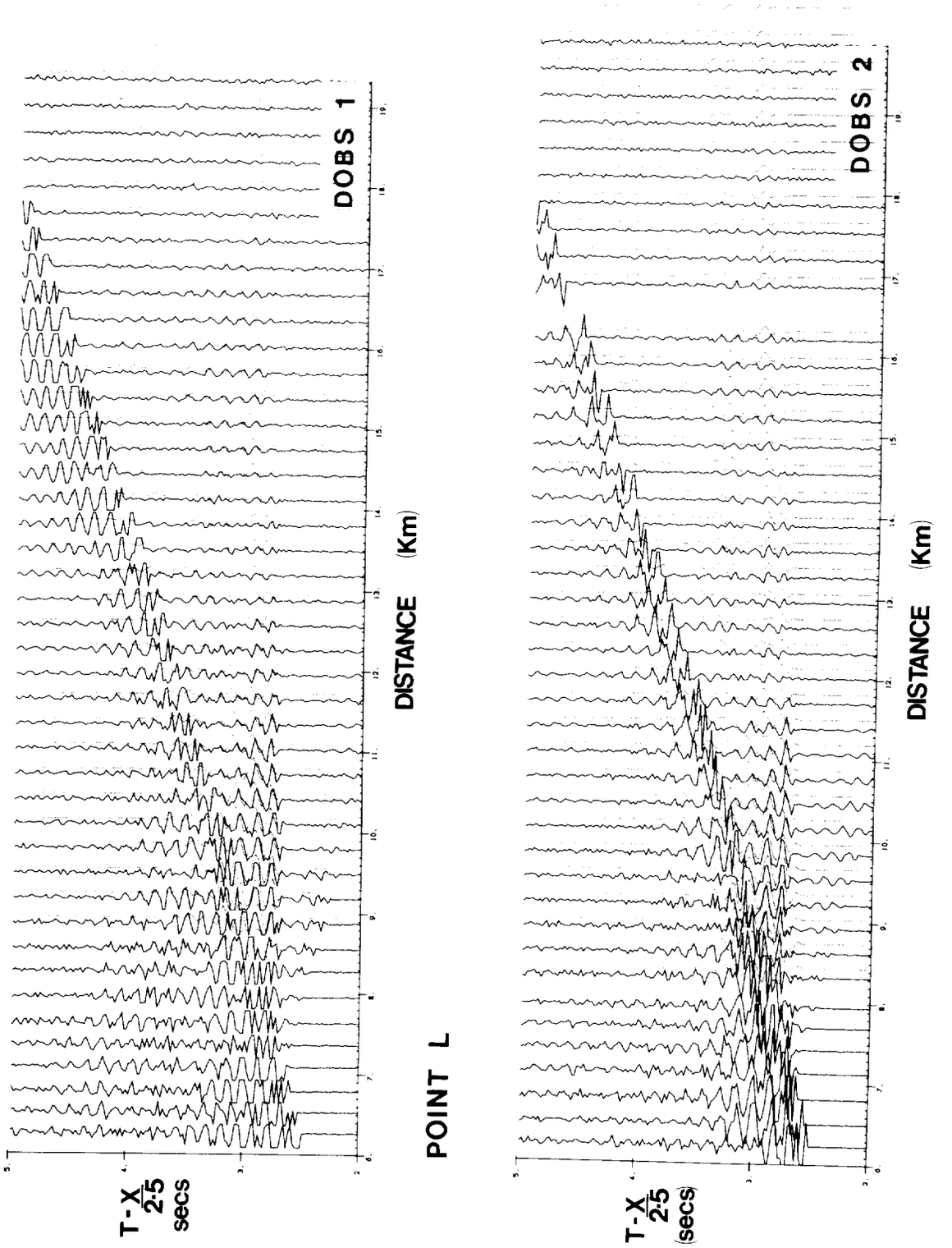

Figure 13: Unfiltered vertical geophone record-sections recorded by DOBS 1 and 2 at Point L. Reduction velocity is 2.5 km s^{-1}. The synthetic seismograms are in red.

5.1.4. Modelling

The first problem was to find an explanation for the offset in sediment arrival-times which occurs around 15 km. In fact there are two associated features which require explanation,

(a) the 0.1 sec difference between two clear sets of sediment arrivals,
(b) the decay in the amplitude of the first set of arrivals so that the first sediment arrival appears to be offset by 0.1 sec at 15 km.

The constraints on suitable models are,

(a) the 2.6 s time intercept of the 2.4 km s^{-1} arrivals which controls the thickness and interval velocity of the layer between the sea-bed and the 2.4 km s^{-1} refractor,
(b) the observation elsewhere in the area that the interval velocity of this layer is about 1.9 km s^{-1}.

There are two types of model which can produce the observed offset of arrivals. The first involves a low-velocity zone. This is unlikely in the present case because assuming lateral homogeneity, each successive set of arrivals should have a greater apparent velocity than the last (Figure 14 indicates the opposite situation viz. velocity decreases around 13 km). The second possibility is that the second arrival group is a multiple of the first. In this case, for multiple refracted arrivals, there will be an abrupt apparent velocity decrease as one passes from one group to the next, as indicated in Figure 14.

The travel-time spent in the upper sediment layer is always so great as to preclude the possibility of the multiples being reflected at the sea-bed. Thus reflection of refracted arrivals <u>within</u> the sediments is indicated. An obvious candidate horizon is the interface between the upper sedimentary layer with an interval velocity of 1.9 km s^{-1} and the underlying 2.4 km s^{-1} layer. A representative model of this type with a sketch of the ray-paths involved is given in Figure 15. Models of this type were developed, using the reflectivity

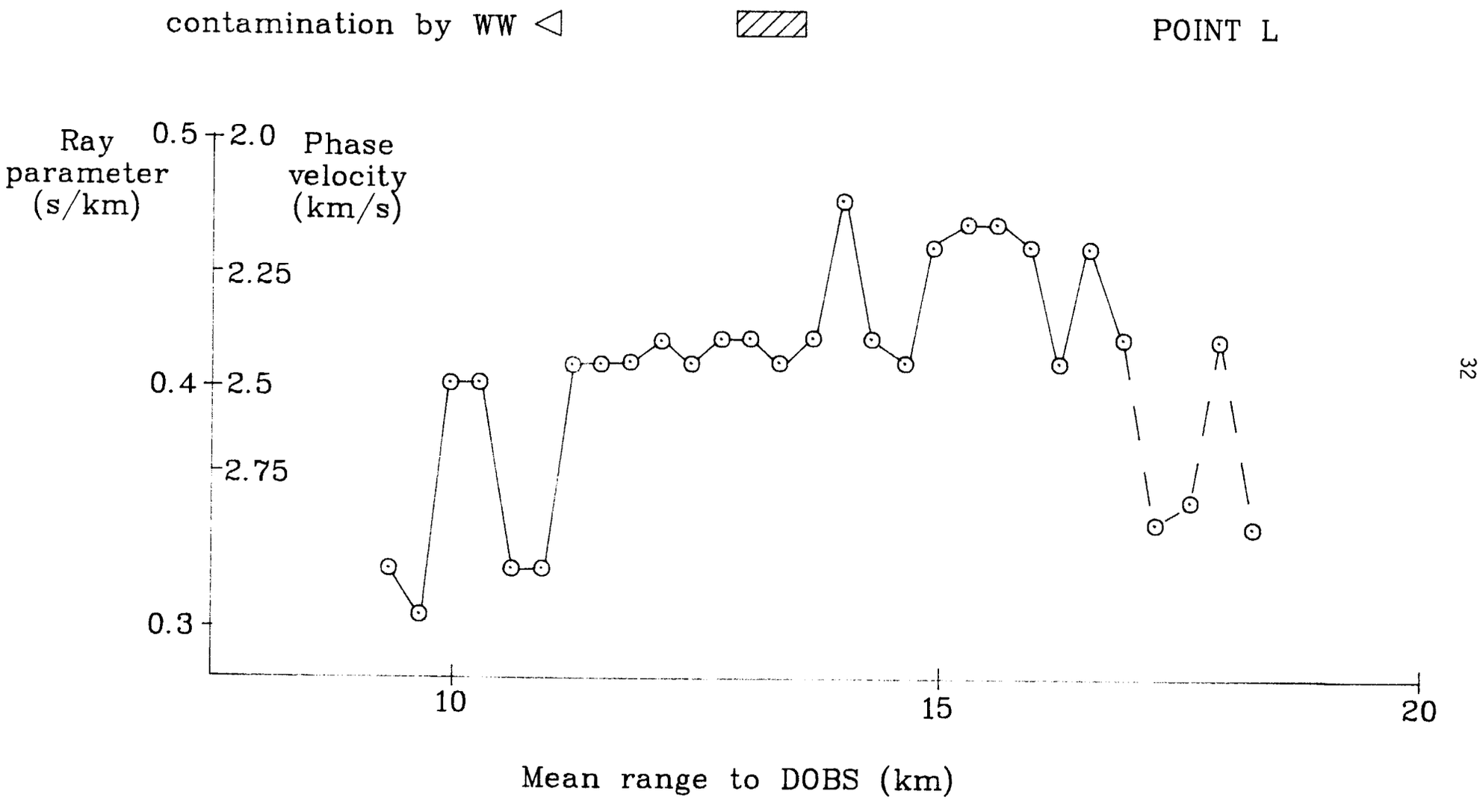

Figure 14: Phase velocity of sediment arrivals across the two DOBS array at Point L. The hachured rectangle marks the transition between the primary arrivals and the first group of multiples. Beyond 17 km noise degraded the calculations.

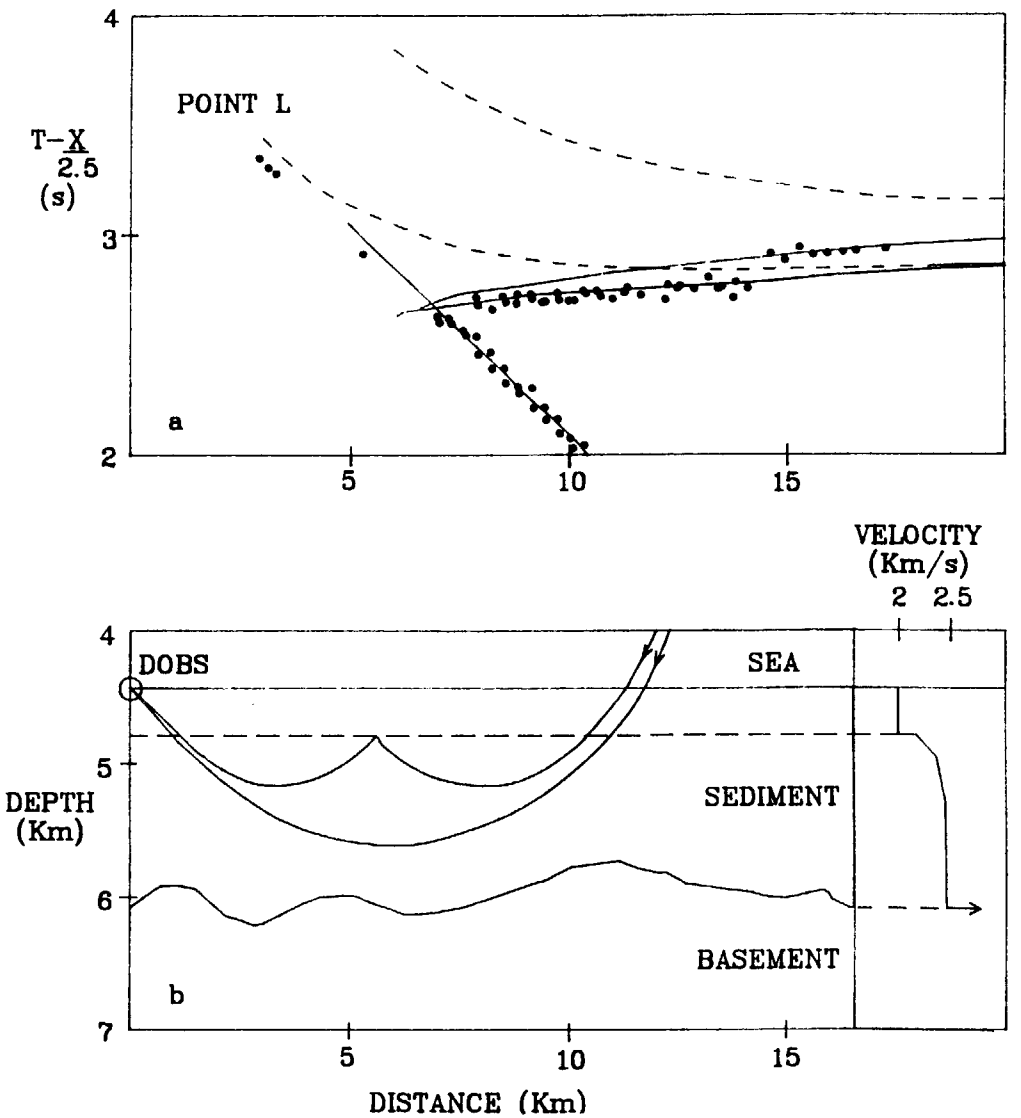

Figure 15: a. Calculated hodochrons which fit the observed arrivals in Figure 13. Two groups of sediment arrivals and a set of basement arrivals are shown. The concave upwards curves represent wide-angle basement reflections. b. Sketch of the types of rays giving rise to the sediment hodochrons in Figure 15a. The multiple refraction is reflected from an interface within the sediments (see velocity structure at right).

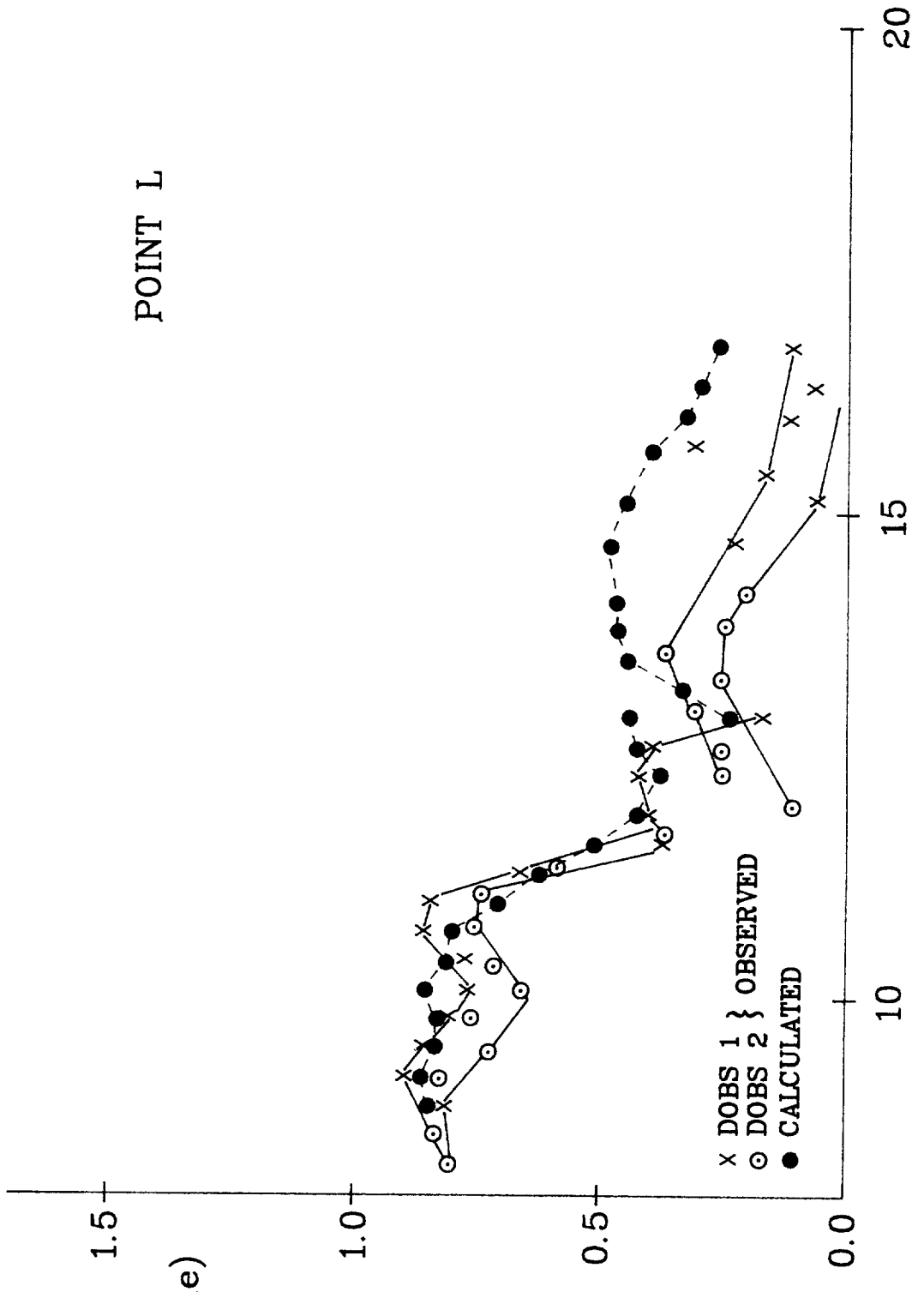

Figure 16: Amplitude/distance plot for sediment synthetic seismograms compared with the seismograms observed at Point L. The continuous line marks the evelope of the observed points.

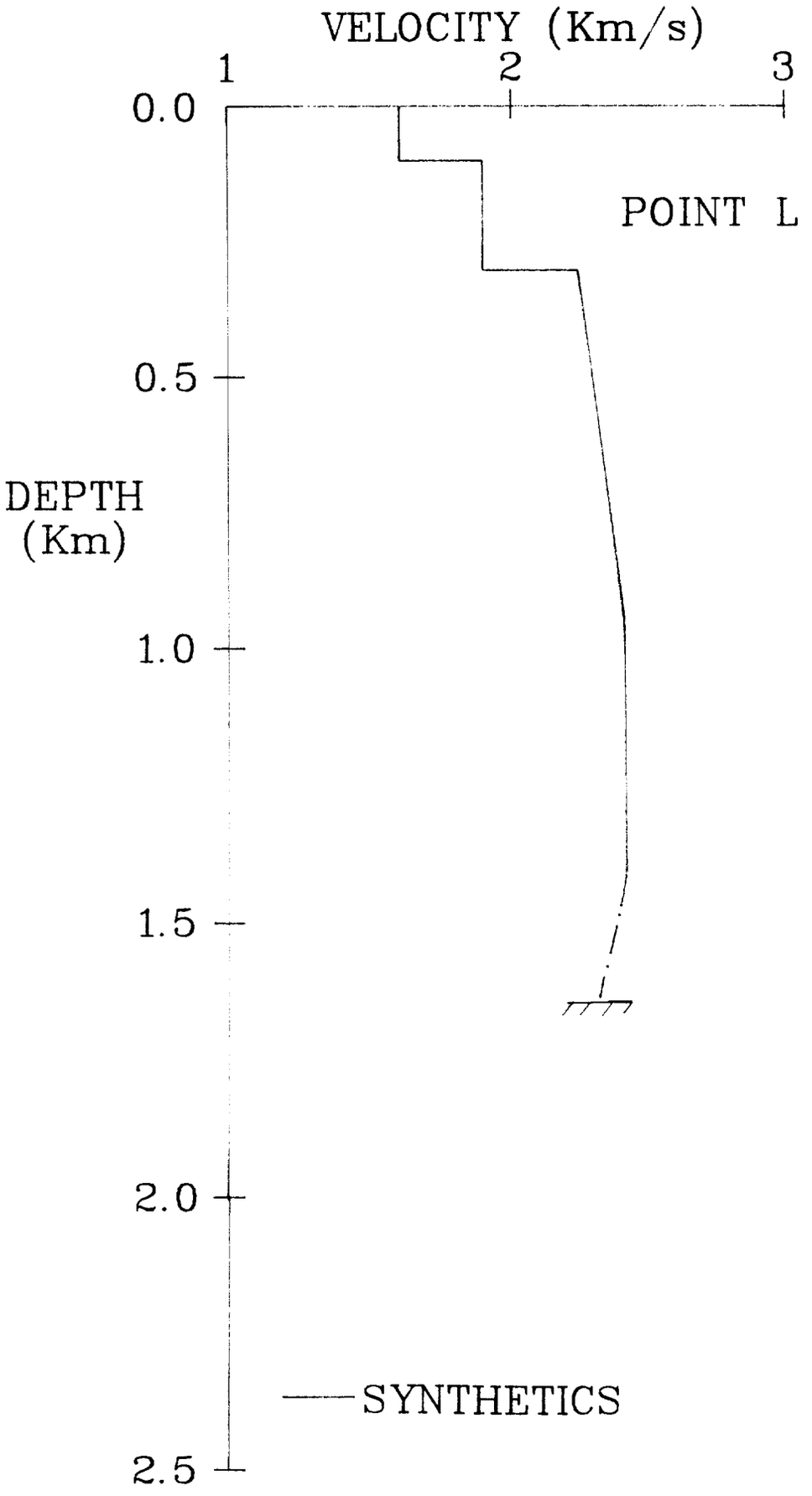

Figure 17: Velocity structure used to obtain the optimum set of synthetic seismograms at Point L. See Table 3 for the detailed structure.

program, in order to reproduce not only the two offset sets of sedimentary arrivals but also their amplitude changes with distance. The peak-trough amplitude of a prominent part of each arrival set in the observed data was picked by cursor on a high-resolution graphics screen. The shape of the amplitude/distance plot for each OBS was remarkably similar (Figure 16). The amplitudes of the corresponding synthetic seismograms were measured on large scale plots. Modelling proceeded until a reasonably close match was obtained to the observed amplitude-distance plot. It should be noted that for simplicity, and because it was not required to be modelled, the volcanic basement has been omitted from these models. If it were included the computation time would have to be doubled, at least, to avoid the noise introduced by 'wraparound' of the multiple reflections from the basement in the synthetic seismograms.

The best velocity model is represented in Figures 13, 16 and 17 and in Table 3. The main characteristics are,

(a) a significant P- and S-wave velocity step at 300 m depth which causes multiples to be reflected within the sediments,

(b) the relatively strong gradient between 300 and 960 m which refracts most of the energy in the observed sediment arrivals back to the sea-bed,

(c) a negative gradient zone at the base of the sediments. This is required to produce the rapid fall-off in amplitude with distance of the primary sediment arrivals (Figure 16). The modelling of the sediment arrivals alone cannot determine the size of the gradient.

(d) The upper sediment 1.9 km s^{-1} layer is required to have a shear-wave velocity nearer 100 m s^{-1} than 500 m s^{-1} to maintain the amplitude distribution in Figure 16. Such relatively low velocities have been measured in situ elsewhere within a few hundred metres of the sea-bed (HAMILTON 1976; WHITMARSH and LILWALL 1982).

6. RESULTS FROM AROUND POINT MM

The work in the vicinity of Point MM resulted in the collection of an airgun seismic reflection profile and two airgun seismic refraction profiles, which were shot with the 4 x 1000 ins^3 array and the 300 ins^3 airgun with WSK respectively, and recorded by DOBS 1 and 2. The tracks are shown in Figure 18. The spatial relationship of the reflection and refraction profiles is indicated in Figure 19.

6.1 Seismic refraction profiles

The 4 x 1000 ins^3 airgun array was towed along a profile northeast of Point MM out to a range of about 37 km. The same firing rate, gun depth and air pressure were used as at Point L. A second shorter profile shot with the 300 ins^3 gun with WSK was obtained to investigate interval velocities between sediment and basement reflectors with the more 'spiky' waveform of this source.

Ranges were calculated for both profiles as for the profile at Point L using the soundspeed model in Table 4. This model is based on straight-line segments fitted by eye to point estimates of soundspeed calculated from temperature and salinity measurements down to 4300 m at Discovery II station 3645 (32°16'N, 14°46'W, FUGLISTER 1960) and from temperature observations during XBT cast 4106A to 566 m depth on Day 259 in the vicinity of Point MM.

6.1.1. Observations

A vertical geophone record section from each DOBS is shown in Figures 20 and 21. These show secondary phases from the sediment layer out to at least 16 km and first arrivals from the igneous crust to at least 25 km. A variety of subcritical reflections and multiple arrivals can also be discerned.

The parts of the record-sections containing the sediment arrivals are displayed at a larger scale in Figure 22. As at Point L the sediment arrivals have phase velocities close to 2.5 km s^{-1}. There is also a fundamental difference in that three groups of arrivals are seen in the ranges 8 - 10.3, 10.5 - 13 and beyond 13 km. Each group is delayed in time by roughly 0.2 sec with respect to the previous group. These same characteristics are seen on both DOBS record-sections and at about the same range so that it may be concluded that they are functions of the velocity/depth structure and are not the result of lateral inhomogeneities.

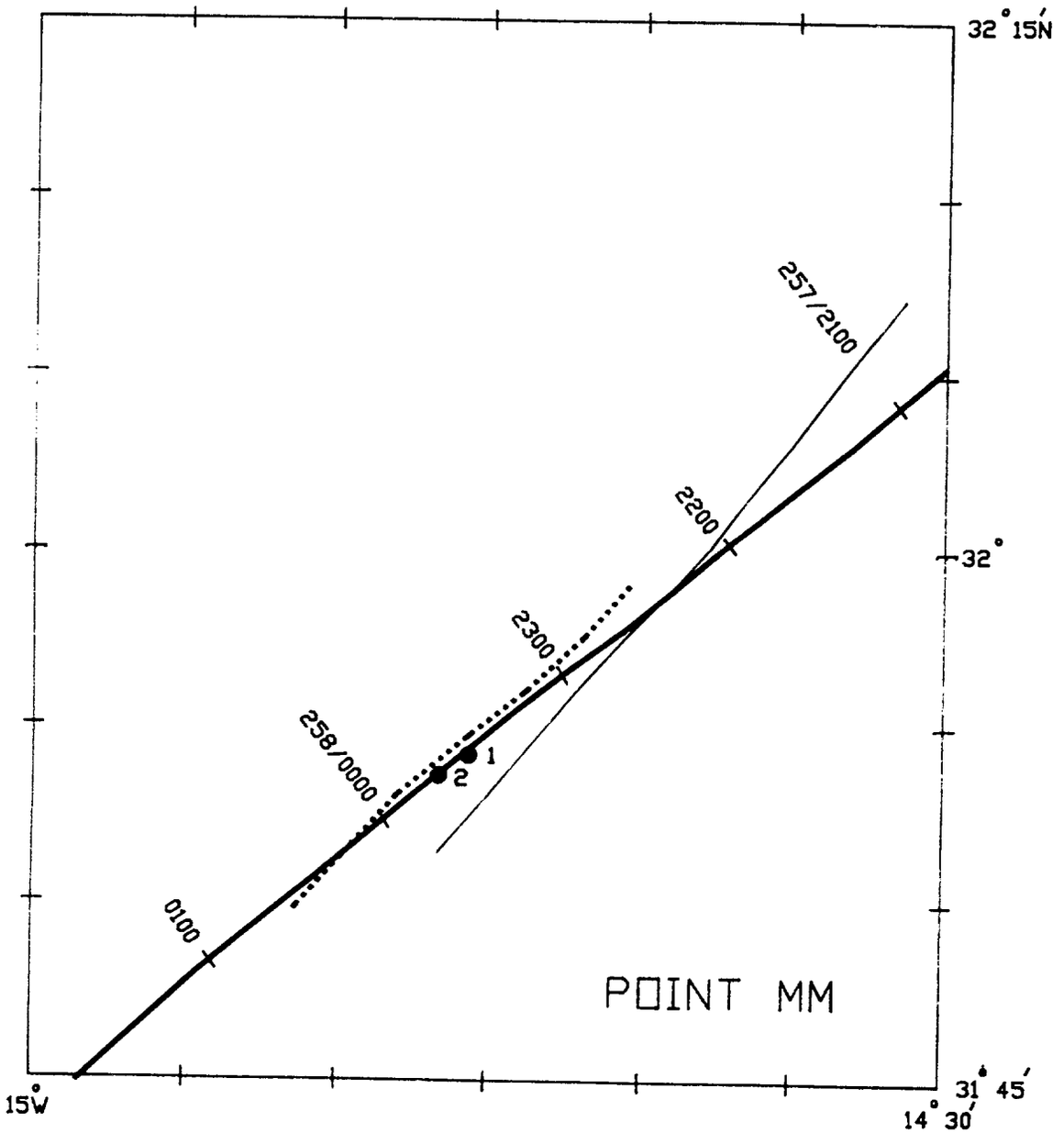

Figure 18: Track of seismic profiles near Point MM. Thick line = seismic reflection profile (Figure 19); thin line = wide-angle refraction profile; dotted line = near-vertical incidence reflection profile shot with 300 ins^3 airgun and wave shape kit; dots = DOBS.

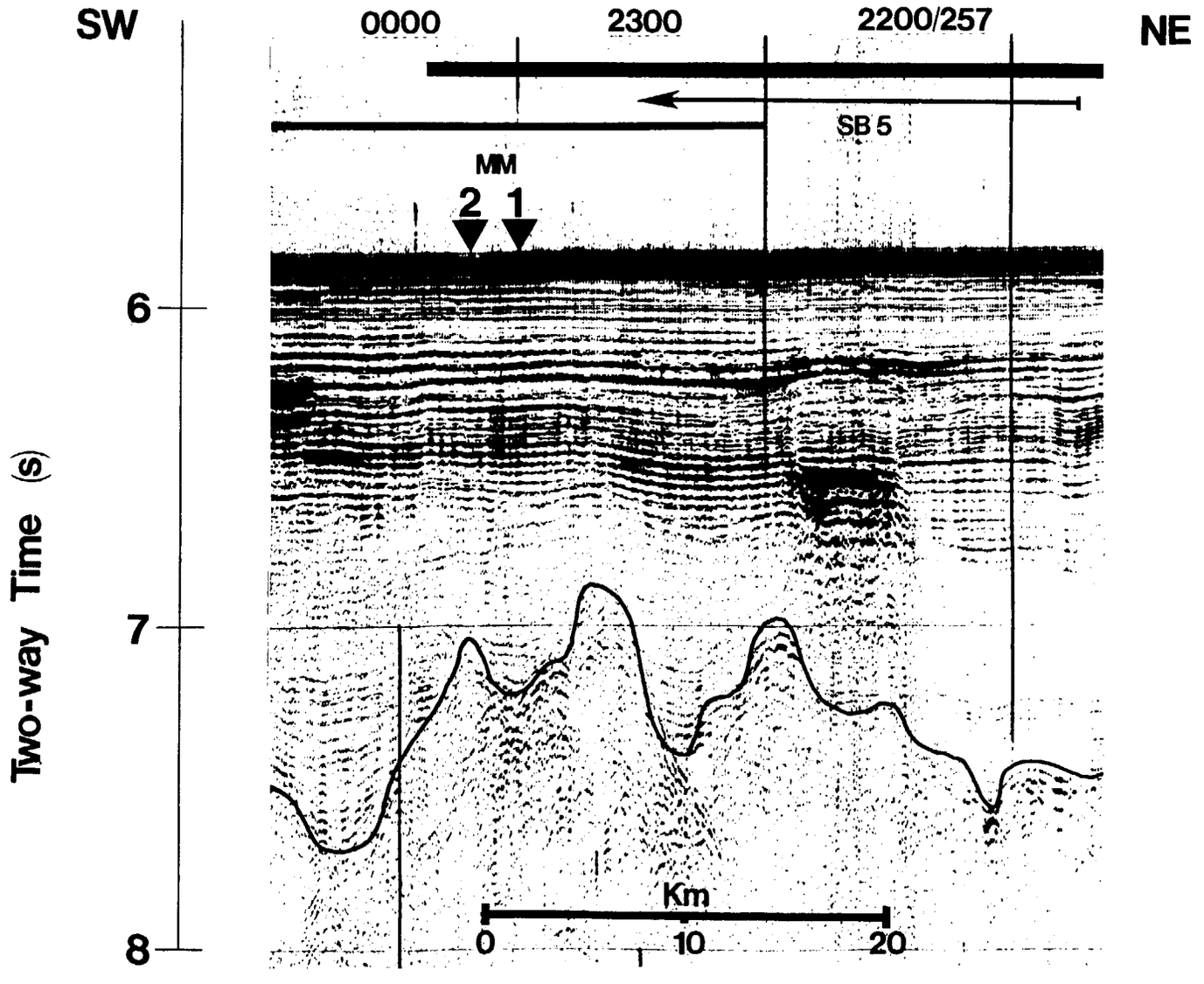

Figure 19: Seismic reflection profile in the vicinity of Point MM (see Figure 18 for location; Figure 5 for symbols).

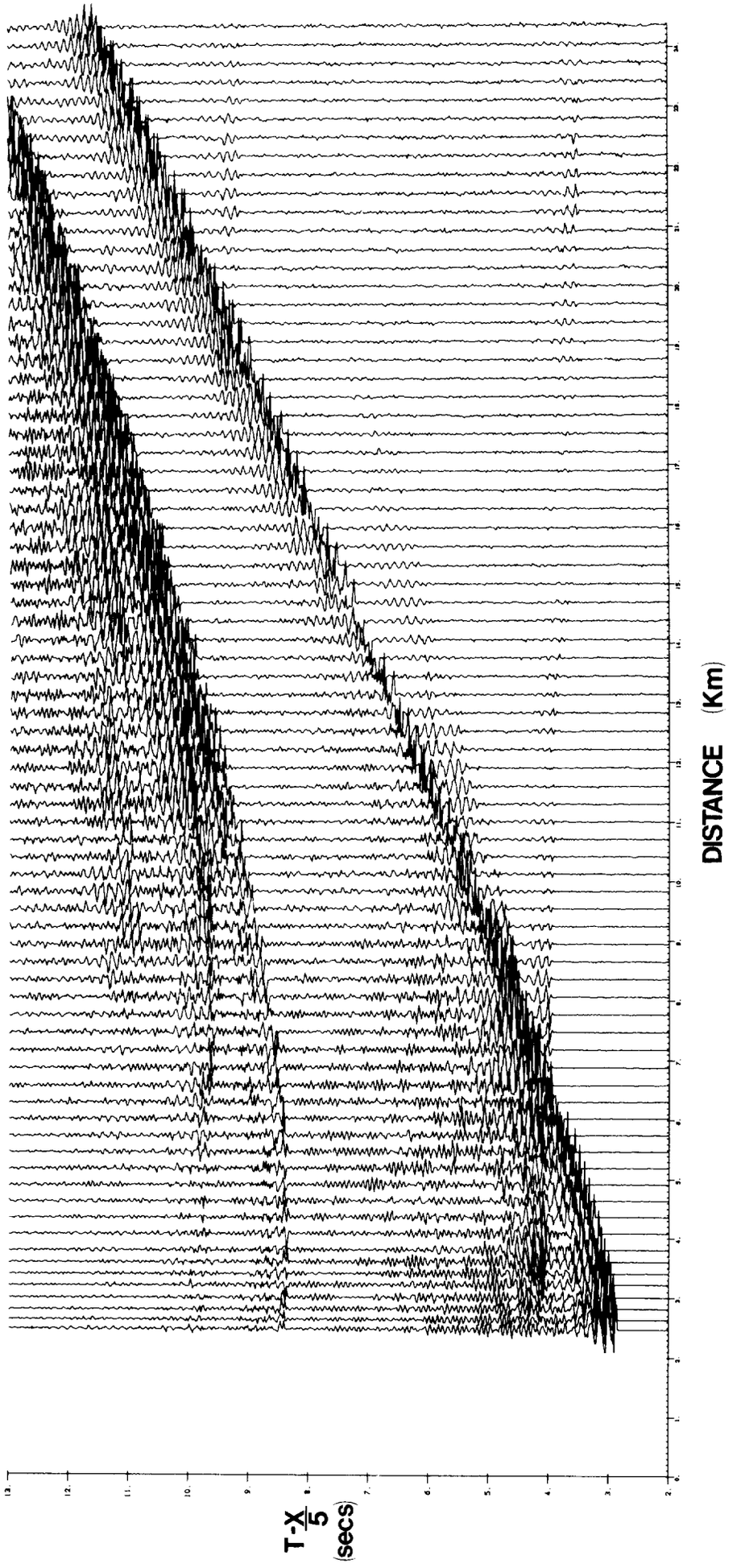

Figure 20: Unfiltered vertical geophone record-section recorded by DOBS1 at Point MM. Reduction velocity is 5 km s^{-1}; sampling rate 50 s^{-1}.

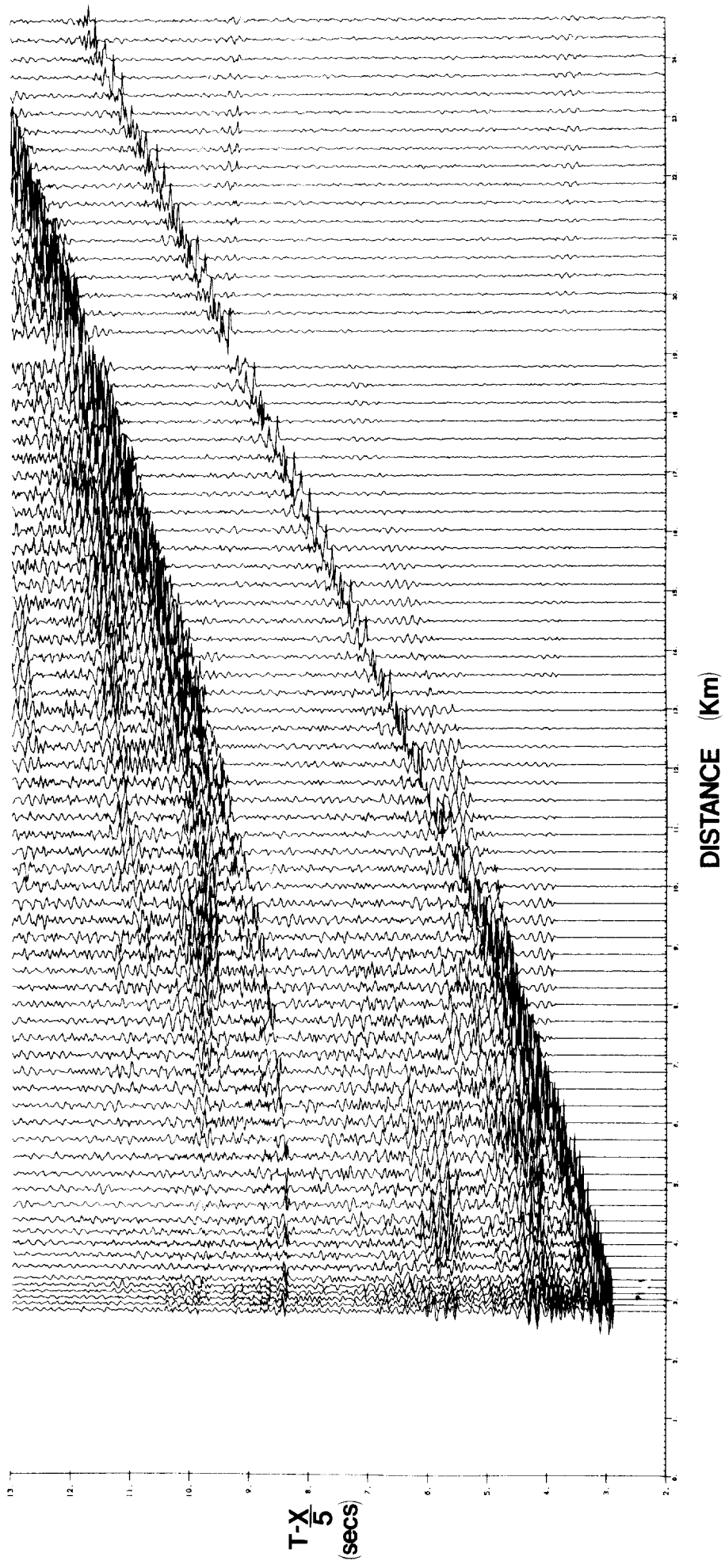

Figure 21: Unfiltered vertical geophone record-section recorded by DOBS2 at point MM. Reduction velocity is 5 km s^{-1}; sampling rate 50 s^{-1}.

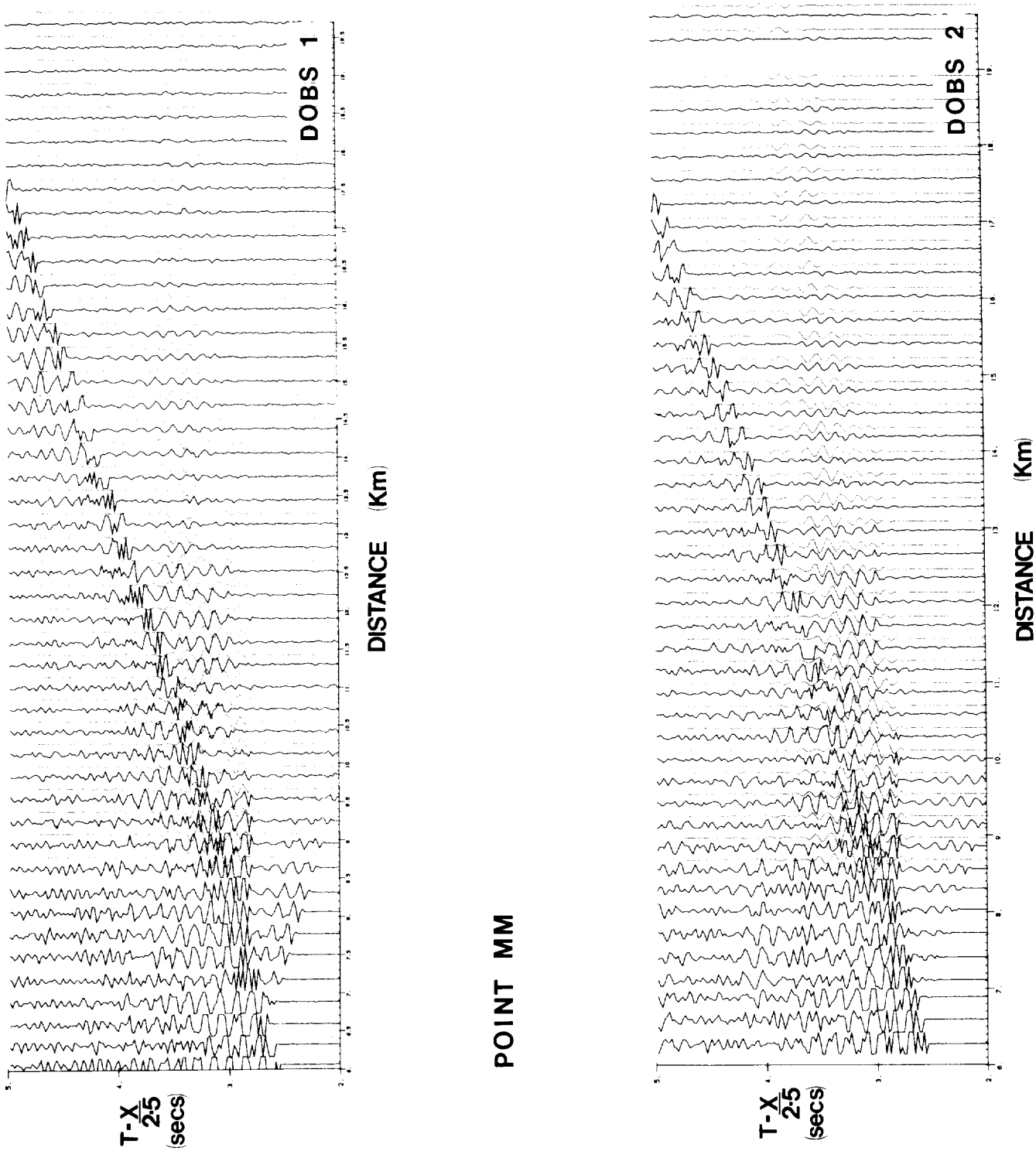

Figure 22: Unfiltered vertical geophone record-section recorded by DOBS 1 and 2 at Point MM. Reduction velocity 2.5 km s^{-1}. The synthetic seismograms are in red.

6.1.2. Lateral structural homogeneity

As at Point L the amplitudes and shapes of arrivals, observed at about the same range, are closely similar (Figure 22). On the record sections the phase differences of particular peaks or troughs vary in the range ±0.02 secs. This indicates a smaller travel-time variability of ±0.014 sec over individual sea and sediment paths than at Point L, possibly because the two DOBS were much closer together (1.1 km compared with 2.1 km at Point L).

Phase velocity across the two DOBS array was also studied, using the cross-correlation technique described in paragraph 5.1.3. (Figure 23). The scatter of points in Figure 23, within an envelope of about ±0.05 s km^{-1}, is a measure of the variation in travel-time caused by lateral inhomogeneity as well as by other factors such as the signal: noise and sampling rate. An error of 1 in the lag gives an error in ray parameter of 0.02 km^{-1}. These figures suggest a random variation along individual travel-time paths of ±0.033 secs. Again this estimate is somewhat greater than that derived from a comparison of observations at similar ranges. The reason may lie in the difficulty of cross-correlating signals from different ranges which have non-identical waveforms.

6.1.3. Modelling

The record sections at Point MM exhibit very similar features to those at Point L. It is necessary to find models which explain ,

(a) the 0.2 sec difference between each of three clear sets of sediment arrivals

(b) the decay in amplitude with range of each set so that the three sets of arrivals appear en echelon on the record-section.

The constraints on suitable models are,

(a) the 2.7 and 2.85 s time intercepts of the first set of 2.5 km s^{-1} arrivals which control the thickness and interval velocity of the layer between the sea-bed and the 2.5 km s^{-1} layer,

(b) the interval velocity structure derived from near vertical incidence reflections at Point MM.

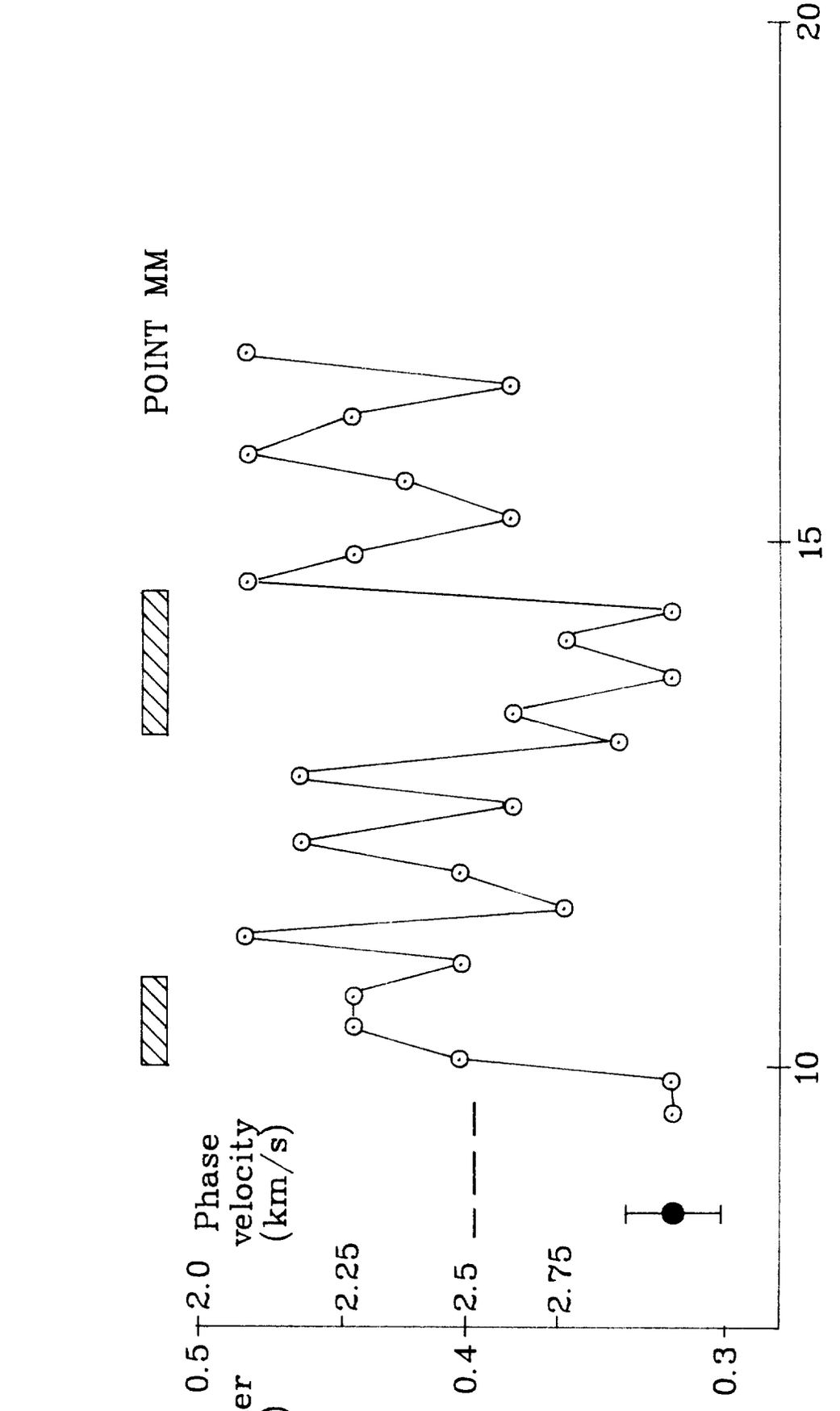

Figure 23: Phase velocity of sediment arrivals across the two-DOBS array at Point MM. The hachured rectangles mark the transition between different groups of sediment arrivals. The dashed line indicates the mean velocity of the primary arrivals which were too close to the water wave to be cross-correlated. The vertical bar indicates the uncertainty due to a lag error of 1.

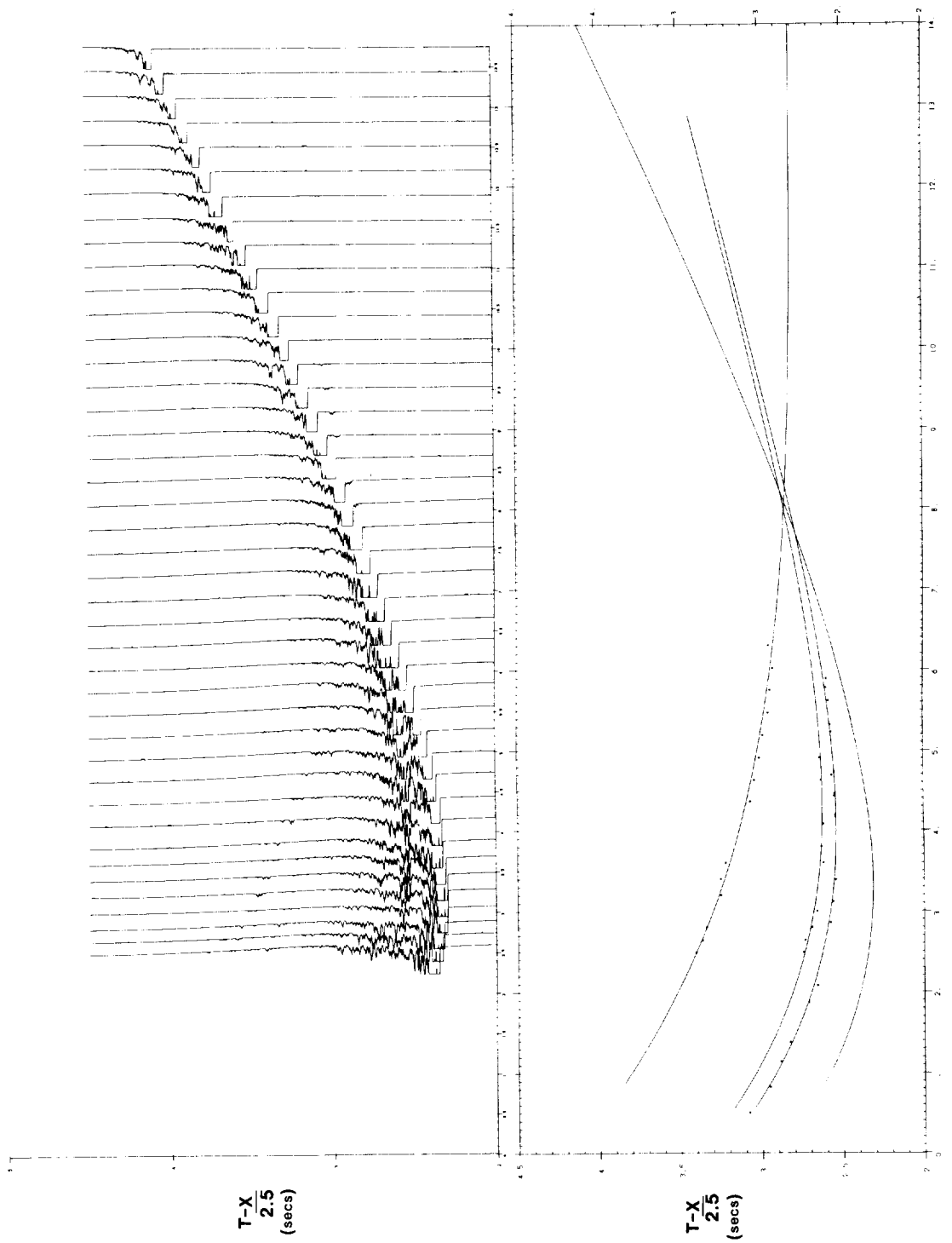

Figure 24: a. Example of near-vertical incidence reflections from the 300 ins^3 airgun recorded on the water-wave channel of DOBS 2 at Point MM.

b. Hodochrons fitted to picks from Figure 24a and from other record-sections. The lowest hodochron represents the direct water-wave.

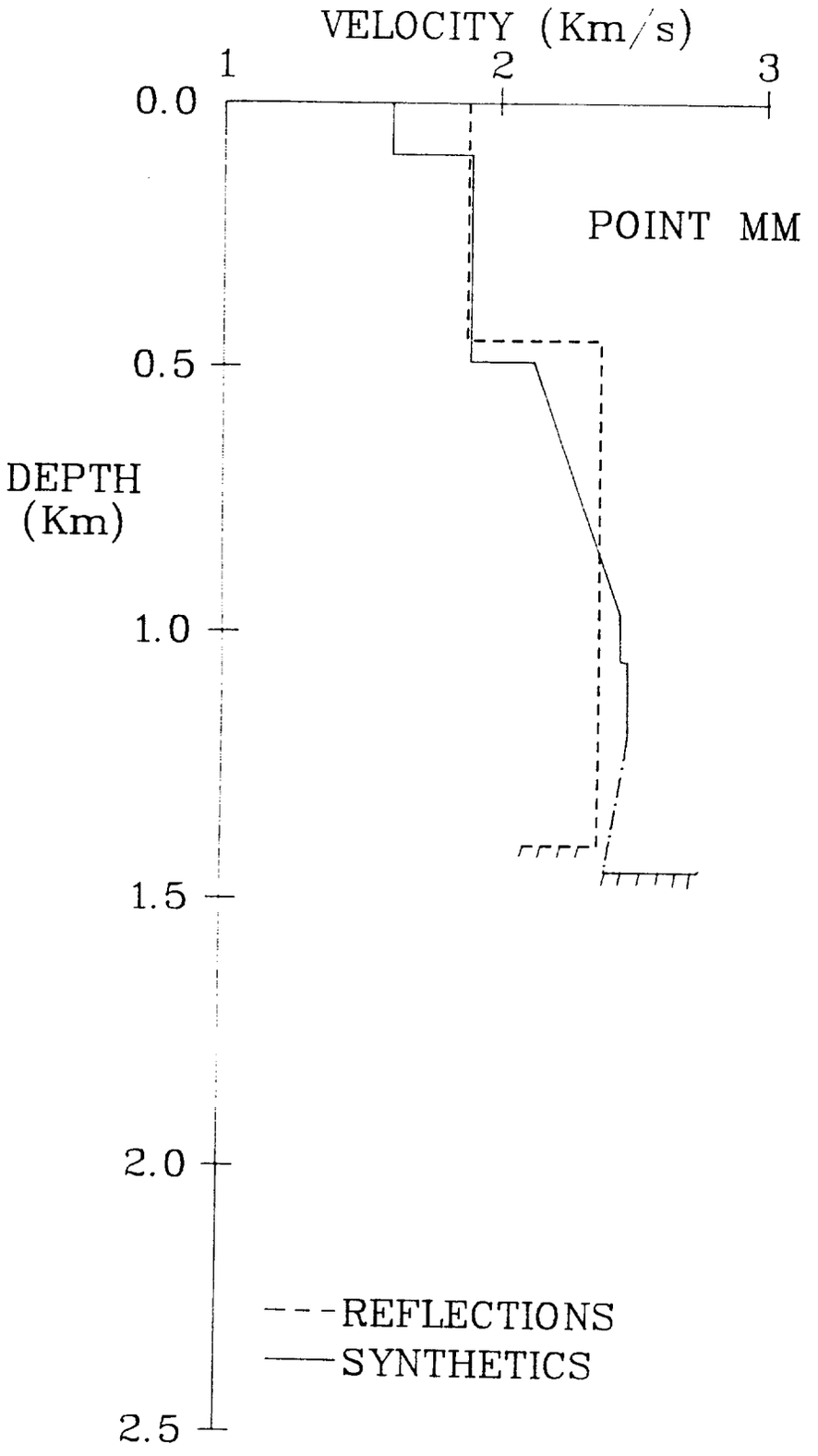

Figure 25: Velocity structures at Point MM. The dashed line represents the structure deduced from near-vertical incidence reflections, the continuous line is the structure which gave the optimum set of synthetic seismograms. See Table 5 for the detailed structure.

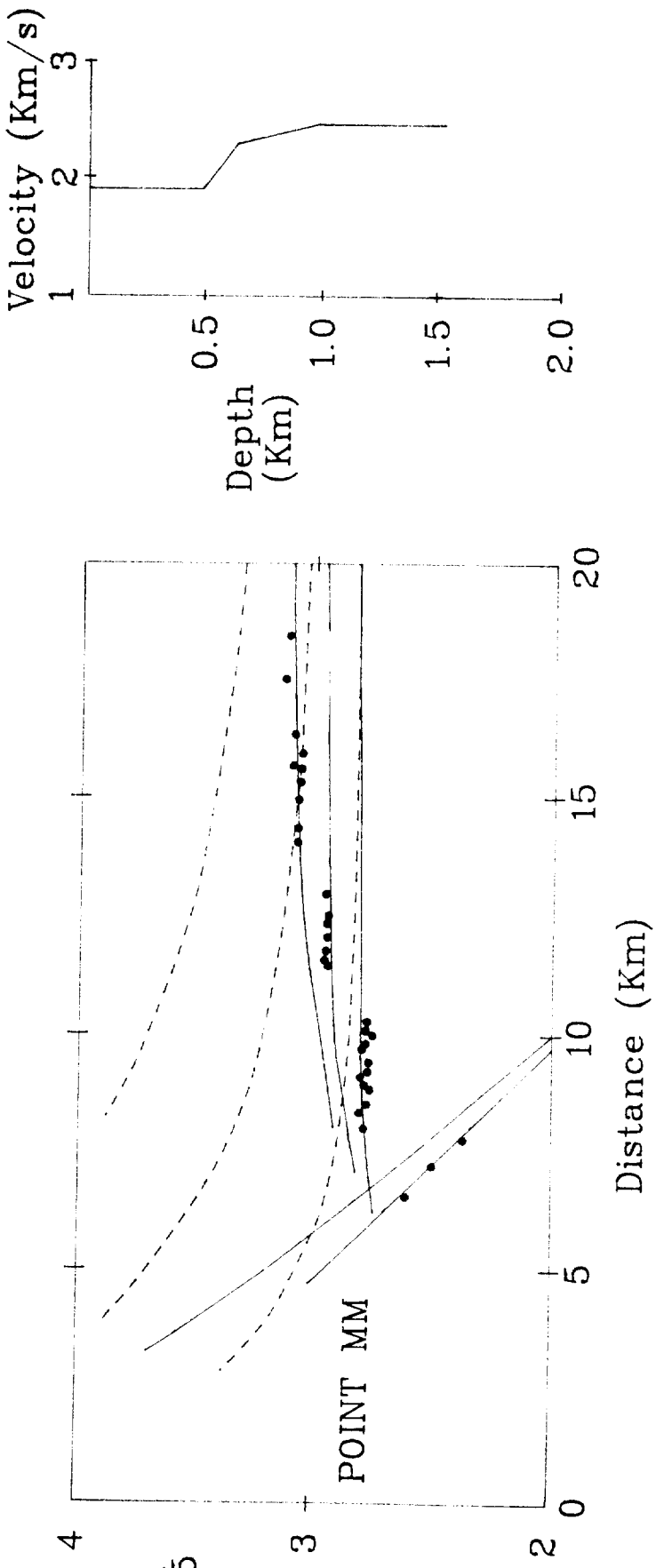

Figure 26: a. Calculated hodochrons which fit the observed arrivals in Figure 22. Three groups of sediment arrivals and a set of basement arrivals are shown. The concave upwards curves represent wide-angle basement reflections.

b. Velocity/depth structure used to calculate the travel-times in Figure 26a.

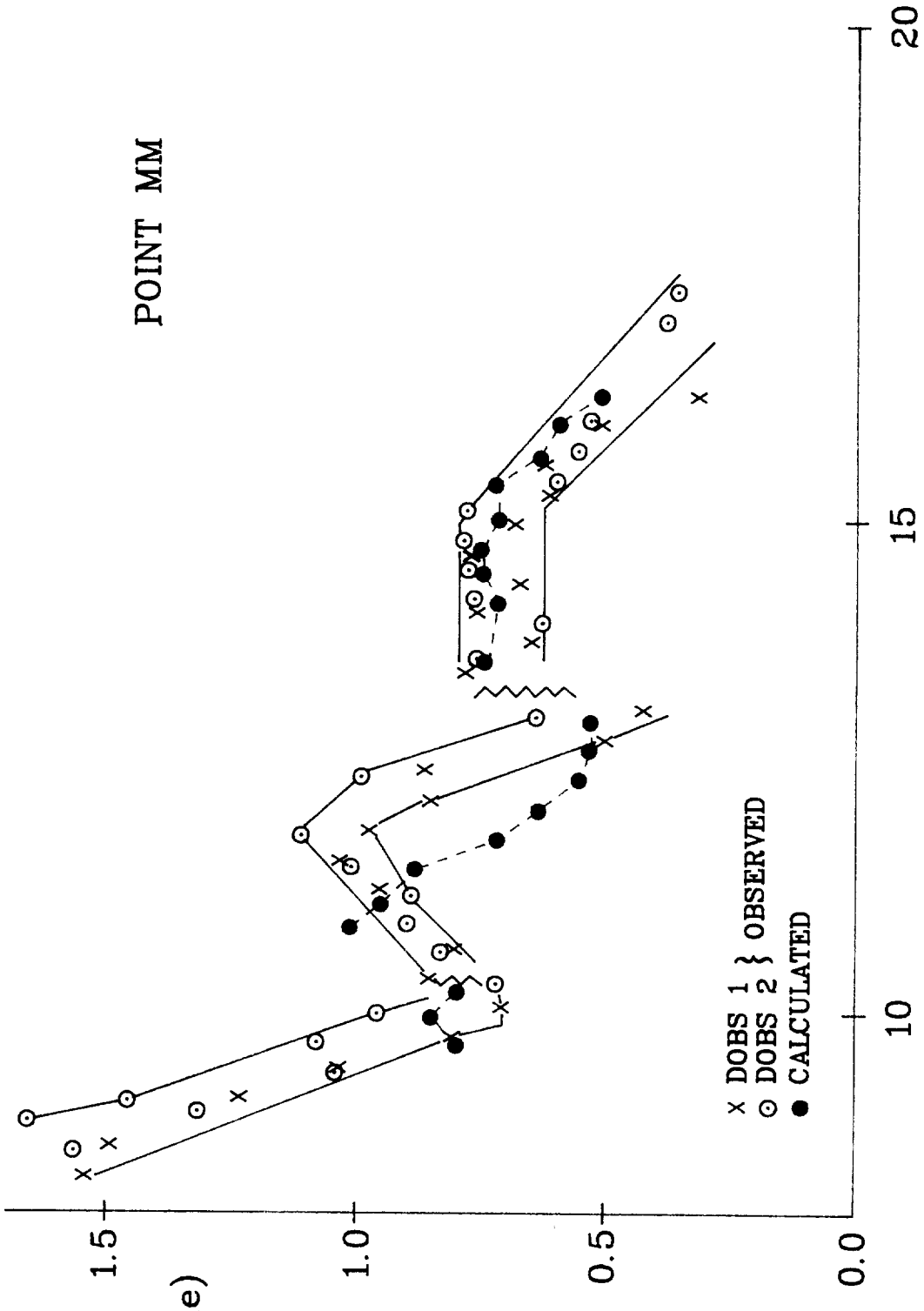

Figure 27: Amplitude/distance plot for sediment synthetic seismograms compared with the seismograms observed at Point MM. The continuous line marks the envelope of the observed points.

The same arguments for the groups of sediment arrivals being multiple refracted arrivals apply as at Point L. In particular an abrupt decrease in phase velocity is clearly seen in Figure 23 as one passes from the second to the third group of sediment arrivals.

Near-vertical incidence reflections from within the sediment layer and from the basement itself were seen on the record sections of both the 4 x 1000 ins^3 and 300 ins^3 airguns. The 300 ins^3 airgun enabled the shallowest reflections to be resolved but deeper reflections had to be picked on the record section of the more powerful airgun array. An example of the record-sections employed and the three hodochrons fitted to the picked points are shown in Figure 24 and the corresponding interval-velocity/depth structure in Figure 25. As at Point L the reflection of the multiples must occur within the sediments presumably at the interface between the 1.9 km s^{-1} and 2.4 km s^{-1} layers. A model of this sort which fits the observed travel-times is illustrated in Figure 26. Models of this type were developed, using the reflectivity program, in order to reproduce not only the three offset sets of sediment arrivals but also their amplitude change with distance. The amplitude-distance plot for each DOBS was remarkably similar (Figure 27). The best velocity structure, based on the synthetic seismograms, is represented in Figures 22, 25 and 27 and the model itself appears in Table 5. This structure exhibits essentially the same characteristics as the model for Point L.

7. RESULTS FROM AROUND POINT NN

The work in the vicinity of Point NN resulted in the collection of an airgun seismic reflection profile, a disposable sonobuoy profile and two airgun seismic refraction profiles, which were shot with the 4 x 1000 ins^3 array and the 300 ins^3 airgun with WSK and recorded by DOBS 1 and 2. The tracks are shown in Figure 28. The spatial relationship of the reflection and refraction profiles is indicated in Figure 29.

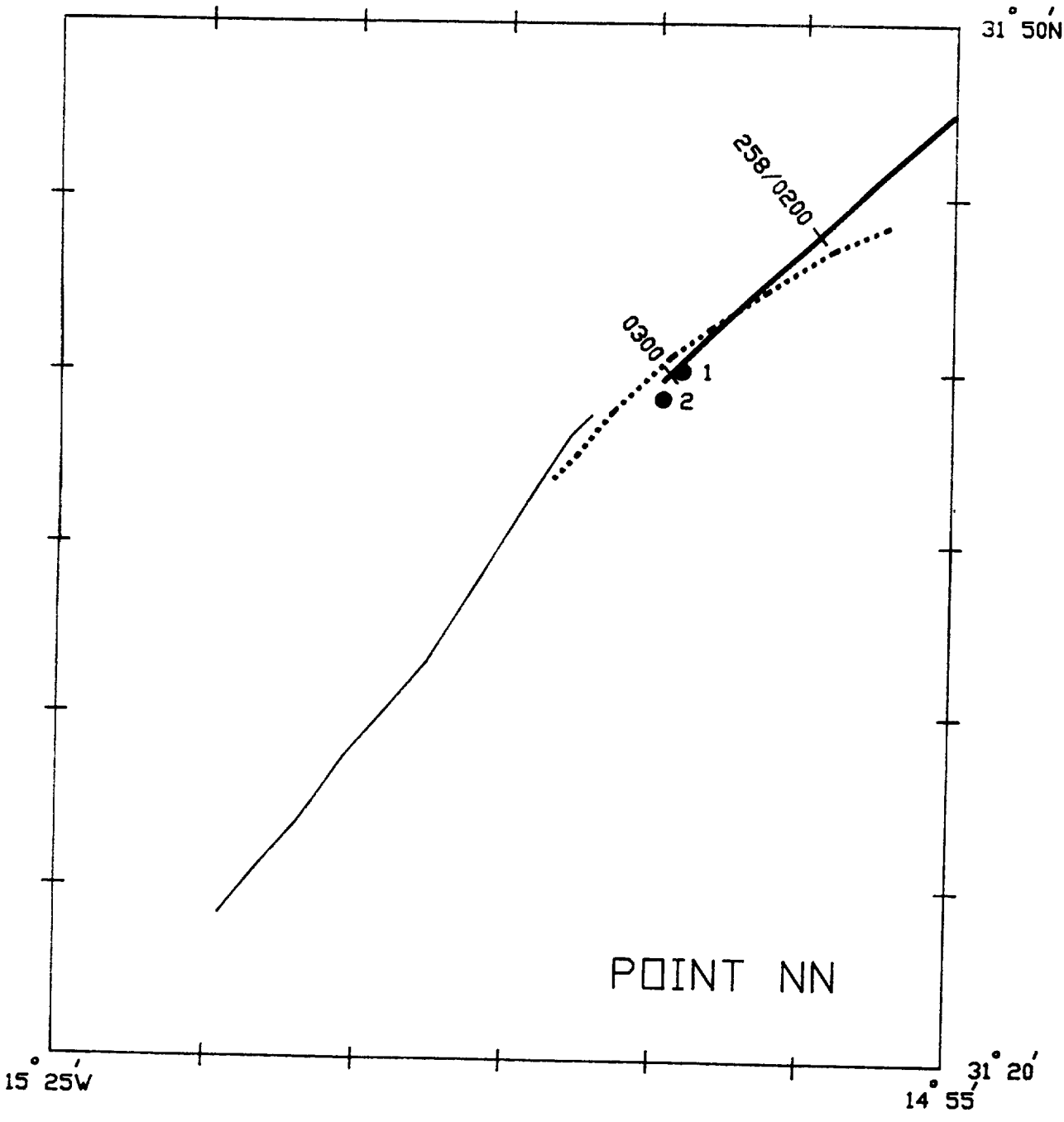

Figure 28: Track of seismic profiles near Point NN. Thick line = seismic reflection profile (Figure 29); thin line = wide-angle refraction profile; dotted line = near-vertical incidence reflection profile shot with 300 ins^3 airgun and waveshape kit; dots = DOBS.

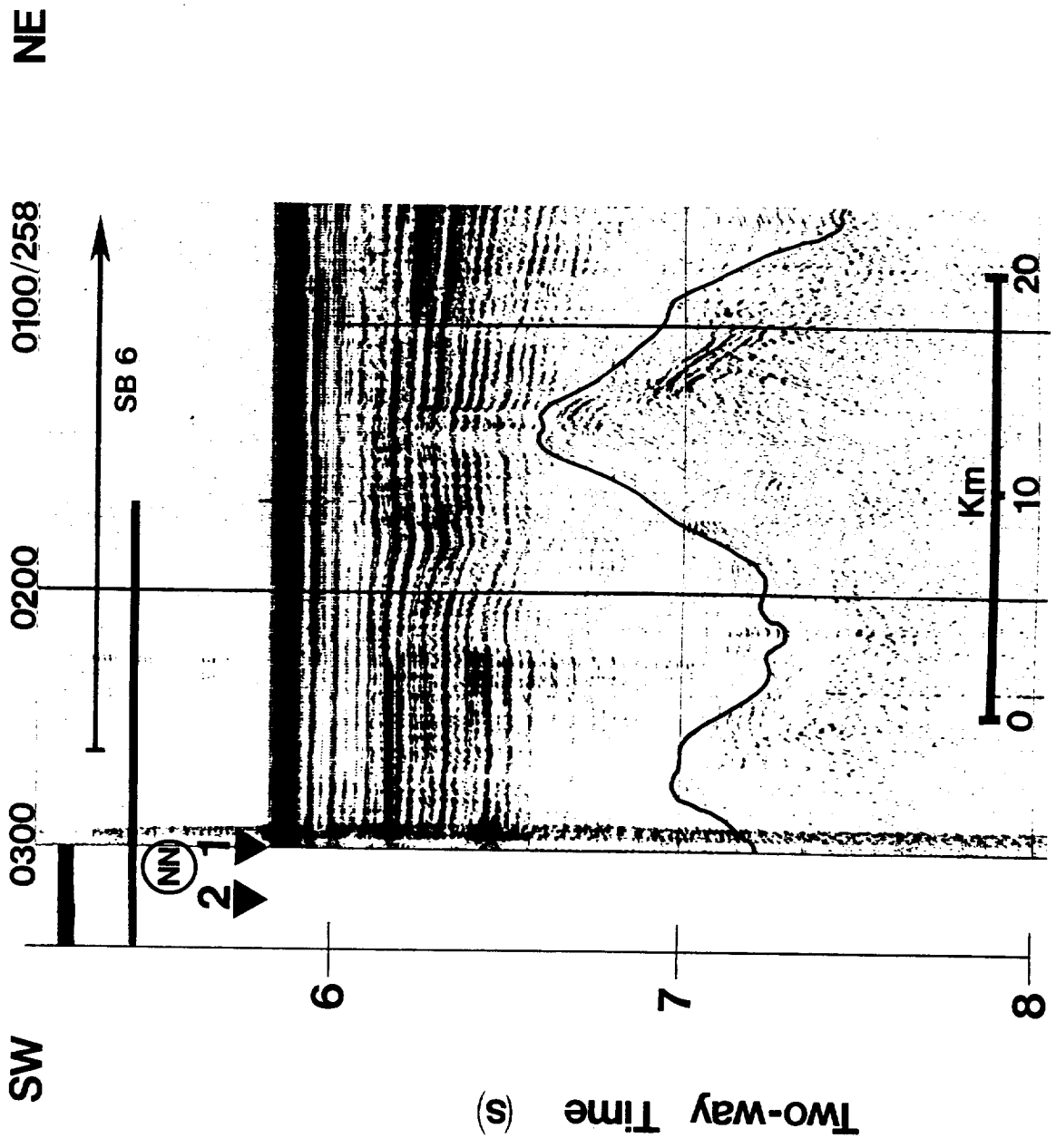

Figure 29: Seismic reflection profile in the vicinity of Point NN (see Figure 28 for locations, Figure 5 for symbols).

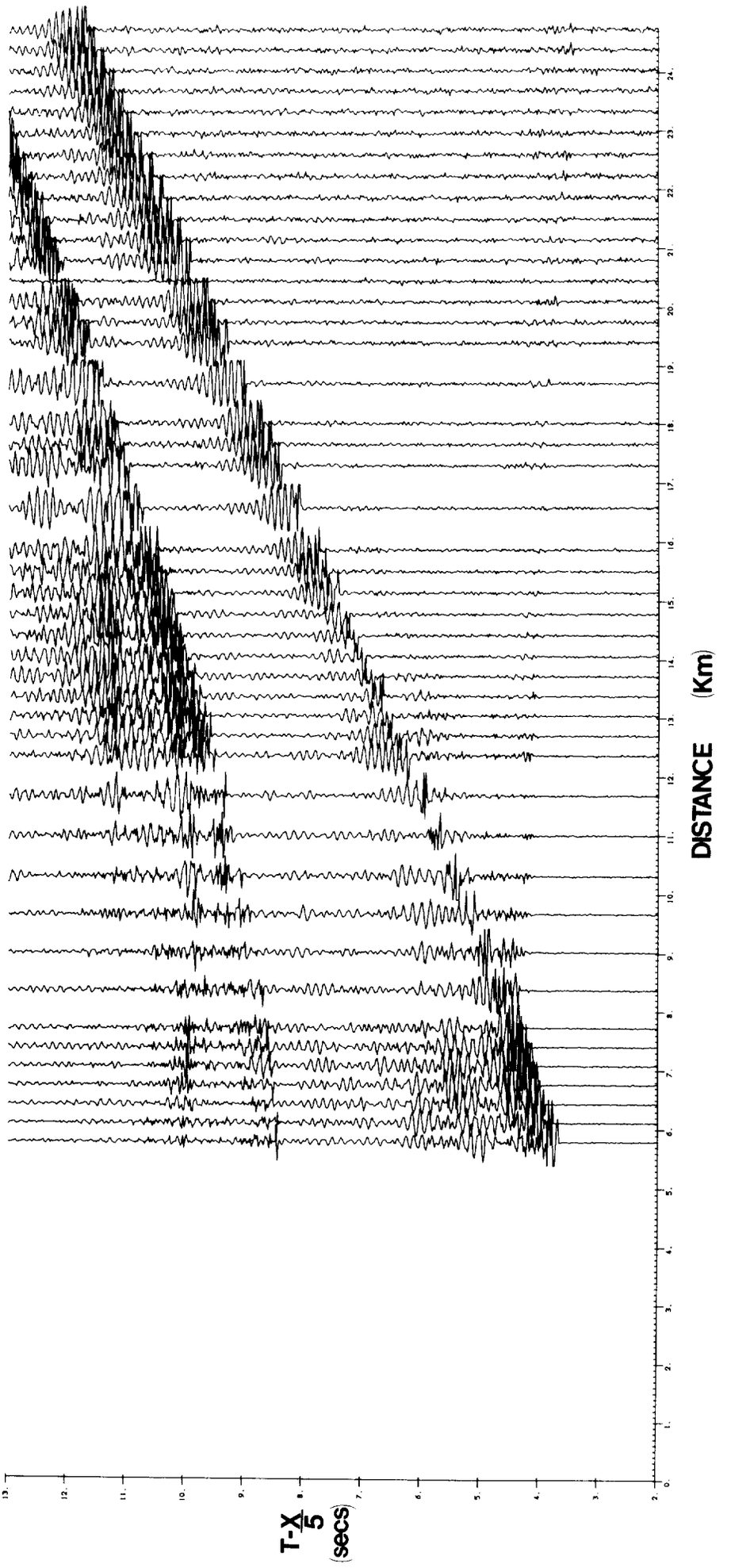

Figure 30: Unfiltered vertical geophone record-section recorded by DOBS1 at Point NN. Reduction velocity is 5 km s^{-1}; sampling rate 50 s^{-1}.

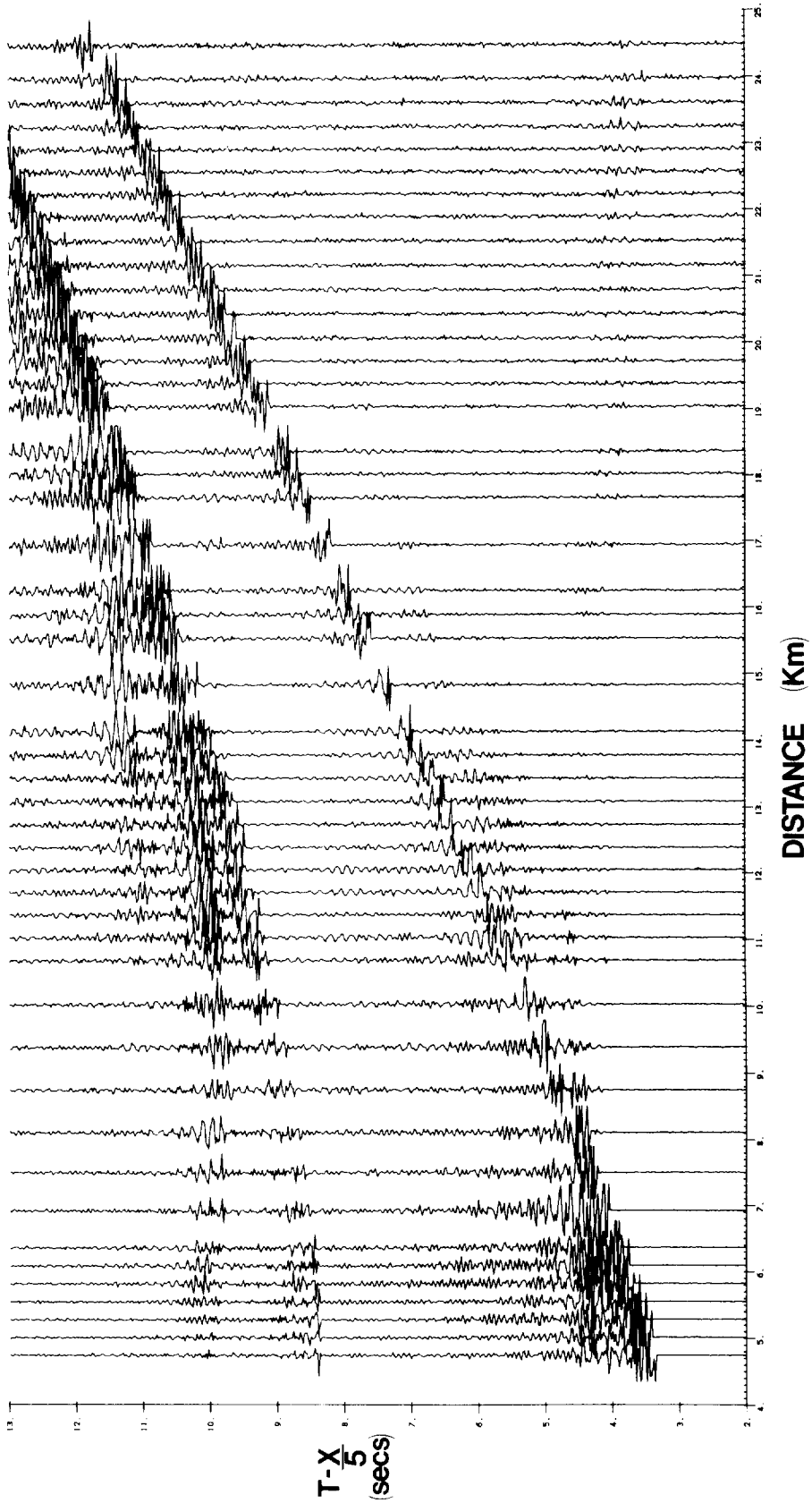

Figure 31: Unfiltered vertical geophone record-section recorded by DOBS2 at Point NN. Reduction velocity is 5 km s^{-1}; sampling rate 50 s^{-1}.

7.1 Seismic refraction profiles

The 4 x 1000 ins^3 airgun array was towed along a profile southwest of Point NN out to a range of about 37 km. The same firing rate, gun depth and air pressure were used as at Point L. A second shorter profile, shot with the 300 ins^3 gun with WSK, was obtained to investigate interval velocities between sediment and basement reflectors using the more 'spiky' waveform of this source. Thirdly a disposable sonobuoy was deployed on departure to the northeast from Point NN which recorded shots of the 300 ins^3 + WSK airgun firing every 13 seconds. This gave additional information about sediment interval velocities from near-vertical incidence and wide-angle reflections.

Ranges were calculated for all three profiles, as for the profile at Point L, using the soundspeed model in Table 6. This model is based on straight-line segments fitted by eye to point estimates of soundspeed calculated from temperature and salinity measurements down to 4300 m at Discovery II station 3645 (FUGLISTER 1960) and from temperature observations during XBT cast 7105A to 876 m depth on Day 258 in the vicinity of Point NN.

7.1.1. Observations

A vertical geophone record section from each DOBS is shown in Figures 30 and 31. The principal groundwaves are less easily distinguished than at the other stations because of their generally higher frequency content and because a number of traces are missing due to recording problems. However in general the same features are visible as elsewhere. Secondary phases from the sediment layer can be followed to almost 20 km and first arrivals from the igneous crust to at least 25 km. A variety of subcritical reflections and multiple arrivals can also be discerned. The parts of the record-sections containing the sediment arrivals are displayed at a larger scale in Figure 32. The record-sections are more complex than at Points L and MM because of the presence of relatively strong phases with velocities of at least 3.3 km s^{-1}. These are probably low-velocity basement arrivals multiply reflected within the sediments. Nevertheless three groups of sediment arrivals with apparent velocities close to 2.5 km s^{-1} can also be distinguished in the range 11-14 km, at about 14 km and beyond 14.8 km. Only a few onsets of these arrivals were picked with confidence

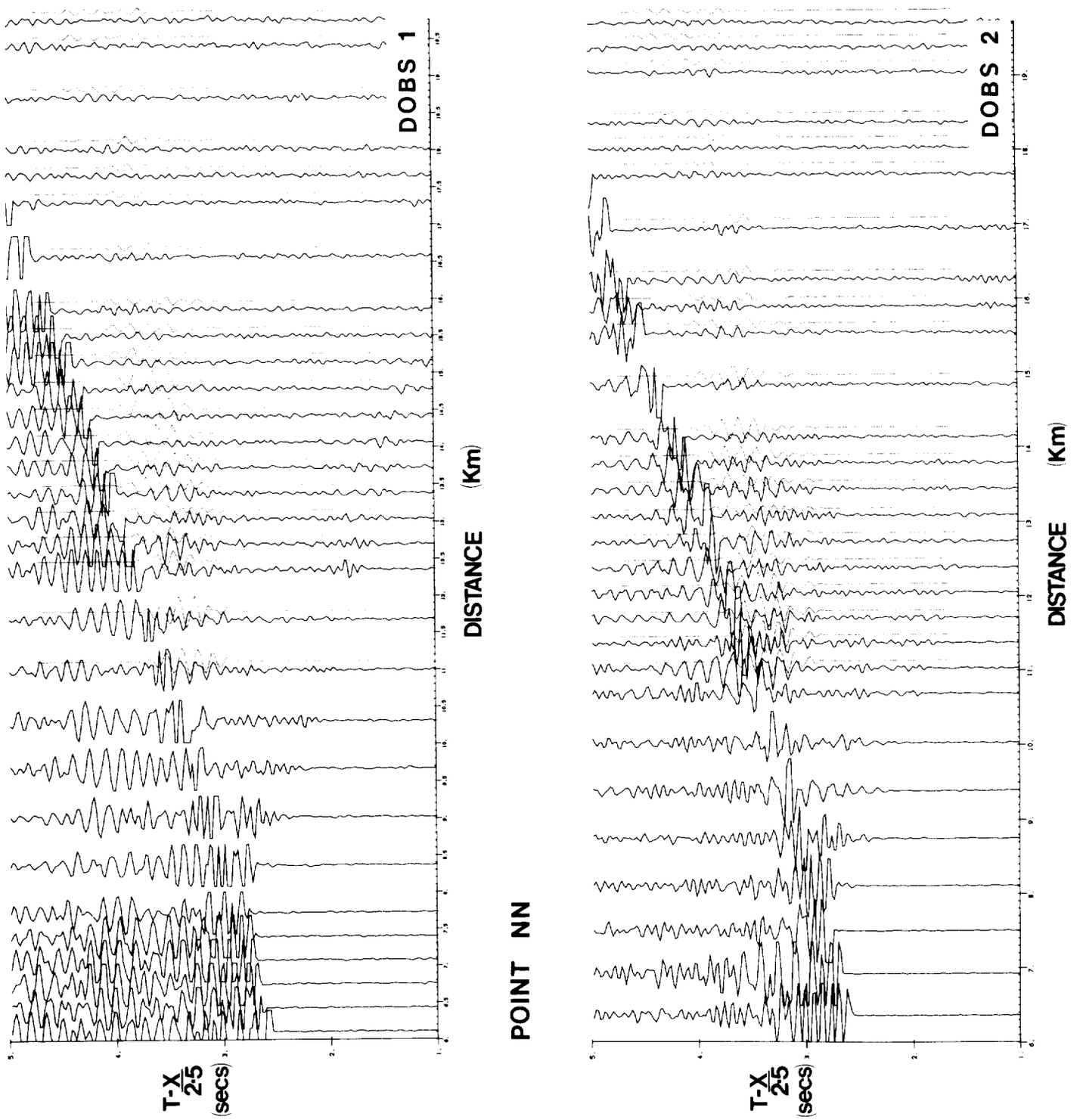

Figure 32: Vertical geophone record-sections recorded by DOBS 1 and 2 at Point NN. Filter low-pass 15 Hz; reduction velocity 2.5 km s^{-1}. The synthetic seismograms are in red.

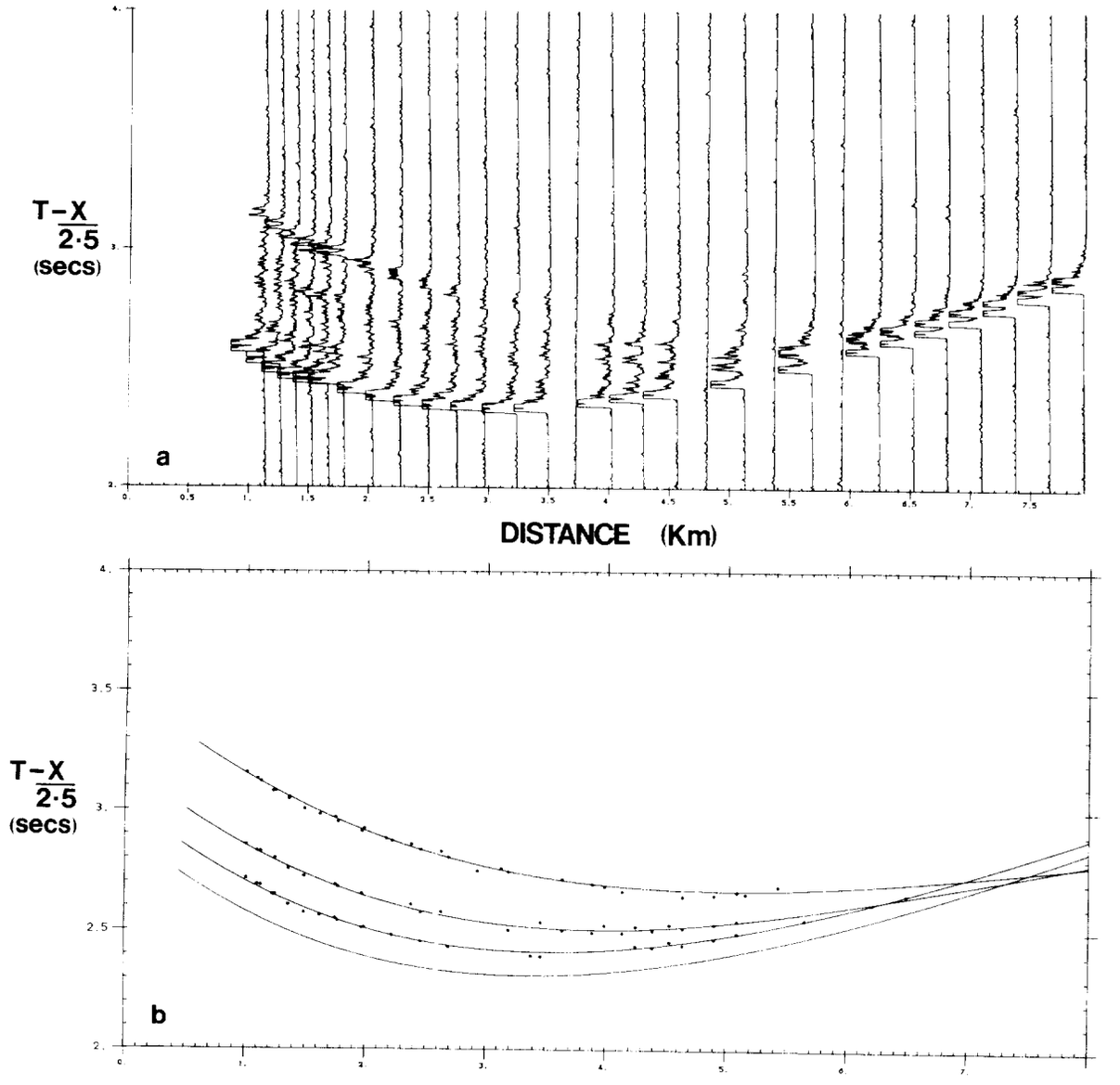

Figure 33: a. Example of near-vertical incidence reflections from the 300 ins^3 airgun recorded on the water-wave channel of DOBS 1 at Point NN. b. Hodochrons fitted to picks from Figure 33a and from other record-sections. The lowest hodochron represents the direct water-wave.

because of the interference of the preceding multiples. Each group is delayed by about 0.25 s with respect to the previous group. The above features are more clearly seen on the DOBS 2 record-section but the other record-section is not inconsistent with the first if the two are overlain.

7.1.2. Lateral structural homogeneity

The amplitudes and shapes of the sediment arrivals, observed at about the same range, are closely similar (Figure 32). On the record-sections the phase differences of individual peaks or troughs are almost entirely in the range ±0.02 secs. The implied travel-time variability of ±0.014 secs for individual shot-to-DOBS paths is similar to the other two sites and implies even greater structural homogeneity since the DOBSs lay 2.0 km apart.

In view of the poorer signal: noise of the sediment arrivals and the missing traces measurement of phase velocities by cross-correlation was not made.

7.1.3. Modelling

The record sections at Point NN exhibit similar features to those at Point L. It is necessary to find models which explain,

(a) the 0.25 sec difference between each of three sets of sediment arrivals,

(b) the decay is amplitude with range of each set so that the three sets of arrivals apppear en echelon.

The constraints on suitable models are,

(a) the 3.05 s time intercept of the first set of 2.5 km s^{-1} arrivals which controls the thickness and interval velocity of the layer between the sea-bed and the 2.5 km s^{-1} layer.

(b) the interval-velocity structure derived from near vertical incidence reflections at Point NN.

Following the observations and discussion of Point L and Point MM data the second and third sets of sediment arrivals are assumed to be multiples of the first reflected within the sediments.

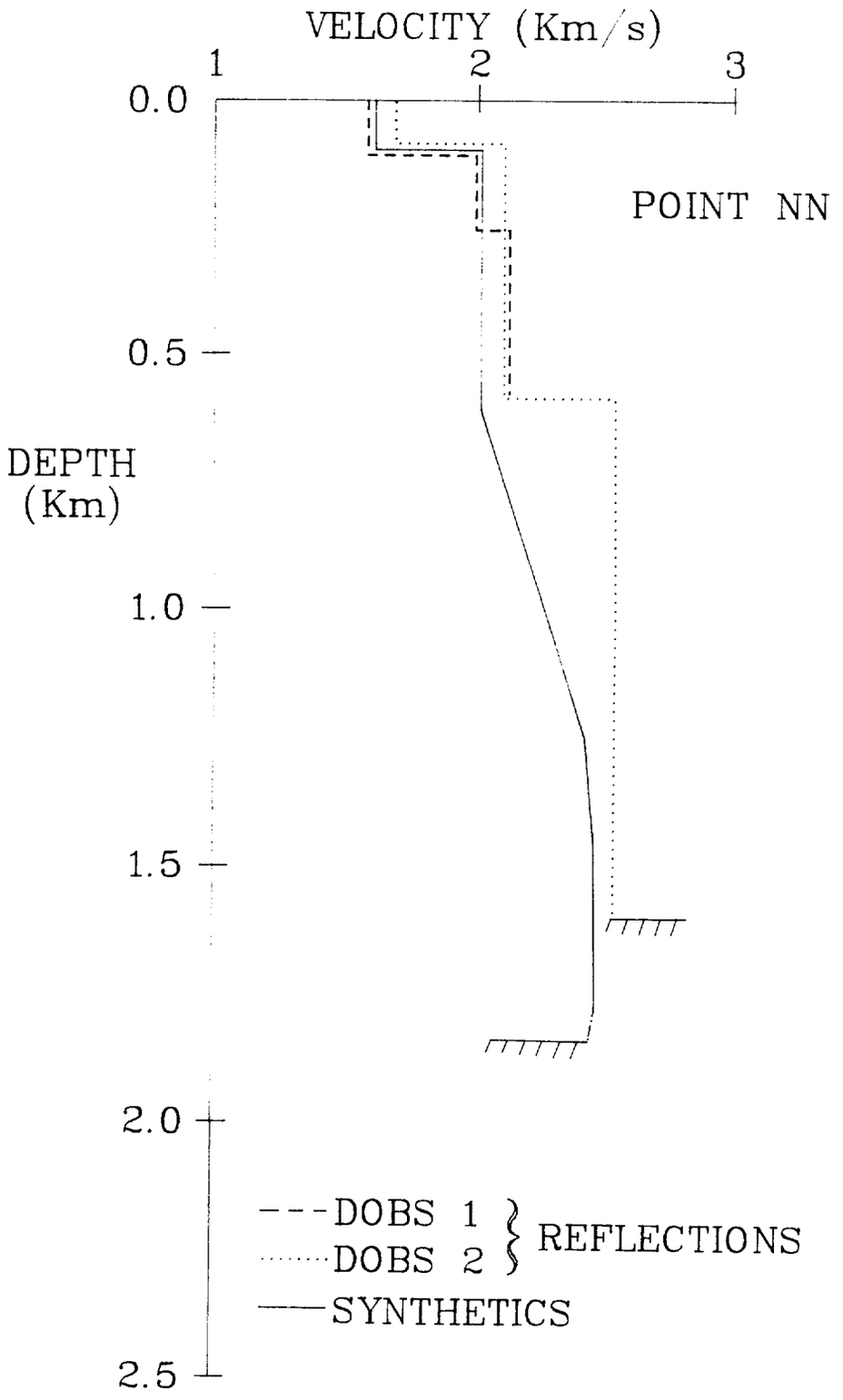

Figure 34: Velocity structures at Point NN. The dashed and dotted lines represent the structure deduced from near-vertical incidence reflections, the continuous line is the structure which gave the optimum set of synthetic seismograms. See Table 7 for the detailed structure.

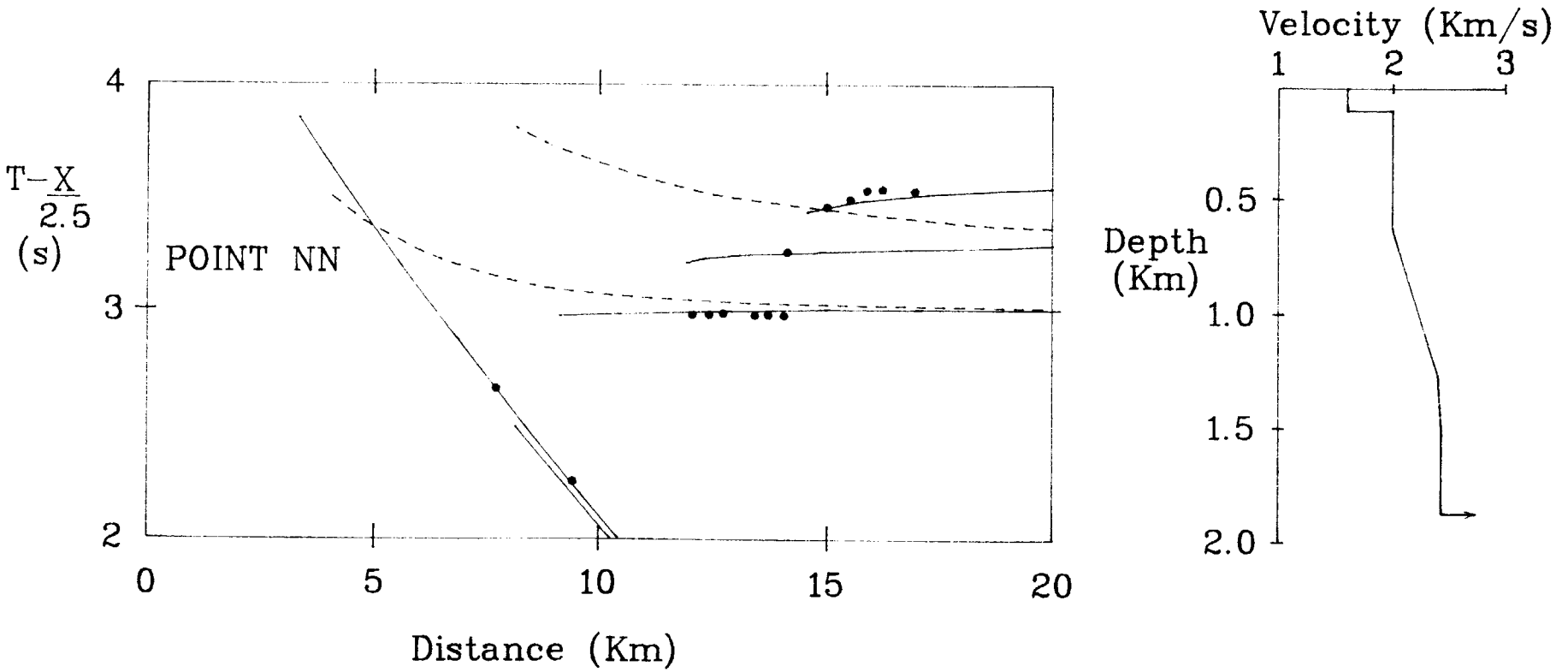

Figure 35: a. Calculated hodochrons which fit the observed arrivals in Figure 32. Three groups of sediment arrivals and a set of basement arrivals are shown. The concave-upwards curves represent wide-angle basement reflections.

b. The velocity/depth structure which was used to calculate the hodochrons in Figure 35a.

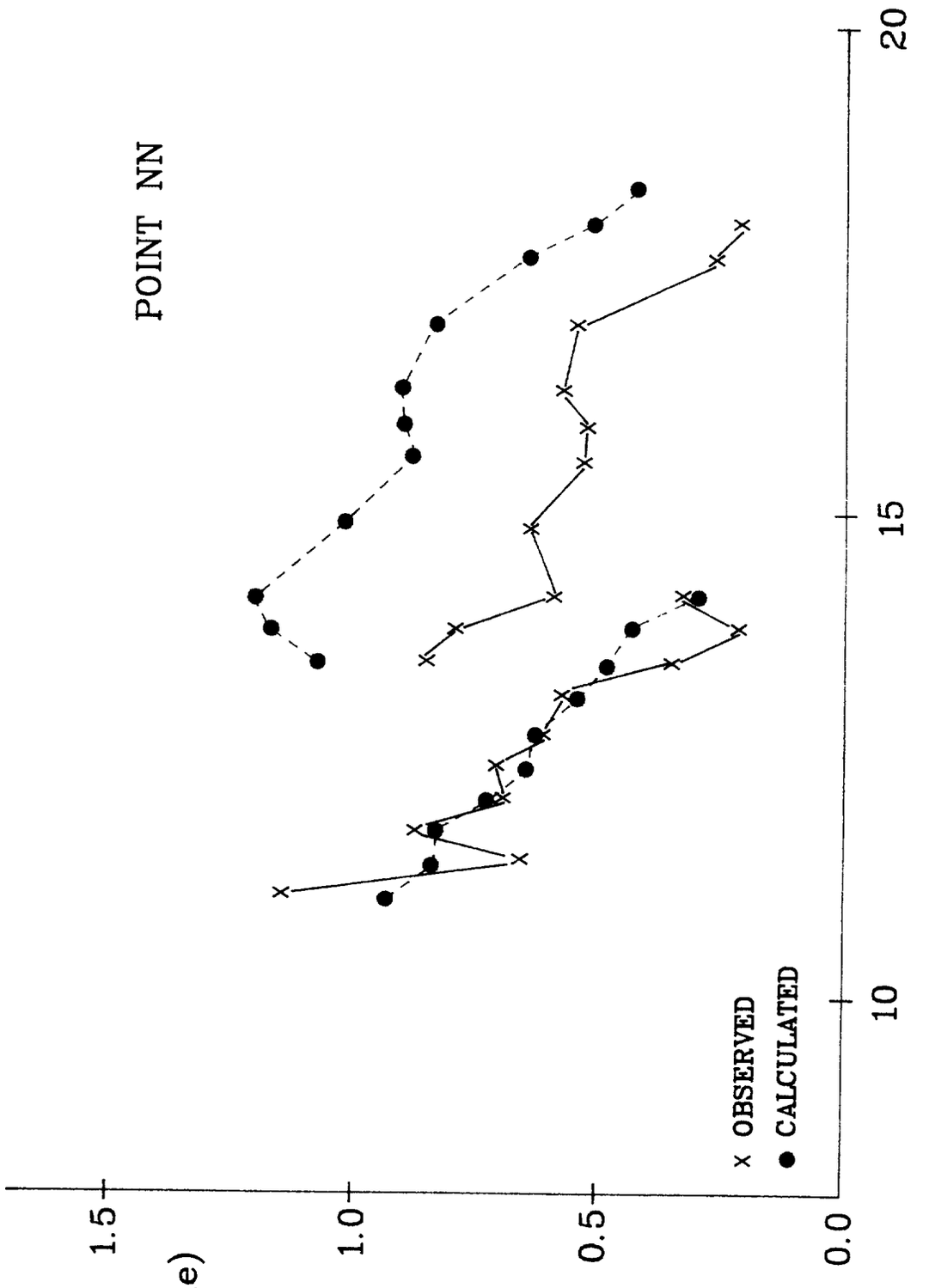

Figure 36: Amplitude/distance plot for sediment synthetic seismograms compared with the seismograms observed at Point NN.

Near-vertical incidence reflections from within the sediment layer and from the basement itself were clearly seen on both DOBS 1 and DOBS 2 record-sections of both the 4 x 1000 ins^3 and 300 ins^3 airguns. By combining picks of arrivals from both airguns for each DOBS two independent, but very similar, interval-velocity/depth structures were obtained (Figure 34). An example of the near-vertical-incidence reflections and the reflection curves fitted to picked arrival times is given in Figure 33.

The time separation between the difference groups of sediment arrivals is even greater at this station than elsewhere. Nevertheless reflection of

multiples within the sediments is still able to model the observed travel-times as illustrated in Figure 35. Models of this type were developed, using the reflectivity program, in order to reproduce not only the offset times of sedimentary arrivals but also their amplitude change with distance (Figure 36). The corresponding velocity structure based on the synthetic seismograms is represented in Figures 32, 34 and 36 and the model itself in Table 7. The structure in Figure 34 has similar characteristics to the structures at Points L and MM. A significant difference however is the absence of a P-wave velocity step at the mid-sediment reflector; this is discussed below.

8. SONOBUOY PROFILES

Three disposable sonobuoys successfully recorded 300 ins^3 airgun shots fired every 13 s along the ARE profile. Their locations are indicated in Figure 5. Although adequate radio signals were received upto 25 km range the most useful data were the near-vertical incidence reflections from within the sediments and from the basement which were seen in the first 7 kms.

Airgun-to-sonobuoy ranges were calculated from the direct water-wave travel-time (out to about 0.5 km) and at greater ranges from the travel-time of the sea-bed reflection.

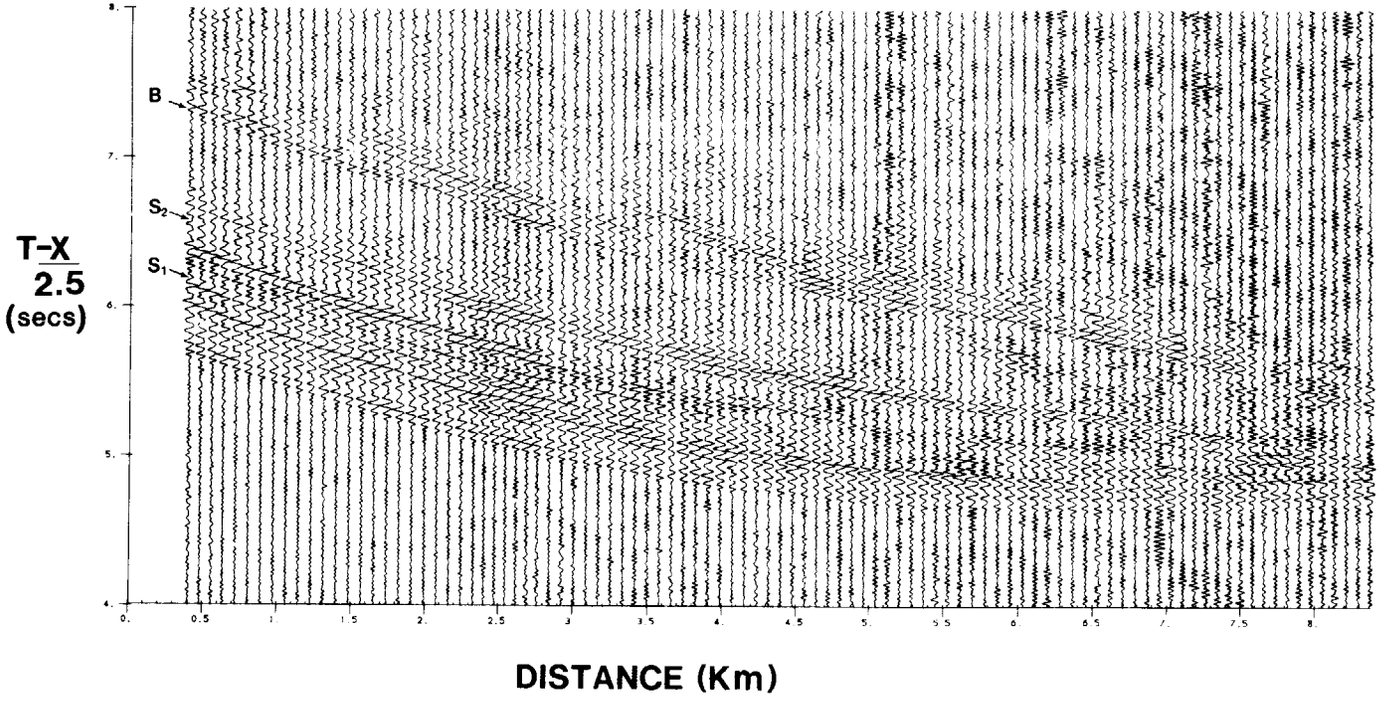

Figure 37: An example of a sonobuoy record-section; reduction velocity 2.5 km s^{-1}. The data were recorded at SB5.

The same travel-time fitting technique was used as for the near-vertical incidence reflections detected by the DOBSs (Section 4.3). An example of a sonobuoy record section is given in Figure 37. The velocity structure derived from each sonobuoy is given in Table 8.

9. DISCUSSION

9.1 Velocity structure from near-vertical-incidence reflections

Near-vertical-incidence reflections were observed by DOBSs and sonobuoys at ranges upto 8 km. The trace density and data quality were variable but structures were obtained at sonobuoys 4 and 5 and at Points MM and NN (from DOBS and/or sonobuoys).

Although the fine-scale of the layering within the sediments cannot be resolved all the above structures are consistent in indicating a relatively low-velocity upper sedimentary layer (1.6 to 2.0 km s^{-1}) overlying a higher velocity (2.1 to 2.6 km s^{-1}) layer (Figure 38). (The higher velocity "upper" layer at sonobuoy 4 is assumed to represent a mixture of upper and lower layer material. The true boundary may not have been resolved due to being too close to the sea-bed.) The depth to the lower layer increases systematically southwestwards from 0.48 to 0.78 km.

9.2 Velocity structure from synthetic seismograms

Although consistent with the observations in Section 9.1 the structures based on synthetic seismograms show more detail in the lower sediments (Figure 38). The mid-sediment boundary deepens southwestwards from 0.3 km at Point L to 0.61 km at Point NN. The velocity increase at the boundary seems to be inversely related to the size of the underlying linear gradient which leads downwards to velocities of 2.41 to 2.48 km s^{-1}. An underlying, almost constant velocity, layer (2.41 to 2.51 km s^{-1}), which is 0.23 to 0.53 km thick, overlies a negative gradient zone.

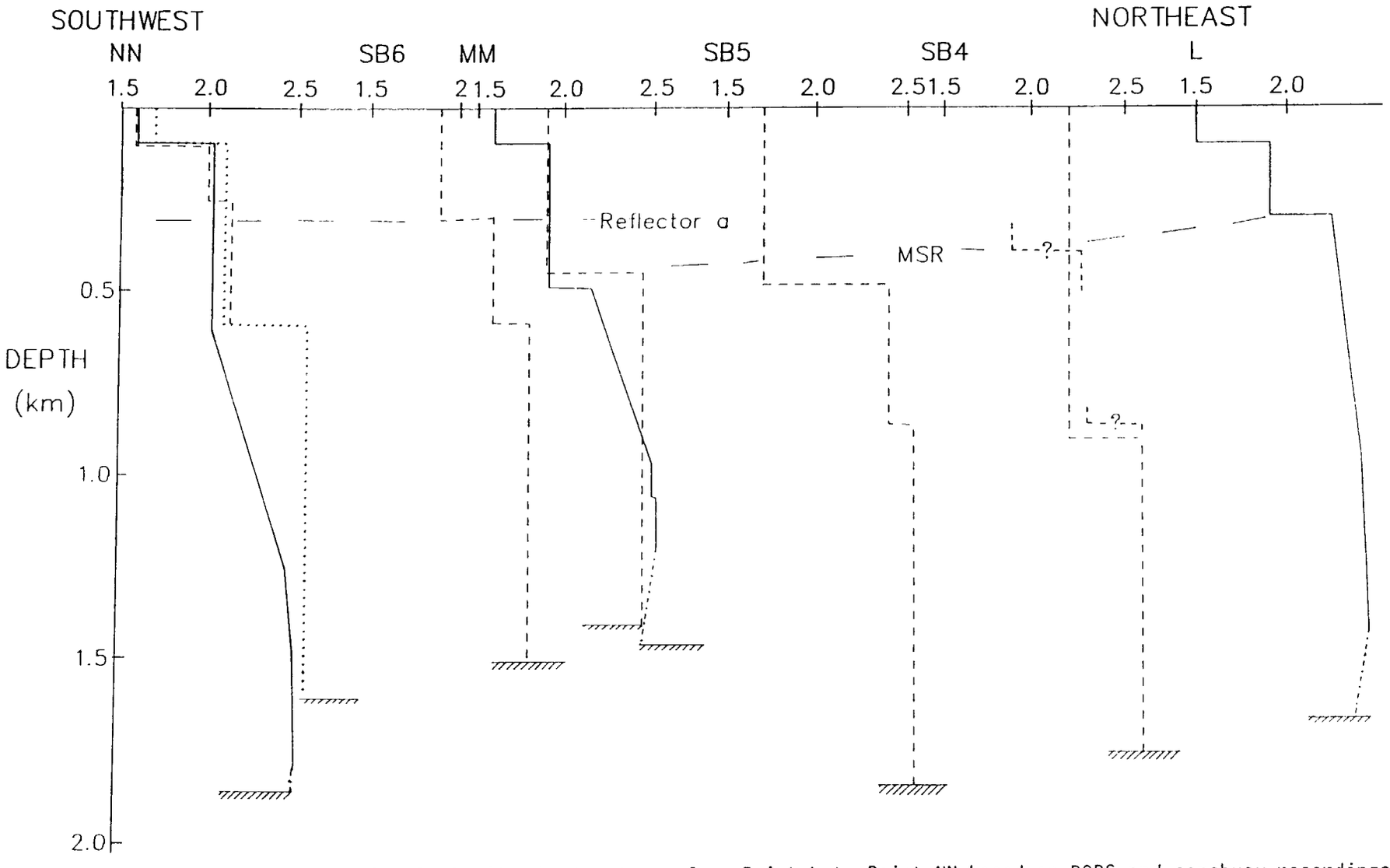

Figure 38: Summary of all velocity/depth structures from Point L to Point NN based on DOBS and sonobuoy recordings. The continuous lines denote models based on synthetic seismogram calculations. The negative gradient at the base of these models is uncertain (see text). The discontinuous lines are models from near-vertical incidence reflections. At SB4 a reflection from the mid-sediment reflector was not detected. One possible interpretation of the SB4 model, which includes this reflector, is indicated. Hachured lines = top of volcanic basement.

A standard structure, based on the near-vertical incidence reflection data, was used for the upper sediments. This structure assumed 100 metres of 1.6 km s^{-1} (indicated by reflections at Point NN). A velocity of 1.9 or 2.0 km s^{-1} was assumed for the remaining upper sediments depending on relevant reflection models. Unfortunately no sediment arrivals with upper-layer apparent velocities were observed on the record-sections. It is simple to show by travel-time computations that this negative observation strongly suggests that in fact the upper sediments may contain a positive velocity gradient rather than the constant velocity assumed in calculating synthetic seismograms. With the information available it is only possible to put a lower limit on the gradient however from the lack of ca 1.9 km s^{-1} phases in that part of the record-section where there are no other significant signals. For example, at Point MM the lack of 1.9 km s^{-1} arrivals between the water-wave and the 2.5 km s^{-1} arrivals at ranges greater than 13 km indicates a gradient of at least 0.2 s^{-1} in the 1.9 km s^{-1} layer. A further more speculative possibility is that 1.9 km s^{-1} arrivals are excluded due to a negative gradient in the lower part of the upper sediments. This deficiency illustrates the window of inaccessibility which exists for the few hundred metres below the sea-bed which can only be investigated directly by using bottom sources.

In addition to the uncertainty about the upper sediment structure several other features deserve comment. It should be emphasised that the mid-sediment reflector, which gives rise to the multiple sediment arrivals, results primarily from the contrast in shear-wave velocity across it (in the models the upper velocity is 0.1 km s^{-1}, the lower velocity 0.58 times the P-wave velocity). Even in the absence of a compressional-wave velocity contrast, as at Point NN, the sediment multiples experience a reflection coefficient of at least 0.5 if the upper-sediment S-wave velocity is 0.1 km s^{-1} (or at least 0.4 if Vs is 0.5 km s^{-1}).

Several synthetic models do not adequately reproduce the relative amplitude contrast betweeen the primary and multiple sediment arrivals. It is likely that further modelling, with a weaker S-wave velocity contrast across the reflecting horizon, would resolve this problem.

The negative gradient zone in the lower sediments was introduced to ensure the correct fall-off in amplitude with distance of the primary sediment arrivals, in models which, to reduce computation time, excluded the underlying volcanic basement. It is possible that such gradients are artifacts. In reality reflection from the basement may curtail the lateral extent of the primary sediment arrivals on the record-sections.

The synthetic seismogram models assume quality factors $Q\alpha$ of 500 and $Q\beta$ of 250. In spite of using values as low as $Q\alpha$ = 100, $Q\beta$ = 50 no significant amplitude difference was detected.

9.3 **Accuracy of the velocity models**

It is not straight-forward to calculate formal error bars on the velocity/depth models presented above. Primarily such limits depend on the extent in time/distance space of the picked arrivals, including the scatter of arrival times. However before attempting to correlate between the models, and with the seismic reflection profile, it is appropriate to investigate the likely accuracy of the models by perturbing one parameter at a time.

The simple models derived from near-vertical-incidence reflections are easy to investigate. The result of changing the depth of a reflector by ±50m and the interval velocity in the overlying 300 m thick layer by ±0.05 km s^{-1} is shown in Figure 39. It is clear from the example that the depth of a reflector can be gauged with a precision of about ±25 m whereas the interval velocity of a layer a few hundred metres thick is not known to better than ±0.05 km s^{-1} (although more precise velocities will be obtained for thicker layers).

The travel-time models for the wide-angle refraction profiles are more complex because they involve velocity gradients and, within the assumptions used, are non-unique. The times of the primary 2.5 km s^{-1} sediment arrivals can resolve changes in the depth of the mid-sediment reflector to within about ±25 m whereas the multiple sediment arrivals will resolve changes in the velocity just below the reflector to about ±0.05 km s^{-1}.

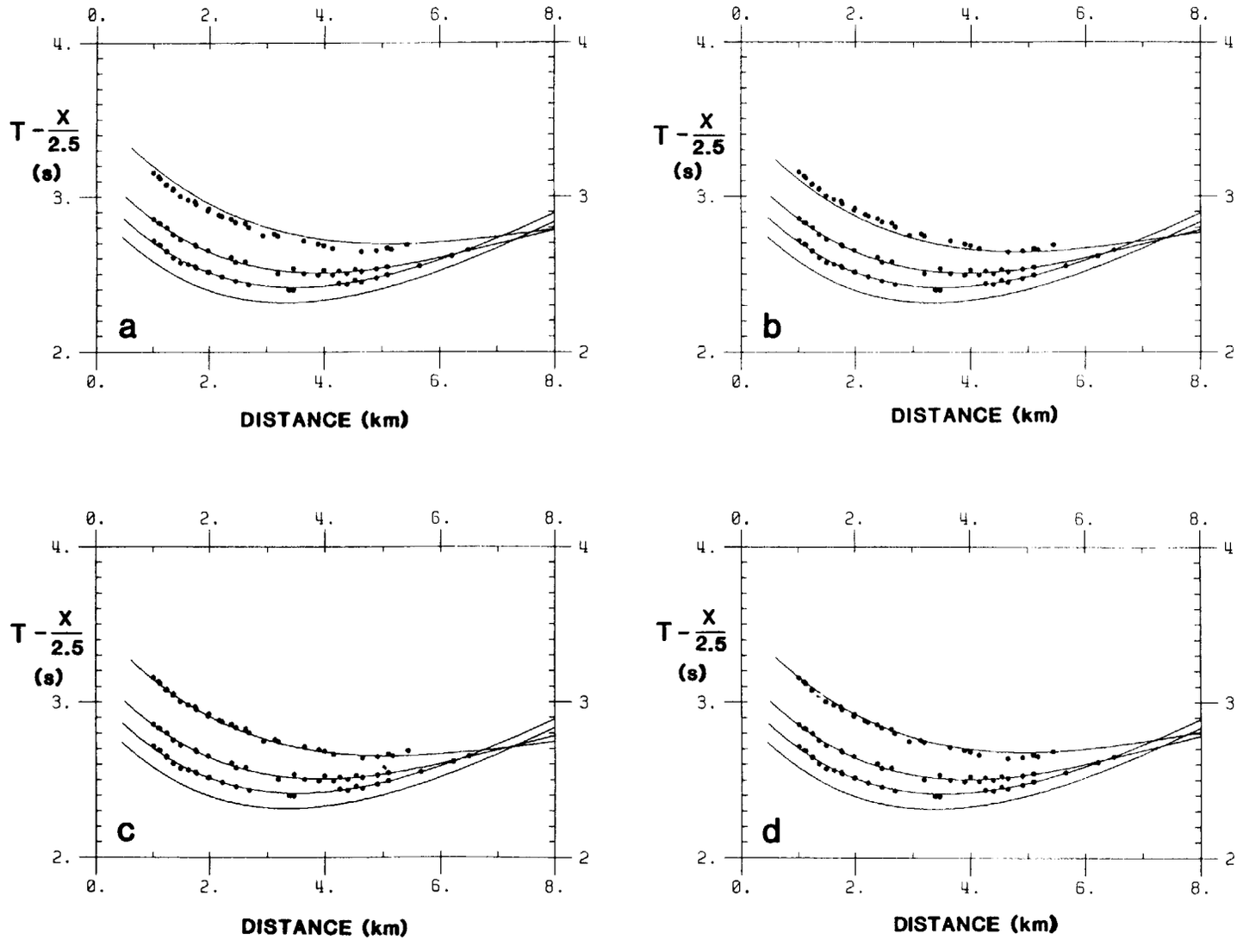

Figure 39: Calculated hodochrons based on perturbing the model, from near-vertical incidence reflections at Point NN, in the vicinity of the mid-sediment reflector (MSR) (a) MSR 50 m deeper, (b) MSR 50 m shallower, (c) velocity just below MSR 0.05 km s^{-1} greater, (d) velocity just below MSR 0.05 km s^{-1} smaller.

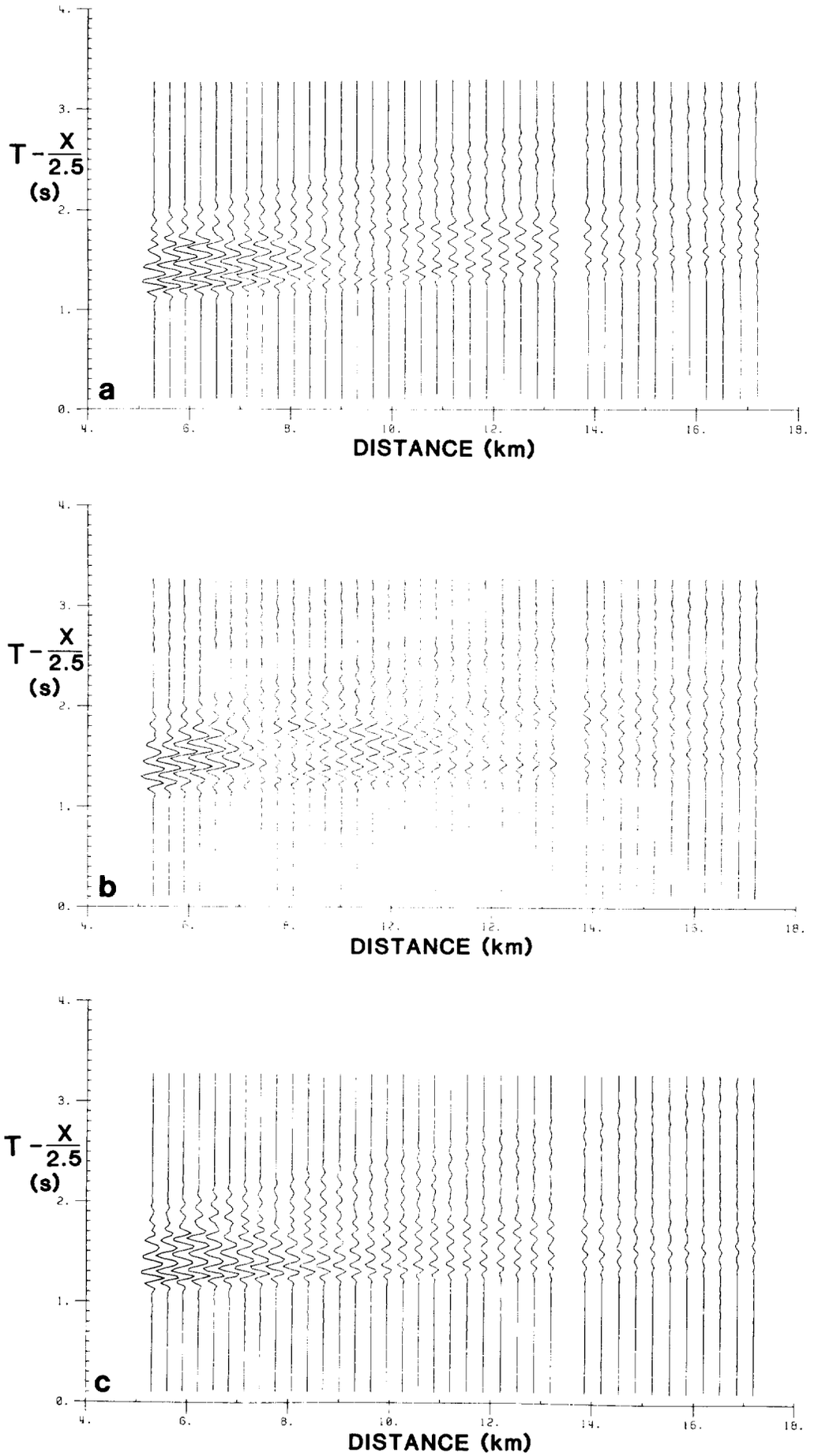

Figure 40: Synthetic seismogram record sections based on perturbations of the best model at Point L. (a) unperturbed model, (b) velocity gradient just below MSR increased to 0.488 s^{-1}, (c) shear-wave velocity above mid-sediment reflector (MSR) is 0.5 km s^{-1}.

The synthetic seismograms depend on several independently variable parameters, i.e. P- and S-wave velocity, Q factors and, particularly, velocity gradients. In Figure 40 examples are given of the synthetics due to (a) a change of gradient below the mid-sediment reflector due to a velocity change of -0.05 km s^{-1} just below the reflector (the gradient was changed from 0.288 to 0.488 s^{-1}) and (b) a change of S-wave velocity just above the reflector from 0.1 to 0.5 km s^{-1}. The sensitivity of the synthetic seismograms to fairly subtle changes in the model, and to the velocity gradient in particular, is very clear from Figure 40. This give us considerable confidence in the optimal nature of our models given the assumptions involved in their application.

9.4 **A velocity model from Point L to Point NN**

The objective of this work was to provide a velocity model for the sedimentary layer at and between Points L, MM and NN. The measurements described above do not provide a continuous estimate of velocity structure along the profile but average the structure over individual relatively short segments of the refraction profiles. The problem to address is how these structures should be merged laterally in such a way that a meaningful correlation is made with the geology seen on the seismic reflection profile. The following discussion is based on the premise that at least some of the reflectors on the seismic reflection profile, in particular those across which there is a strong angular unconformity, relate to significant changes in the overall velocity/depth structure. The physical character of horizons which are efficient reflectors at 60 Hz and that of horizons which are important in determining the energy distribution in wide-angle seismograms at 10 Hz are not necessarily the same and may be very different. However it is likely that the velocity changes due to age and lithological differences across significant structural unconformities in the sediments will be detected by both seismic reflection and refraction techniques.

The first step is to transform the velocity/depth structures to velocity/vertical travel-time by integration, assuming layers with zero or linear velocity gradients. The 'depth' (times) of important features can then be plotted on the reflection profile with a lateral extent corresponding to the estimated region along the profile which was "sampled" by the primary sediment arrivals (Figure 41a).

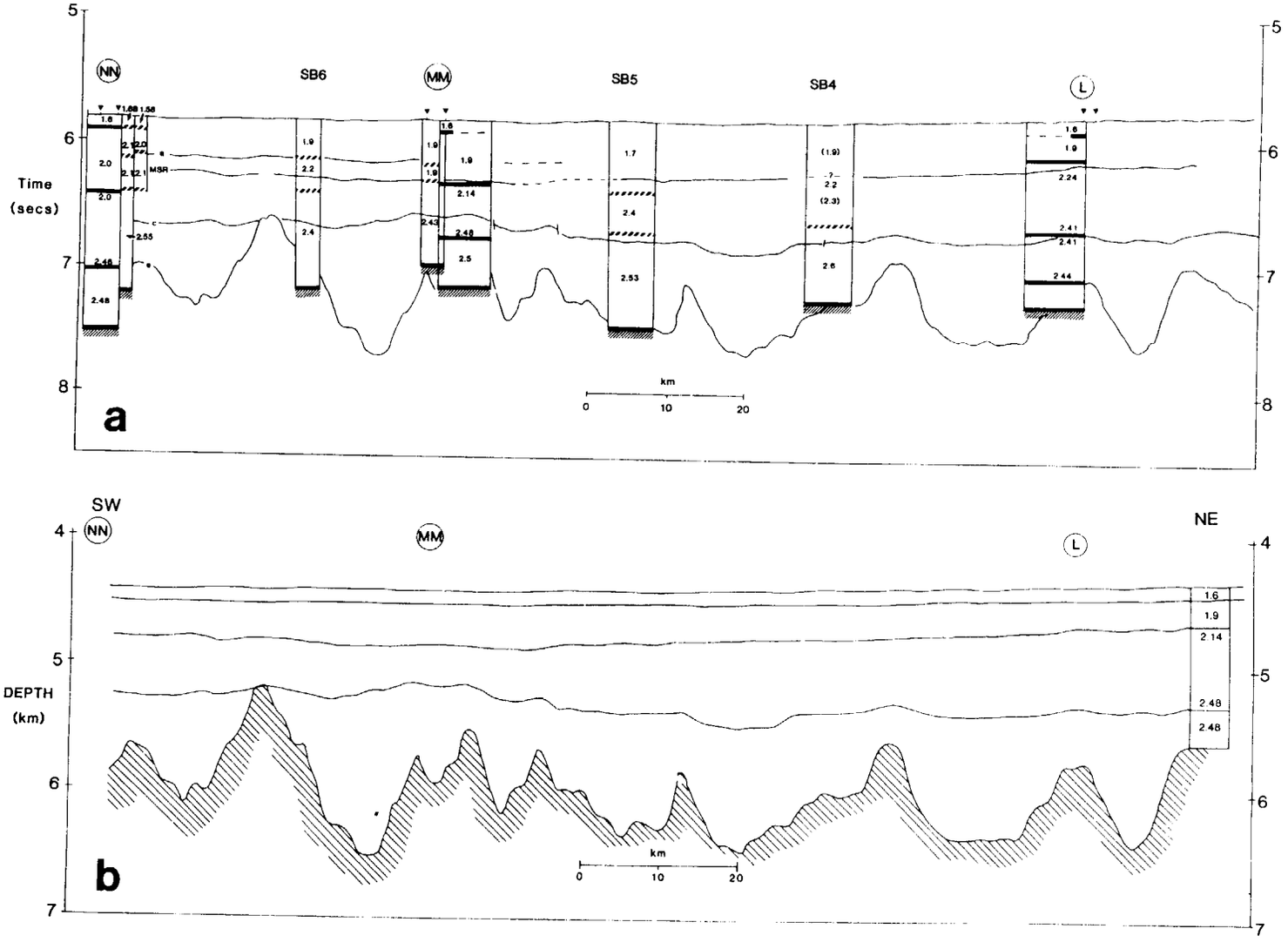

Figure 41: a. Summary of velocity models transformed to a vertical travel-time axis for comparison with the seismic reflection profile. The 'depth' of a feature in the reflection profile, which appears to correlate with the mid-sediment reflector (MSR), is indicated as is the top of the transparent 'pelagic sediment' layer (Reflector c). This layer may correspond to the nearly constant velocity lowermost sediments. b. Summary depth section between Point L and Point NN derived from correlations proposed in Figure 41a. See text for full explanation.

In Figure 41a the mid-sediment reflector lies between Reflectors a and b and closely corresponds with the top of a sequence of closely-spaced layered reflections seen between 1700 and 2130 hours (Figure 5). The importance of this correlation is that in the vicinity of Point NN the mid-sediment reflector onlaps Reflector b. Although there is no reflection profile SW of Point NN it is reasonable to suppose that the mid-sediment reflector is absent there. This may explain the lack of a step in P-wave velocity in the Point NN velocity structure. If it is correct that the mid-sediment reflector is primarily due to the S-wave velocity contrast across it then the rather weak P-wave signal from this reflector at vertical incidence (where the reflection coefficient theoretically is zero) is not unexpected.

A second important feature in Figure 41a is the top of the low-velocity gradient layer in the lower sediments. Generally this corresponds to velocities in excess of 2.40 km s^{-1} both on the near-vertical-incidence reflection and synthetic seismogram models. This horizon lies very close to Reflector c, the top of the relatively transparent layer of draped pelagic sediments.

Following the above correlations in time of features in the velocity models with two horizons on the seismic reflection profile it is now possible to transform Figure 41a to a depth section to obtain our best estimate of a continuous P-wave velocity structure between Points L and NN. This was calculated assuming 100 m of 1.6 km s^{-1} underlain by 1.9 km s^{-1} sediment in the upper sediment, a gradient from 2.14 to 2.48 km s^{-1} between the mid-sediment reflector and the top of the transparent layer (over which velocity is assumed to vary linearly with time), and a constant velocity of 2.48 km s^{-1} within the transparent layer. The resulting depth section appears in Figure 41b.

10. SUMMARY

Pairs of digital ocean-bottom seismographs (DOBS) were deployed at a depth of about 4400 m at three colinear points along a NE-SW profile eastsoutheast of Madeira. The DOBSs recorded shots from airgun sources to ranges in excess of 25 km. In addition three disposable sonobuoy profiles were also obtained.

Preliminary simple velocity models were obtained from the travel-times of near-vertical-incidence reflections. More sophisticated synthetic seismogram modelling was applied to three wide-angle seismic refraction profiles. This modelling identified an important and unsuspected mid-sediment reflector which had caused multiple reflection of energy refracted within the lower sediments. The upper sediments had velocities of 1.6 to 2.0 km s^{-1} and the lower sediment velocities lay between 2.14 and 2.51 km s^{-1}. The mid-sediment reflector appears to be associated with a small or negligible P-wave velocity contrast and a more substantial S-wave velocity difference. For this reason it is not clearly seen on seismic reflection profiles in the area.

The seismic structure of the upper sediments could not be constrained by synthetic seismogram modelling because no arrivals from the upper sediments could be distinguished on the record-sections. This is essentially a geometrical problem only soluble in oceanic depths by using bottom sources. The calculated velocity/depth models were transformed to velocity/vertical travel-time and compared with a seismic reflection profile from Point K to Point NN. The mid-sediment reflector was associated with a laterally extensive change in character in the upper part of the profile and the near-constant velocity layer with the transparent, probably pelagic, sediments draped over the volcanic basement. These correlations finally enabled an estimated depth section to be made from the whole reflection profile.

REFERENCES

ANON. 1983 Geophysical investigations of the Moroccan Continental Margin. Lamont Newsletter, 4, 2-3.

CHAPMAN, C.H. 1978 A new method for computing synthetic seismograms Geophysical Journal of the Royal Astronomical Society, 54, 481-518.

CHAPMAN, C.H. & ORCUTT, J.A. 1985 Least squares fitting of marine seismic refraction data. Geophysical Journal of the Royal Astronomical Society, 82, 339-374.

EMERY, K.O. & UCHUPI, E. 1984 The geology of the Atlantic Ocean. New York: Springer-Verlag, 1050 pp. + 22 charts.

FUCHS, K. & MULLER, G. 1971 Computation of synthetic seismograms with the reflectivity method and comparison with observations. Geophysical Journal of the Royal Astronomical Society, 23, 417-433.

FUGLISTER, F.C. 1960 Atlantic Ocean Atlas of Temperature & Salinity Profiles and Data from International Geophysical Year 1957-58. Woods Hole Oceanographic Institution, Woods Hole Atlas Series, Vol.1, 209pp.

HAMILTON, E.L. 1976 Shear-wave velocity versus depth in marine sediments: a review. Geophysics, 41, 985-996.

HAYES, D.E., PIMM, A.C. & SHIPBOARD SCIENTIFIC PARTY, 1972 Initial Reports of Deep-Sea Drilling Project, Volume 14. Washington, D.C.: U.S. Government Printing Office, 975 pp + charts.

HINZ, K., WINTERER, E.L. & SHIPBOARD SCIENTIFIC PARTY 1984 Initial Reports of the Deep-Sea Drilling Project, Volume 79. Washington, D.C.: U.S. Government Printing Office, 934 pp + charts.

KENT, D.V. & GRADSTEIN, F.M. 1986 Chapter 3. A Jurassic to recent chronology. pp.45-50 in, Geology in North America. Volume M. The western North Atlantic region, (ed. P.R. Vogt, B.E. Tucholke) Boulder, CO: Geological Society of America, 696pp.

KLITGORD, K.D. & SCHOUTEN, H. 1986 Plate kinematics of the central Atlantic. pp. 351-378 in, Geology of North America. Volume M. The western North Atlantic region, (ed. P.R. Vogt & B.E. Tucholke) Boulder, CO: Geological Society of America, 696pp.

LANCELOT, Y., WINTERER, E.L. & SHIPBOARD SCIENTIFIC PARTY 1980 Initial Reports of the Deep-Sea Drilling Project, Vol. 50. Washington D.C: U.S. Government Printing Office, 868pp + charts.

MOUNTAIN, G.S. & HAYES, D.E. 1985 Styles of deformation in the eastern North Atlantic (Abstract), EOS: Transactions American Geophysical Union, 66, 374.

PEAL, K.R. & KIRK, R.E. 1983 An event recording ocean bottom seismograph. pp. 114-118 in, Proceedings of 3rd Working Symposium on oceanographic data systems, Woods Hole, Massachusetts. October 1983. Silver Spring, MD.: IEEE Computer Society Press/WHOI, 199pp.

WHITMARSH, R.B. & LILWALL, R.C. 1983 Ocean-bottom seismographs. p.254-286 in, Structure and development of the Greenland-Scotland Ridge, new methods and concepts, (ed. M.H.P. Bott, S. Saxov, M. Talwani, J. Thiede.) New York: Plenum Press, 685 pp + chart.

WHITMARSH, R.B. & LILWALL, R.C. 1982 A new method for the determination of in situ shear-wave velocity in deep-sea sediments. Paper 4.2 in, Oceanology International 1982 Vol. 1. Kingston-upon-Thames: Spearhead Exhibitions Ltd. [21pp].

WHITMARSH, R.B. et al. 1986 RRS Discovery Cruise 161, 16 August (227) - 19 September (262) 1986. Portuguese ocean-continent boundary, plate boundaries west of Iberia and seismic structure of sediments off Madeira. Institute of Oceanographic Sciences, Cruise Report, No.188, 35pp.

WHITMARSH, R.B., AVEDIK, F., & SAUNDERS, M.R. 1986 The seismic structure of thinned continental crust in the northern Bay of Biscay. Geophysical Journal of the Royal Astronomical Society, 86, 589-602.

WINTERER, E.L., LANCELOT, Y. & HINZ, K. 1980 Chapter 6. Underway geophysical measurements from Glomar Challenger, Deep-Sea Drilling Project Leg 50 and multichannel seismic reflection profile of RN Meteor, Cruise 3902. Initial Reports of the Deep-Sea Drilling Project, Vol.50, 319-329.

TABLE 1. TYPES OF DATA USED FOR SEISMIC MODELLING

SOURCE	RECEIVER	MODELLING PROCEDURE
300 ins^3 airgun + WSK (13 sec. rate)	Sonobouy	Travel-time fitting of near-vertical incidence reflections
300 ins^3 airgun + WSK 4 x 1000 ins^3 airguns (120 sec. rate)	DOBS	Travel-time fitting of near-vertical incidence reflections.
4 x 1000 ins^3 airguns (120 sec. rate)	DOBS	Travel-time and amplitude modelling of wide-angle data.

TABLE 2 SOUNDSPEED MODEL IN THE VICINITY OF POINT L

Depth (m)	Soundspeed ($m\ s^{-1}$)
0	1530.0
100	1516.7
380	1506.4
600	1503.4
1180	1506.0
1830	1502.1
2320	1504.0
3260	1516.0
5000	1545.7

TABLE 3 SYNTHETIC SEISMOGRAM MODEL AT POINT L

Thickness (km)	P-wave velocity (km s^{-1})	S-wave velocity (km s^{-1})	Density (gm cm^{-3})	Q_α	Q_β
0.173	1.530	0.001	1.000	9999	9999
0.100	1.600	0.100	0.826	500	250
0.200	1.900	0.100	0.934	500	250
0.047	2.237	1.292	1.055	500	250
0.047	2.250	1.299	1.059	500	250
0.047	2.264	1.307	1.064	500	250
0.047	2.278	1.315	1.069	500	250
0.047	2.291	1.323	1.074	500	250
0.047	2.305	1.331	1.079	500	250
0.047	2.318	1.339	1.084	500	250
0.047	2.332	1.346	1.089	500	250
0.047	2.345	1.354	1.094	500	250
0.047	2.359	1.362	1.098	500	250
0.047	2.373	1.370	1.103	500	250
0.047	2.386	1.378	1.108	500	250
0.047	2.400	1.386	1.113	500	250
0.047	2.413	1.393	1.118	500	250
0.046	2.421	1.398	1.121	500	250
0.046	2.422	1.399	1.121	500	250
0.046	2.424	1.399	1.122	500	250
0.046	2.425	1.400	1.122	500	250
0.046	2.426	1.401	1.123	500	250
0.046	2.428	1.402	1.123	500	250
0.046	2.429	1.403	1.124	500	250
0.046	2.431	1.403	1.124	500	250
0.046	2.432	1.404	1.125	500	250
0.046	2.433	1.405	1.125	500	250
0.085	2.400	1.386	1.113	500	250
0.085	2.340	1.351	1.092	500	250
0.085	2.280	1.316	1.070	500	250
0.085	2.220	1.282	1.049	500	250
20.000	2.180	1.259	1.034	500	250

TABLE 4 SOUNDSPEED MODEL IN THE VICINITY OF POINT MM

Depth (m)	Soundspeed (m s^{-1})
0	1536.9
100	1515.2
440	1504.0
880	1503.3
1180	1505.9
1830	1502.1
2320	1504.0
3260	1516.0
5000	1545.7

TABLE 5 SYNTHETIC SEISMOGRAM MODEL AT POINT MM

Thickness (km)	P-wave velocity (km s^{-1})	S-wave velocity (km s^{-1})	Density (gm cm^{-3})	Q_α	Q_β
0.173	1.530	0.001	1.000	9999	9999
0.100	1.600	0.100	0.826	500	250
0.387	1.900	0.100	0.934	500	250
0.048	2.157	1.245	1.026	500	250
0.048	2.191	1.265	1.038	500	250
0.048	2.225	1.285	1.050	500	250
0.048	2.259	1.304	1.063	500	250
0.048	2.293	1.324	1.075	500	250
0.048	2.327	1.344	1.087	500	250
0.048	2.361	1.363	1.099	500	250
0.048	2.395	1.383	1.111	500	250
0.048	2.429	1.403	1.124	500	250
0.048	2.463	1.422	1.136	500	250
0.045	2.481	1.433	1.142	500	250
0.045	2.484	1.435	1.143	500	250
0.010	2.498	1.442	1.148	500	250
0.047	2.512	1.450	1.153	500	250
0.047	2.515	1.452	1.154	500	250
0.047	2.518	1.454	1.156	500	250
0.010	2.435	1.406	1.126	500	250
20.000	2.350	1.357	1.095	500	250

TABLE 6 SOUNDSPEED MODEL IN THE VICINITY OF POINT NN

Depth (m)	Soundspeed (m s^{-1})
0	1532.0
80	1516.0
420	1504.7
760	1504.0
1210	1505.6
1830	1502.1
2320	1504.0
3260	1516.0
5000	1545.7

TABLE 7 SYNTHETIC SEISMOGRAM MODEL AT POINT NN

Thickness (km)	P-wave velocity (km s^{-1})	S-wave velocity (km s^{-1})	Density (gm cm^{-3})	Q_α	Q_β
0.173	1.530	0.001	1.000	9999	9999
0.100	1.600	0.100	0.826	500	500
0.510	2.000	0.100	0.970	500	250
0.050	2.017	1.165	0.976	500	250
0.050	2.052	1.185	0.988	500	250
0.050	2.087	1.205	1.001	500	250
0.050	2.121	1.225	1.013	500	250
0.050	2.156	1.245	1.026	500	250
0.050	2.190	1.265	1.038	500	250
0.050	2.225	1.285	1.050	500	250
0.050	2.260	1.305	1.063	500	250
0.050	2.294	1.325	1.075	500	250
0.050	2.329	1.345	1.088	500	250
0.050	2.363	1.365	1.100	500	250
0.050	2.398	1.385	1.112	500	250
0.050	2.433	1.405	1.125	500	250
0.046	2.454	1.417	1.132	500	250
0.046	2.462	1.422	1.135	500	250
0.046	2.470	1.426	1.138	500	250
0.046	2.478	1.431	1.141	500	250
0.046	2.486	1.435	1.144	500	250
0.300	2.500	1.443	1.149	500	250
20.000	2.350	1.357	1.095	500	250

TABLE 8 VELOCITY STRUCTURES FROM SONOBUOY OBSERVATIONS

Sonobuoy 4

Depth (km)	Velocity (km s^{-1})
0	2.2
0.9	2.2
0.9	2.6
1.75	2.6
1.75	basement

Sonobuoy 5

Depth (km)	Velocity (km s^{-1})
0	1.7
0.48	1.7
0.48	2.4
0.87	2.4
0.87	2.53
1.84	2.53
1.84	basement

Sonobuoy 6

Depth (km)	Velocity (km s^{-1})
0	1.9
0.3	1.9
0.3	2.2
0.59	2.2
0.59	2.4
1.51	2.4
1.51	basement